



Title	PREEQUILIBRIUM DEEXCITATION PROCESS FOR (PARTICLE, $XN\ YP\ \gamma$) REACTIONS ON DEFORMED NUCLEI
Author(s)	Sakai, Hideyuki
Citation	大阪大学, 1978, 博士論文
Version Type	VoR
URL	https://hdl.handle.net/11094/24459
rights	
Note	

The University of Osaka Institutional Knowledge Archive : OUKA

<https://ir.library.osaka-u.ac.jp/>

The University of Osaka

PREEQUILIBRIUM DEEXCITATION PROCESS FOR
(PARTICLE, $XN\; YP\; \gamma$) REACTIONS ON DEFORMED NUCLEI

HIDEYUKI SAKAI

12

80SC00370

CONTENTS

	Page
Abstract	iii
§ 1 Introduction	
1-1 Compound Nucleus Formation and Deexcitation Process	1
1-2 Review of Preequilibrium Process	3
1-3 New Points of the Present Work	6
§ 2 Experimental Instruments and Procedures	
2-1 Instruments	
i) Accelerator and the F Beam Line	11
ii) Goniometers and Two Target Chambers	14
iii) Detectors	15
iv) Electronic Circuits	21
2-2 Procedures	23
§ 3 Results	
3-1 Cross Sections for the Preequilibrium and Equilibrium Reactions	
i) $\sigma(E_T)$ Cross Sections	26
ii) I_m ; Median Spin Values	31
iii) K-isomer Ratios	33
3-2 Neutrons Following $^{164}\text{Dy}(\alpha, xn)$ and $^{165}\text{Ho}(p, xn)$ Reactions	35
§ 4 Analyses	
4-1 An Exciton Model	40
4-2 An Application of the Exciton Model	44
4-3 Analysis by a Simple Model	47
4-4 Comparison with Experimental Results	52

4-5 Analysis of the K-isomer Ratios	59
§ 5 Discussions	61
§ 6 Summary and Concluding Remarks	70
§ 7 Acknowledgement	75
References	76
Figure Captions	84
Table 1	92
Figures	

Abstract

Preequilibrium and equilibrium processes of (particle, xn yp γ) reactions induced by medium energy projectiles were studied by investigating deexciting neutrons and gamma-rays. Neutrons following the $^{164}\text{Dy}(\alpha, xn\; yp\; \gamma)$ reaction at $E_\alpha = 90$ and 120 MeV and the $^{165}\text{Ho}(p, xn\; yp\; \gamma)$ reaction at $E_p = 60\text{ MeV}$ were measured in coincidence with discrete gamma-rays characteristic of the reaction channels (residual nuclei). Median spin values I_m for spin populations of yrast levels populated by the (particle, $xn\; \gamma$) reactions were obtained for various projectile energies and particles. Cross-sections for the (particle, $xn\; \gamma$) reactions and energy and angular distributions of the emitted neutrons were analyzed in terms of the preequilibrium and equilibrium deexcitation processes. Calculations based on an exciton model were carried out. Characteristic behaviours of the preequilibrium process were found in such (particle, $xn\; \gamma$) reactions that the $E_T = \sum_i E_i$ of the kinetic energies E_i of the emitted neutrons was large and the number of emitted neutrons was small. The cross-sections for the $(\alpha, xn\; \gamma)$ reaction at $E(\alpha) = 120\text{ MeV}$ were expressed by $\sigma = 0.7 \sum_x \sigma(3, x-3) + 0.3 \sum_x \sigma(2, x-2)$, where $\sigma(n_p, n_e)$ stands for emission of n_p neutrons at pre-equilibrium stage followed by evaporation of n_e neutrons at the equilibrium stage. Other reaction were also well reproduced in a similar manner. K-isomer ratios, being defined as the ratio of the population of the K-isomer with spin I ($I=K$) to that of the ground state rotational band (gsb) ($K=0$) levels

with the same spin I, in ^{182}Os and $^{172,174}\text{Hf}$ were studied by (particle, $xn\ \gamma$) reactions for various kinds of projectiles in a wide range of the projectile energies. The K-isomer ratios were found to depend on the projectile mass.

§1. Introduction

Nuclear reactions induced by medium energy projectiles with velocity near the Fermi motion in nuclei are interesting in view of preequilibrium and equilibrium deexcitation processes. A number of fast nucleons are expected to be emitted at the preequilibrium stage, and later on some slow nucleons (mostly neutrons in medium and heavy nuclei) are evaporated at the equilibrium stage.

The purpose of the present work is to investigate in detail the preequilibrium process of (particle, xn yp γ) reactions at moderate energy projectiles. We first review the mechanism of the (particle, xn yp γ) reaction at low energy projectiles. This is called as a statistical process or compound process. Secondly we review the preequilibrium process at higher projectile energies. Main ideas and methods of the present work are given in sub-section 1.3.

1.1 Compound Nucleus Formation and Deexcitation Process

Nuclear reactions of the type (particle, xn γ) with low energy projectiles (~ 10 MeV per nucleon) on medium mass nuclei are mostly of a statistical process¹⁻³. The reaction cross section is close to a geometrical value ($\sim \pi R^2$). Thus the nucleus may be considered to be almost a black body for

the incident particles. The excitation function for the reaction cross-section is well interpreted in terms of an evaporation model, namely the compound nucleus model proposed by N.Bohr (1936).⁴⁾ Inbeam gamma spectroscopy by using the (particle, xn) reaction was originated by Morinaga and Gugelot.⁵⁾ It has provided a wealth of spectroscopic informations. An angular momentum transferred to the residual nucleus has also been extensively studied by the inbeam gamma measurements. The angular momentum distribution at the ground state rotational band (gsb) is always anomalously more damped than expected on the statistical deexcitation of the compound nucleus.

A simple view of the deexcitation process for the (particle, $xn \gamma$) reaction (see fig. 1-1) is as follows.

The compound nucleus has a high excitation energy and a large angular momentum. It firstly deexcites by neutron emissions (evaporation) down to a region where gamma decays become comparative. The energy spectrum of the evaporated neutron is known to have a Maxwellian distribution peaking at around $kT = 1 \sim 2$ MeV where T is the nuclear temperature. The mean energy is determined from the level density of the residual nucleus. The angular distribution of the evaporated neutrons are symmetric with respect to 90° to the incident beam direction. These low energy neutrons are mostly of s or p wave, and take out little angular momentum. Then gamma decay begins statistically to enter rotational bands built on two

quasi-particle states lying close to the yrast line. We call this starting point of the statistical decay as the entry point. The spin is given as I_Y . The excited nucleus loses little angular momentum but a large energy through the statistical gamma decay, in which $2 \sim 3$ gamma rays of probably dipole character are involved. The next stage of deexcitation proceeds through intra-band transitions along rotational bands built on two quasi-particle states according to the K-band deexcitation process.⁶⁻⁵⁾ Each decay takes away two units of angular momentum. The angular momentum decreases mainly through this process. The rotational transition prefers intraband decay to interband decay by virtue of K (projection of the angular momentum on the nuclear symmetry axis) selection rule. The final decay process is the rotational transitions through the yrast band. The K-selection rule plays an important role in the decay process, and is known as a K-conservation model.⁶⁻⁸⁾ We call the median spin for the spin population of the yrast levels (gsb) as I_m .⁷⁾ Thus the I_m gives information on the spin distribution of gamma ray deexcitation process.

1.2. Review of Preequilibrium Process

The preequilibrium process has been investigated earlier by several authors.⁹⁻¹⁴⁾ Recently high energy tails of deexciting particle spectra have extensively been studied by

many investigators.¹⁵⁻²³⁾ They are mostly high energy protons following (α , p), and (^3He , p) reactions⁸⁻²⁰⁾, inelastic scatterings of charged particles^{21,22)}, and the (p, n) reactions.^{23,24)} Excitation functions for equilibrium and pre-equilibrium reactions have been studied on (particle, $xn\ yp\ \gamma$) reactions.²⁵⁾ The characteristic features obtained by those studies are as follows;

- i) The energy distribution of emitted particles deviates at high energy region from what one would expect on a basis of the compound (equilibrium) reaction process.
- ii) The angular distribution of emitted particles is not isotropic in the CM frame of the compound nucleus and exhibits a considerable enhancement in a high energy region.
- iii) The excitation function of the cross section is much different from that expected from pure statistical decay.
- iv) The integrated cross-section of the high energy component of the spectrum depends on $AT^{1/3}$ where AT is the target mass, rather than $AT^{2/3}$. Thus it is mostly due to a peripheral process.

We consider the reaction mechanism of a nucleon-nucleon collision in terms of a door way state. It is schematically illustrated in fig. 1-2. The reaction starts through a 1-particle state. For simplicity we assume a nucleon-nucleon

collision. (For an alpha particle projectile the starting state is a four particle state.) It goes to a 2p-1h states by a nucleon-nucleon collision, and then to 3p-2h states and so on. Finally the system gets equilibrium (compound nucleus) after many collisions. Some particles created through these nucleon-nucleon collisions are unbound. Thus they may escape before the system gets equilibrium. These nucleons contribute to a high energy component of the spectrum. If the projectile energy is high, the escape (emission) probability of these particles before the equilibrium is larger. This process is called as a preequilibrium process.

There are mainly two types of approach existing to describe the preequilibrium process. One is an intra nuclear cascade model, and another is an exciton model. The cascade model²⁶⁻²⁸⁾ considers successive two body collisions between the nucleons. The paths of the nucleons are followed on classical trajectories in the nucleus until the nucleons lose their energies. The model can predict energy and angular distributions of emitted nucleons. This model was firstly developed to analyse the quasi-free scattering phenomena for high energy reactions (> 100 MeV/nucleon). The predicted energy and angular distributions are not in good agreement with experimental data for low and medium energy nuclear reactions (< 100 MeV/nucleon). The model may be used only for nucleon induced reactions.

Another approach is the exciton model, which was originated by Griffin.²⁹⁾ The exciton model describes the nuclear states in terms of the exciton number $n = p+h$, where p and n are respectively number of particles and holes, and the total excitation energy E . For each exciton number, some fraction of states have unbound particles which may escape to a continuum state. It is shown in fig. 1-2. This model was combined with the master equation approach of Harp, Miller and Berne³⁰⁾ by Cline and Blann.³¹⁾ It has been generalized as a hybrid model by Blann.^{32,33)} The refinements of the model has also been done by Gadioli et.al.^{34,35)} Blann has developed his hybrid model by taking into accounts a geometry-dependent mean free path. This is called as a geometry-dependent hybrid model (GDH).³⁶⁾ Recently, the exciton model has been extended to calculate the angular distribution of emitted particles.^{37,38)} The exciton model based on the master equation approach is described in Chapter 4. The model reproduces well the preequilibrium cross-section, and energy and angular distributions of deexciting particles.²⁹⁻⁴⁰⁾ Recent reviews on these subjects are given by Blann,⁴¹⁾ and Gadioli and Gadioli Erba.⁴²⁾

1.3. New Points of the Present Work

The purpose of the present work is to investigate in detail the preequilibrium process of (particle, $xn\; yp\; \gamma$) reactions

by measuring neutrons and gamma rays in coincidence with discrete gamma rays characteristic of various reaction channels. The main ideas and new points of the present work are as follows. i) Reaction channels for medium energy projectiles interacting with medium heavy nuclei are mostly ($i, xn \gamma$) reactions. The deexcitation scheme for 120 MeV alpha bombardment, the energy sum E_T of the deexciting particles and the average energy \bar{E}_n per nucleon are shown in fig. 1-3. The \bar{E}_n is very large for small number (x) of emitted nucleons, and decreases rapidly with increase of the number of evaporated neutrons. The former may be characterised as mainly the preequilibrium process, and the latter as the equilibrium process. These reaction channels (numbers of emitted nucleons or final product nuclei) are identified by requiring coincidence with the characteristic gamma rays. ii) The major component of the deexciting particles are in the low energy region of $1 \sim 20$ MeV, where many reaction channels are mixed ($x = 4 \sim 11$). Interesting is to investigate the deexcitation process for the low-energy component of each reaction channel. iii) The cross-sections, the energy spectra of the deexciting particles, and their angular distributions for various reaction channels (number of emitted neutrons) give such an information as number of particles emitted at the preequilibrium phase and the exciton numbers of the preequilibrium stage. iv) The deexciting particles with a large \bar{E}_n/x take out more

angular momentum than those with a small \bar{E}_n/x . Thus angular momenta transferred to the residual nuclei depend on the particle decay at the preequilibrium and equilibrium phases and this causes a change in gamma ray deexcitation flow (see fig. 1-1). These effects can be obtained by the median spin values I_m . v) Systematic studies using various projectiles and energies will make the preequilibrium process more clearly.

We studied also K-isomer ratio following (particle, xn γ) reactions. Protons may transfer a large angular momentum to one nucleon in the target nucleus by the proton-nucleon collision, resulting in excitation of high K quasi-particle states. Complex projectiles, however, transfer large angular momentum to many nucleons in the compound system, and may give rise to a rotation of the whole nucleus. The rotation of the projectile-target composite system induced by the collision of the heavy projectile with the outer region of the target may be characterized as low K motion, populating the gsb ($K = 0$). Thus one expects the large K isomer ratio for the proton projectile and the large yrast band ($K = 0$) population for complex projectiles. (Here the K-isomer ratio is defined as a ratio of the population of the K-isomer with spin J to that of the gsb ($K = 0$) level with the same spin J).^{8,45)} If complex projectiles bring so large angular momentum that the Coriolis interaction destroys the K-selection rule,^{8,43)} gamma cascades feed strongly the gsb with $K = 0$. In fact heavy

ions do not feed much levels other than yrast levels.⁴⁴⁾ Measurements of the isomer ratios by using various kinds of projectiles in wide energy range are essential to clarify the projectile dependence. Use of different projectiles with similar incident (angular) momenta for populating the same isomer is particularly important to study the projectile dependence.

We chose for the present work such (particle, $xn\ \gamma$) reactions that give residual nuclei of Er and Hf isotopes, because the rotational levels and other low lying levels in these residual isotopes are well known. The discrete gamma rays from the rotational levels, which are characteristic of the residual nuclei (reaction channels), are used to give the cross-sections of the various reaction channels in the single mode, and to identify the reaction channels in the coincidence mode. The K-isomers of $^{182}\text{Os}\ J^{\pi}K = 8^-8$ and $^{172}\text{Hf}\ J^{\pi}K = 6^+6$ were studied to investigate the projectile dependence of the K-isomer ratio because they are well excited by various type of (i, $xn\ \gamma$) reactions and they are close in the excitation energy and far separated in the K-quantum number.

Experimental instruments and procedures are given in the next Chapter. Results are presented in Chapter 3. The analyses in terms of the preequilibrium and equilibrium process based on an exciton model calculations are given in Chapter 4.

Detailed discussions on the reaction mechanism are presented in Chapter 5, and summary in Chapter 6. A part of this work has been published in refs. 46, 47 and 48.

§2 Experimental Instruments and Procedures

2-1 Instruments

i) Accelerator and the F Beam Line

The RCNP cyclotron^{49,50)} is a 230 cm variable energy AVF cyclotron with $K = 120$ MeV. The K is defined as $E = KQ^2/A$. It gives stable and high quality beams of p , d , ^3He , α , polarized p and d , and various kinds of heavy ions. The beam intensity and the beam spot of the beam have to be very stable for our inbeam gamma measurement with Ge(Li) detectors in order to keep constant counting rate and good energy resolution.

The F beam line was constructed for the inbeam photon, electron and particle (PEP) spectroscopy. A rough sketch of the F beam line is shown in fig.2-1. The accelerated particles from the cyclotron are analyzed in energy by the analyzing magnet and deflected by the switching magnet, and focussed on to the defining slit (F6). The F beam line has two sets of target ports. They are located in cascade, and each has a target chamber and a goniometer. The beam is focussed on a first target by means of two sets of quadrupole magnetic lenses (Q3, Q4). Light ion (p , d , He) beams passing through the first target spread little, but the spread of heavy ions is considerable. Then the beam is refocussed by use of another set of quadrupole magnetic lenses (Damp Q) onto the second target, and stopped by the beam dumper which is located 1.8m behind the second target. The beam dumper is made of Ta.

It is shielded with paraffin, iron and lead bricks as shown in fig.2-1. A size of a light ion beam spot is typically less than 2mm \varnothing at both the first and the second target ports. A spot size of a heavy ion (for example 130 MeV ^{14}N) on the second target gets larger by a factor two than that on the first target when the first target of a few mg/cm 2 is used. Thus in most cases we take out the first target to perform accurate measurement with heavy ion beams at the second beam port. No beam defining slits are set inside the beam duct in the target room in order to avoid background gamma rays from defining slits. Seven graphaite baffles with apertures of 15 ~ 30 mm in diameters are set inside the beam tubes to reject stray (scattered) beam.

The beam duct is evacuated by means of three turbo-molecular pumps with 250l/sec evacuation speed. Two liquid nitrogen traps are set for each target chambers, one before and another behind the target chamber. Pressure in the target chamber is typically 2×10^{-5} Torr without the liquid nitrogen traps and 1×10^{-6} Torr with liquid nitrogen traps.

The background gamma rays with blank target above 80keV from stray beam and the beam damper with a 55cc Ge(Li) detector are only ~25 counts/sec with 90 MeV 4nA alpha beam in the beam line. The neutron background, measured in the 5" \varnothing x 5" NE213 liquid scintillator at 22.5cm from the first target, is less than 10 counts/sec. These back ground counts

for both gamma and neutron counts are typically less than one percent of the true counts due to gamma rays and neutrons from a target.

Prompt and delayed gamma ray spectra are measured by using naturally bunched beam from the cyclotron. Here the "prompt spectrum" is for prompt gamma rays coming within $20 \sim 30$ ns after every beam burst, and the "delayed spectrum" is for delayed gamma rays observed with a certain (typically $20 \sim 30$ ns) delay after every beam burst. The time spectrum was obtained by starting a time to amplitude converter (TAC) with gamma ray signal and stopping it by a time signal of the bunched beam. The time signal of the beam was picked up from the RF oscillator (Dee) of the cyclotron. The circuit diagram to pick up the RF signal is shown in fig. 2-2. The scale down mode by a factor 1/2 in fig. 2-2 gives two prompt peaks in the time spectrum, from which we calculated the time scale. By using 70 MeV alpha particles the FWHM of the prompt peak is about 13 ns for $E_\gamma \geq 150$ KeV and 5 ns for $E_\gamma \geq 1$ MeV. The shield against the RF noise is not necessary. The time signal of the pulsed beam is obtained also by a thin plastic scintillator foil set behind the second target port (see fig. 2-1). This method has merit of being free from time fluctuation due to the phase traveling. The width of the prompt peak using this system and Ge(Li) detector for $E_\gamma \geq 150$ keV was about 4.5 ns including the time

resolution of detection system and beam width.

ii) Goniometers and Two Target Chambers

Two goniometers were installed on the F beam line. Each goniometer has four turn tables. Two of them in the first (upstream) goniometer can be rotated by stepping motors. Other two turn tables are rotated manually. All of the turn tables in the second (downstream) goniometer can be rotated remotely. These turn tables are used for Ge(Li) detectors, Ge(HP) [so called LEPS] detectors, liquid-scintillators and NaI (Tl) detectors. Angles of the turn tables are read by three ways, counting the number of pulses used to move stepping motors, the potentiometer reading, and reading directly angular scales by means of industrial TV cameras.

The target chamber, being installed on the first goniometer, is made of stainless steel, and has two wide windows at left and right hand sides of the beam line. The windows are vacuum-sealed with thin Al(0.5mm) plate or mylar (0.05mm) film and a 5mm thick lucite plate. Absorption due to the thin window may be neglected for gamma rays above 100 keV. This chamber is usually used for γ - γ , n- γ or n-n coincidence measurements. The goniometer and a typical example of the counter arrangements is schematically illustrated in fig.2-3.

The target chamber installed on the second goniometer is also made of stainless steel and designed for the charged particle gamma-ray correlation measurements. Therefore

it has a wide window for gamma ray detection. It is vacuum sealed with a thin ($20\mu\text{m}$) mylar film. Two turn tables are set inside the chamber. One of them can be rotated by means of a stepping motor.

The target ladders of each chamber can be moved up and down and be rotated by means of two 23PM-C004 stepping motors.

iii) Detectors

(A) Ge(Li) detectors

The following coaxial detectors were used; 55cc ORTEC-I, 55cc ORTEC-II, 35cc HORIBA-I, 35cc HORIBA-II, and some other home made detectors. The energy resolutions of these detectors were typically $\text{FWHM} = 2.0 \sim 2.3 \text{ keV}$ for the ^{60}Co 1332 keV gamma rays.

The counting rate has to be nearly constant to keep the counting condition stable. The counting rate was monitored by a counting rate meter for one of the gamma detectors, so that the PHAs, scalers, raw data processor (PDP-11) and beam current integrator run when the counting rate is within the given range (typically $1.5 \sim 3 \text{ k counts/sec}$).

The beam current integrator was modified slightly for this purpose. The dead time was typically less than 10%. The Ge(Li) detectors were shielded by lead block of 5cm thickness to reduce background gamma rays.

A 1mm thickness copper plate was inserted between the lead shield and aluminum cap of Ge(Li) detector to absorb lead x-rays from the lead shield. In front of the Ge(Li) detector a 2~3mm thick copper or brass absorber was set to reduce the low energy x-rays and gamma rays coming from the target. These Ge(Li) detectors were used for measuring discrete gamma rays, monitoring reactions, gamma ray multiplicity measurements, and identification of reaction channels.

(B) High Purity Germanium Detector "LEPS"

Nuclear reactions induced by moderately high energy projectiles have many reaction channels. Thus gamma rays following these many reaction channels are plenty and the gamma ray spectrum is much complicated. These complicated spectrum was precisely measured by a 1.4cc high purity Ge detector "LEPS" with its high resolution. The energy resolution is FWHM=565 eV for ^{57}Co 122 keV gamma rays and 1 keV for 511 keV gamma rays. The counting rate was always kept below 700 counts/sec by adjusting the distance from the target to LEPS. Therefore no dead time correction was necessary. No lead shield was employed but a 0.5~1.5mm thickness brass absorber was set in front of the LEPS. The photo peak energy was determined within 0.2 keV. It was made clear that the LEPS was very powerful for resolving gamma rays and gave cross sections of various kinds of

weak or strong reaction channels.

The absolute efficiencies of these Ge(Li) and LEPS detectors were measured every time after the experiment by an RI source set (RCC QCR 1) and ^{226}Ra (RCC RAC 2) at the target position.

The typical examples of absolute efficiency curves obtained for ORTEC-II Ge(Li) and LEPS are shown in figs. 2-4-a,b.

(C) Liquid Scintillator NE213

Neutron energy was measured by an NE213 organic scintillator. It has a good detection efficiency and gamma rays were discriminated by pulse shape analysis. In what follows the details of this method are described.

The organic scintillator detects neutron through recoiling protons. The recoil proton makes a continuous energy distribution depending on the angular distribution of the recoil proton with respect to the incident neutron. The organic scintillator detects gamma rays also through the Compton electron scattering. The decay time ^{51,52)} of the fluorescent light output in some scintillators(NE213, Stilbene, KL356 etc.) have mainly two components, one is a fast ($2 \sim 4$ ns) one and another is a slow ($10 \sim 30$ ns) one. The former is due to low ionization density, and the latter due to high ionization density. The recoil proton produces higher ionization densities than the compton electron does. This effect is used to distinguish neutrons from gamma rays. The organic scintillator NE213 is quite good for this discrimination. We used these two NE213 liquid scintillators, one $5" \phi \times 5"$ and another $3" \phi \times 1"$. Hereafter we describe properties of the NE213 liquid scintillator.

The light output is proportional to the energy for electrons, while it is proportional to about the 3/2 power of the energy for protons. Fig. 2-5 is the light output against energy for the NE213 measured by V.V.Verbinski⁵³. The light output of a scintillator is usually calibrated by measuring the Compton edge of gamma rays. Following gamma rays were used for the light output calibration; ⁵⁶Co ($E_e = 3017, 2365, 1027$ keV), ⁸⁸Y ($E_e = 1612$ keV), and ²²Na ($E_e = 1062, 341$ keV). Since no gamma ray source with the Compton edge greater than 3 MeV was available, light outputs for higher energy electrons were extrapolated. The error there was about $\pm 5\%$.

We, for simplicity, neglect multiple scattering in the scintillator, escape of protons from the scintillator, and finite energy resolution for the scintillator. We assume that the energy distribution $f(E_p)$ of the recoil proton is simply given as $f(E_p) = \text{constant}$ for $E_p < E_m$, $f(E_p) = 0$ for $E_p > E_m$, where E_m is the maximum energy (i.e. neutron energy). This is based on an isotropic angular distribution of the recoil proton as found experimentally in the present energy region. Then the number of recoil protons is given by

$$N_p = \frac{n_H \sigma_H}{n_H \sigma_H + n_C \sigma_C} N_0 \{ 1 - \exp [- (n_H \sigma_H + n_C \sigma_C) d] \} , \quad (2.1)$$

where N_0 : the number of incident neutrons

n_H, n_C : the number of hydrogen atom per cm^3 and that of carbon,

σ_H : the neutron-hydrogen cross sections

σ_C : the neutron-carbon cross sections

d : the thickness of the scintillator.

Actually pulses from recoil carbon are too small to be distinguished from the photomultiplier noise, and to be identified by the pulse shape discrimination circuit. We set a lower discrimination level B to cut away these small pulses and noises (see fig. 2-6). The detection efficiency with the discrimination level B is,

$$\begin{aligned}\epsilon(E_n, B) &= \left(1 - \frac{B}{E_n}\right) \frac{n_H \sigma_H}{n_H \sigma_H + n_C \sigma_C} \{1 - \exp[-(n_H \sigma_H + n_C \sigma_C) d]\} \\ &= \left(1 - \frac{B}{E_n}\right) \epsilon_0(E_n)\end{aligned}\quad (2-2)$$

For a large volume liquid scintillator, say $5''\phi \times 5''$, the assumptions mentioned above are crude. Thus a Monte Carlo calculation was made to get a realistic detection efficiency ^{54,55)}. Energies produced by a neutron through scattering and reaction in the liquid scintillator are calculated ^{*)}. The calculated detection efficiency with a certain lower threshold is compared with the experimentally measured value ⁵⁵⁾ in fig.

2-7. Agreement is satisfactory. Pulse height distributions for neutrons in a wide energy range are necessary for unfolding the light output spectrum.

*) Monte Carlo calculation code was provided by K. Shin, Dept. of Nucl. Eng. Kyoto Univ. and modified by the author.

A finite energy resolution of the scintillator has to be included in the calculation. Here Gaussian smearing function was introduced, its energy dependence is expressed by

$$\text{FWHM} = 0.11 + 0.05L_p ,$$

where L_p is the light output in electron energy unit(MeV) .

In fig. 2-8 two examples compared with measured pulse height distribution are shown.

There are two methods of unfolding the light output spectrum from scintillator, one is the differentiation method and another is the response matrix method⁵⁶⁾. The differentiation method is easy to compute but it introduces error for a large volume liquid scintillator in which pulse height distribution is no more constant. The response matrix method needs more elaborate computations which demand many data points and good statistics. Comparison of these method will be given in §3.2.

iv) Electronics Circuits

The block diagram of the circuits system is shown in fig.2- 9. It is composed of four parts. The first part is for measurement of a single gamma-ray spectrum by the LEPS to obtain cross sections. The second part is for prompt and delayed gamma ray measurements. Constant fraction timing circuits were employed to get fast logic signals.

Some pulses of low energy gamma rays with slow rise-time were rejected by the slow rise time rejection mode. Since the pulse height discrimination of the CFD is not sharp, the energy signals are gated by the logic signals from the CFD. The energy (linear) pulse was analyzed in a 4096 channel PHA (Canberra 8700). The spectrum was routed by the time signals so as to get the prompt and delayed spectra ($2K \times 2$). The third part is for neutron-gamma coincidence measurements. Neutron signals were obtained by the pulse-shape discriminator circuit⁵⁷⁾. Conventional fast slow circuits were employed. The gate width for the fast coincidence system was $\Delta t \sim 50\text{ns}$, and that for the slow coincidence system is $\Delta t \sim 4\mu\text{s}$. The rate of accidental coincidence was at most 2%. The gamma ray energy and the neutron pulse height spectra were taken by a 4096 channel two-parameter pulse-height analyzer (Canberra 8100) with 512 channel for the gamma ray energy, 8 channels for the neutron pulse height. The 8 channels for the neutron pulse height gave only a crude shape of the spectrum. Thus we used later the event by event mode (list mode) for $n-\gamma$ coincidence data. The fourth part is for a raw data processor. All informations (E_n , E_γ , TAC($n-\gamma$), TAC(PSA)) were collected by event by event mode. So there is no limitation to memory size. After the experiment off line analyses were performed. Data tapes were sorted by the central computer (TOSBAC 5600/120).

2.2 Procedures

Most of projectiles used for the experiment were provided by the RCNP AVF cyclotron at Osaka University. Use was also made of ^3He beams provided by the Dept. Physics Osaka Univ. cyclotron and the IPCR cyclotron for K-isomer studies. The projectiles and the targets used in the present work are listed in table 1. The $^{162,164}\text{Dy}$, $^{174,176}\text{Yb}$ and ^{184}W targets with $1 \sim 5\text{mg/cm}^2$ in thickness were prepared by depositing oxide powders onto thin mylar (0.003mm) film. Self supporting metallic foils of the natural Ho(99.9% of ^{165}Ho) and natural Lu(97.4% of ^{175}Lu) with $2 \sim 11\text{mg/cm}^2$ in thickness were prepared by rolling small pieces of metals. The ^{185}Re target was prepared by depositing metallic powder onto thin mylar film. The cross-sections of various reaction channels were mostly obtained by a 1.4cc pure Ge detector "LEPS" and a 55cc Ge(Li) detector was also used in some cases. The detector was set mostly at about 125° , where $P_2(\cos\theta) = 0$, with respect to the incident beam direction. Gamma ray spectra were obtained at 40° , 110° or 149° in some case where the cross sections were corrected for the anisotropic angular distribution. The cross sections of the various (i, xn yp za γ) reactions were obtained from the gamma works. 58-59)

The angular and energy distributions of the neutrons were measured for following reactions



at 35° - 145° with respect to the incident beam direction in coincidence with rotational gamma rays which were detected at 90° . Neutrons were measured by means of a $5''\phi \times 5''$ NE213 liquid scintillator. The neutron pulse was separated from the gamma ray pulse by a pulse shape analysis (PSA) method.⁵⁷⁾ Typical examples of light output from liquid scintillator versus PSA output are given in fig. 2-10. A lead absorber with thickness $2 \sim 3\text{cm}$ was used in front of the neutron detector to reduce gamma rays. In some cases we employed plastic scintillator with 5mm thickness which was set just in front of the liquid scintillator to reject charged particle (mainly protons). The effect of the 2cm lead absorber on the liquid scintillator light output is shown in fig. 2-11. These data and other lab. data⁹⁴⁾ show that the absorber does not distort much the pulse height spectrum.

The small effect due to the lead absorber was corrected for. The energy ($1 \sim 3$ MeV) per channel and the energy resolution ($1 \sim 3$ MeV) of the present neutron spectrometer are sufficient to select high energy neutrons for the angular distribution measurements, and to give rough shape of the continuous energy spectra characteristic of the preequilibrium

or equilibrium process. The neutron spectrometer has an advantage of the large solid angle (~ 0.2 sr.), which is essential for the present coincidence work, over a conventional TOF method. Contributions of neutrons scattered from the lead shields, and other detectors to the neutron detector were checked and found to be negligible in the present coincidence experiment.

Discrete gamma rays of rotational transitions, being characteristic of the residual nuclei, were detected by the coaxial type 55cc Ge(Li) detector.

The LEPS, the coaxial Ge(Li) and the liquid scintillator were set typically 75 \sim 100mm, 160mm, and 220mm far from the target, respectively. The counter arrangement is shown schematically in fig. 2-3. The typical electronics circuits are shown in fig. 2-9.

The counting rates with 0.8 nA of 120 MeV alpha particles on ^{164}Dy target with 3.3mg/cm^2 thickness were typically 2.2kc/s for the coaxial Ge(Li), 0.65kc/s for the LEPS and 6kc/s for the 5" diam. \times 5" liquid scintillator. The $n-\gamma$ coincidence rate with the coaxial Ge(Li) detector and the liquid scintillator was around 10c/s. The accidental coincidence rate was less than 2%. The dead time of the LEPS detector was negligible.

§ 3 Results

3.1 Cross Sections for the Preequilibrium and Equilibrium Reactions

Many rotational gamma rays for even A and odd A nuclei were observed in the detailed singles gamma ray spectra taken by the LEPS or/and the Ge(Li) detector. Typical examples of the gamma ray spectra obtained by the LEPS are shown in figs. 3-1, 3-2. Following quantities are obtained from these singles spectra i) $\sigma(E_T)$; cross sections for reaction channels, ii) I_m ; median spin values of the ground band levels, iii) R_k ; K-isomer ratio. In what follows we discuss these quantities in detail.

i) $\sigma(E_T)$ Cross Sections

Total reaction cross sections leading even-even residual nuclei may be approximately given by the cross sections of the ground band $2^+ \rightarrow 0^+$ transitions. The LEPS was very useful to detect these low energy (~ 100 keV) $2^+ \rightarrow 0^+$ transition. The cross section of the ground band $4^+ \rightarrow 2^+$ transition detected by the Ge(Li) detector was also used for convenience. Because the angular momentum involved in the present reaction is much higher than the $1\hbar = 4 \sim 2$, the intensities of the ground band (yrast) $4^+ \rightarrow 2^+ \rightarrow 0^+$ transitions give approximately the total

reaction cross-sections. The total cross sections for odd A and odd-odd residual nuclei are obtained as follows. The gamma decays in odd A isotope in Hf region are almost equally shared into several rotational bands, for example; $5/2^-$ [512], $7/2^+$ [633] and $1/2^-$ [521] bands. These low-lying rotational bands are well known from other inbeam gamma works.⁸⁶⁻⁹²⁾ The cross section for feeding each residual nucleus was obtained by summing up the intensities of the transitions (gamma rays and conversion electrons) for low-lying levels in these bands.

A rotational (yrast) band with positive parity is strongly populated in each odd Er isotope. It carries almost 40% of the total cross section.

The cross section was obtained from the observed intensity of the yrast band by referring to known population ratio for other bands. Uncertainty of the cross sections obtained from these methods is almost 30% for residual nuclei in the Hf region, and 15% for Er isotopes.

The corrections for isotopic impurity were also made and the largest correction was an order of 2% of the maximum cross section. The error in the absolute cross section is mainly due to the uncertainty of the target thickness.

The total reaction cross sections defined as $\sigma(E_T)$ are plotted as a function of the energy sum $E_T = \sum_{n=1}^x E_n$ of the decaying particles. The E_T is equivalent to the energy excess above the reaction threshold. It is given as

$$E_T = E_i + Q(x) - E_\gamma, \quad (3.1)$$

where $Q(x)$ is the ground state Q value for the $(\text{particle}, xn \text{ y} \gamma)$ reaction. The E_i is the incident particle energy, and the E_γ is the average excitation energy of levels populated by the $(\text{particle}, xn \text{ y} \gamma)$ reaction. The E_γ is taken away by the γ deexcitation. We ignore the shift of the Q value due to the rotational energy of the yrast level.

The relative cross sections induced by $^{174},^{176}\text{Yb}(\alpha, xn \gamma)\text{Hf}$ reactions at projectile energies $E_\alpha = 50, 70, 90$ and 120 MeV are shown as a function of E_T in fig.3-3. The prominent feature is that the cross sections for the small number (x) of emitted neutrons with large E_T are much larger than expected from the equilibrium (compound) process. This feature gets pronounced more as the projectile energy gets higher.

The $\sigma(E_T)$ for (α, xn) , $(\alpha, p xn)$, and $(\alpha, \alpha'xn)$ reactions induced by 120 MeV alpha on ^{164}Dy , $^{174},^{176}\text{Yb}$ are shown in figs.3-4-a,b. It is interesting to note that the sum of the cross sections for the $(\alpha, p xn)$ channels amounts as much as $70\% \sim 90\%$ of the sum of the cross sections for the (α, xn) channels. The cross sections for the $(\alpha, p xn)$ reactions are rather flat as a function of the number x of the emitted neutrons. The energy E_T at which the cross section is maximum in the $(\alpha, p xn)$ channels is about 5 MeV larger than that in the (α, xn) channels. For this target residual nuclei by $(\alpha, p xn)$ reactions are odd- Z nuclei and odd-odd nuclei unfortunately not studied by inbeam technique until now. Moreover to get the cross sections of odd A is a little bit

complicated and erroneous. To ascertain this phenomenon made a reaction by odd Z target. The $^{165}\text{Ho}(\alpha, p xn)$ Er reaction induced by 120 MeV alpha particles was studied since the decay schemes of the residual Er isotopes were well known. The cross sections are plotted in fig. 3-5. This figure shows clearly that the reaction cross sections involving proton decay are uniformly populated being insensitive to the number X .

We could also assign the gamma lines following $(\alpha, \alpha'xn, \gamma)$ reaction channels. The sum of the cross sections for $(\alpha, \alpha'xn)$ reaction channels was $15 \sim 30\%$ of the sum for the (α, xn) reaction channels. Here the gamma rays are assigned to the $(\alpha, \alpha'xn)$ reaction rather than the $(\alpha, 2p 2n xn)$ reaction because they are well observed in coincidence with the alpha particle. The $\sigma(E_T)$ for the (p, xn) and $(^3\text{He}, xn)$, $(^3\text{He}, p xn)$ reactions induced by various kinds of bombarding energy are summarized in figs 3-6, 3-7.

We introduce two quantities " E_M " and " S ". The E_M is the energy at which cross section is maximum and " S " is the slope of $\sigma(E_T)$ at large E_T region, being defined as

$$\sigma(E_T) = \sigma(E_M) \exp\left(-\frac{E_T - E_M}{S}\right). \quad (3.2)$$

It is interesting to find in every figure that S gradually increases with increase of the bombarding energy and it is much larger than expected from a prediction of a simple compound reaction. Thus most of the cross sections at large E_T (small x)

are due to the preequilibrium process. In fig. 3-8, 3-9 we summarize the present experimental results for E_M and S . The error for each results were estimated from the $\sigma(E_T)$ figures for the observed cross sections. It is interesting to point out that the relation of E_M to S of proton is much different from that of other projectile (${}^3\text{He}$, α). It indicates that the cross-sections at large E_T region are more pronounced for proton projectiles.

ii) I_m ; Median Spin Value

The median spin I_m is defined by

$$\frac{1}{2} = \frac{\sum_{I=4}^{I_m+1} P(I)dI}{\sum_{I=4}^{\infty} P(I)dI}, \quad (3.3),$$

where $P(I)$ is the side feeding population of the yrast level with spin I . The $P(I)$ is obtained as a difference $Y(I) - Y(I-2)$, where $Y(I)$ is the intensity of the gsb $I \rightarrow I-2$ transition.

Note that the I_m is practically obtained from the observed yield $Y(I)$ by a relation $Y(I_m+1) = Y(4)/2$. Thus the error in the I_m is fairly small although the error in the $P(I)$ is large. The yields $Y(I)$, normalized as $Y(4) = 1$, of the gsb's following the $^{174}\text{Yb}(\alpha, 6n)^{172}\text{Hf}$ reactions at three different bombarding energies are plotted in fig. 3-10. The I_m values for various kinds of projectiles and energies are summarized in figs. 3-11-a,b. The obtained I_m values increase very slowly as E_α goes from 50 to 120 MeV. They are much smaller ($\approx I_m(\text{CN})/2$) than the mean value ($I_m(\text{CN}) = I_{\text{max}}/\sqrt{2}$) introduced by the alpha particle (see fig. 3-11-a). The striking feature is that the I_m values for a given reaction channel are rather flat in a wide range of the E_α energy. The I_m values for different exit channels induced by 70, 90 and 120 MeV alpha particles on $^{174},^{176}\text{Yb}$ are plotted as a function of the energy excess E_T in fig. 3-12. The I_m 's for the large E_T region, where the preequilibrium process is important, are definitely smaller than

those for the small E_T region. It indicates that neutrons from the preequilibrium process take away more angular momenta than those from the equilibrium process.

iii) K-isomer Ratio

The K-isomer ratios for ^{172}Hf , ^{174}Hf and ^{182}Os following (particle, $\text{xn } \gamma$) reactions were studied. ^{172}Hf and ^{174}Hf has K-isomer with $I^\pi K = 6^+$ at 1685 keV and 1252 keV, respectively. The isomeric transitions are 1056 keV ($6_g \rightarrow 6_g$) and 1376 keV ($6_g \rightarrow 4_g$) for ^{172}Hf and 941 keV ($6_g \rightarrow 6_g$) and 1252 keV ($6_g \rightarrow 6_4$) for ^{174}Hf , where I_g is the gsb state with spin I and 6_g is the K-isomer. The K-isomer in ^{172}Hf was rather weakly populated. The contribution of the nearly 937 keV (^{18}F) background line to the 941 keV isomeric transition in ^{174}Hf had to be carefully corrected for. The ^{182}Os has K-isomer with $I^\pi K = 8^- 8$ at 1832.5 keV. It decays to the gsb 8^+ state by the 554.7 keV gammas. The 483.6 keV $8_g^+ \rightarrow 6_g^+$ gamma line has small contribution from 484.1 keV line of ^{183}Re $\frac{9}{2}^- \rightarrow \frac{7}{2}^+$ transition. It has been corrected for by referring to the known intensity ratio⁹⁴⁾ and the measured intensity of the ^{183}Re 384.1 keV transition. The correction is an order of $10 \sim 7\%$.

The intensities of the K-isomers were obtained normally from single spectra (prompt + delay). Delayed gamma ray spectra were also used in some cases. Typical examples of the gamma ray spectra following the $^{182}\text{W}(\text{He}^3, 3n\gamma) ^{182}\text{Os}$ at $E(\text{He}^3) = 31$ MeV are shown in fig. 3-13.

The K-isomer population ratio "R_k" is defined by;

$$R_k = \frac{P_k(I\pi)}{P_0(I\pi)} \quad (3.4)$$

where P₀(I^π) : population of the level with spin I in the ground band, excluding the contributions from the K-isomer band,

P_k(I^π) : population of the K-isomer.

Then $R_k = \frac{P_6(6^+)}{P_0(6^+)}$ for the Hf isotopes and $R_k = \frac{P_8(8^-)}{P_0(8^+)}$ for the ¹⁸²Os. Populations for the K-isomers in ^{172,174}Hf were obtained in some cases only from the $6_6^+ \rightarrow 6_g^+$ transition by referring to the known branching ratio.^{8,83)} [¹⁷²Hf: Y($6_6 \rightarrow 4_g$) / Y($6_6 \rightarrow 6_g$) = 2.3, ¹⁷⁴Hf: Y($6_6 \rightarrow 6_g$) / Y($6_6 \rightarrow 6_g$) = 1.0]

They are plotted here, for convenience, as a function of the median spin I_m in figs. 3-14-a,b (other lab's data are also included).

It is clear in these figures that the isomer ratios do not depend much on I_m, but do depend on the projectile. The isomer ratios for the proton induced reactions are definitely larger by a factor 1.5 ~ 2.0 than those of following the complex projectiles.

3.2 Neutrons following $^{164}\text{Dy}(\alpha, xn)$ and $^{165}\text{Ho}(p, xn)$ Reactions

Typical gamma ray spectra in coincidence with neutrons following $^{164}\text{Dy}(\alpha, xn)E_r$ reactions induced by 120 MeV alpha particles are shown in fig. 3-15. The neutron channels $1 \sim 8$ correspond, respectively, to the recoil proton energy windows of 2.5-3.5, 3.5-5.1, 5.1-6.8, 6.8-9.8, 9.8-12.4, 12.4-15.0, 15.0-17.6, and 17.6-20.1, all in MeV units. These values correspond to the maximum energies of the neutrons. It is remarkable that intensities of the gamma rays following (α, xn) reactions with large x are large at the lower energy window (the first $1 \sim 2$ channels). They decrease rapidly as the neutron energy increases. The gamma rays due to the reaction with small x , however, are not prominent in the spectra at the lower energy windows and are seen even at the higher energy bins. Thus the small xn reaction channels have a component of high energy neutrons. This is clearly seen in fig. 3-16 where the pulse height spectra are plotted as a function of \bar{E}_n for various reaction channels. Neutron energy spectra may be extracted by unfolding these pulse height spectra. There are two ways to unfold the pulse height spectra, a differential method and a response matrix method.

i) Differential method

The neutron energy spectrum $N^\alpha(E_i)$ for the reaction channel α was extracted from the yield of such gamma rays following the reaction channel α that were in coincidence with the neutron pulse in the i -th pulse height window. It is

$$N^\alpha(E_i) = (Y_i^\alpha/\Delta E_i - Y_{i+1}^\alpha/\Delta E_{i+1}) \bar{E}_i / \epsilon_i$$

where Y_i^α is the yield of gamma rays due to the reaction channel (residual nucleus) α , ΔE_i is the width of the i -th neutron energy window, \bar{E}_i is the mean energy of the neutrons in the i -th window, and ϵ_i is the absolute efficiency of the NE213 for the \bar{E}_i . Here we assumed that the recoil protons were isotropic in the liquid scintillator, and the value for ϵ_i was taken from the fig. 2-7⁵⁵⁾.

ii) Response matrix method

This method was developed by V.V.Verbinski⁵⁶⁾. His method is as follows;

The pulse height distribution of a NE213 is related to the unknown neutron spectrum $N_n(E)$ by

$$\bar{C}_i = \int_0^{\infty} A_i(E) N_n(E) E$$

where: $A_i(E)$ = probability that a neutron with energy E gives a pulse height in i -th channel,
 $N_n(E)$ = neutron energy spectrum,
 \bar{C}_i = counts in channel i .

The efficiency function $A_i(E)$ can be measured, or can be computed by a Monte Carlo computer program as described in the previous section. This is conventional for extracting the neutron spectrum from the measured pulse height spectrum. Although this does not include statistical fluctuations \sqrt{C} and various instrumental distortion the results show good agreement with the spectrum obtained by a time of flight method⁹⁵⁾. The $A_i(E)$ for the present analysis was obtained by a Monte Carlo calculation. It agreed with the measured one by use of a TOF method.

The neutron energy spectra were obtained by two different methods as mentioned above. They agree with each other as shown in fig. 3-17.

Systematic errors of the energy spectrum are around 20% in both the intensity and energy.

The extracted neutron spectra for various reaction channels are plotted in figs. 3-18-a,b. Only statistical errors are given in the figs. The arrows in the figures

show the mean neutron energies $\bar{E}_n = E_T/X$. All the neutron spectra have a high energy part and a low energy part. The former is conspicuous at forward angles, and in the small xn reaction channels.

Angular distributions for these neutrons are shown in figs. 3-19-a,b. The preequilibrium process is important in the (α, xn) reaction with the small x which shows predominantly forward peaking distributions. Even the reaction with large x has also a forward peak distribution. The forward peaks are mainly due to the high energy components. The coefficients of the Legendre polynomial expansions $\sum A_i P_i(\cos\theta)$ for the angular distributions are plotted as a function of E_T in figs. 3-20-a,b.

The equilibrium process gives a symmetric distribution in the cm (center of mass) frame, and a small asymmetry of $A_1^e = 0.13$ in the lab. system for $(\alpha, 10n)$ reaction induced by 120 MeV alpha particles on ^{164}Dy . The A_1^e for the (α, xn) reaction decreases as the number x decreases (for example $A_1^e = 0.08$ for $x = 6$). The observed asymmetry terms are much larger than the A_1^e in every case and this fact suggests clearly some preequilibrium process for every reaction channel. $A_2 P_2(\cos\theta)$ term through compound nuclear reaction can be estimated from the formula obtained by Ericson and Strutinski⁹⁶⁾. There the $P_2(\cos\theta)$ term was given by

$$W(\theta) \propto 1 + A_2 P_2(\cos\theta) ,$$

$$A_2 = \frac{2\xi}{3+\xi} ,$$

$$\xi = \frac{1}{2} \alpha^2 \bar{I}^2 \bar{\ell}^2 ,$$

$$\alpha = \frac{\hbar^2}{2JT} ,$$

where T is the nuclear temperature, J is the moment of inertia and \bar{I}^2 and $\bar{\ell}^2$ are averages of I^2 and ℓ^2 . This gives $A_2^e \approx 0.002$ for a typical case of $^{164}\text{Dy} + 120$ MeV α reactions where $I_{\max} \approx 30$, $\ell_n \approx 2 \sim 7$. Here use was made of rigid-body moment of inertia values. The observed A_2 values have definitely larger than the A_2^e and this fact also suggests some contributions from the preequilibrium process.

§4 Analysis

4.1 An Exciton Model

The exciton model is one of the useful method to analyse the preequilibrium process. Here we do not give a complete survey of various kinds of exciton models²⁹⁻⁴²⁾, but we briefly follow the exciton model given by S. Yoshida in ref. 38. The theoretical foundation of this model was given by Agassi et. al.⁹⁷⁾. The equilibration process is described by a Pauli master equation as

$$\frac{d}{dt} P_n(t) = \sum_m W_{mn} [\rho_n P_m(t) - \rho_m P_n(t)] , \quad (4.1)$$

where the $P_n(t)$ is the occupation probability of n exciton state (a state with exciton number n) at time t , the $W_{mn} = W_{nm}$ is a mean value of the square of the transition matrix elements, and the ρ_n is the level density of n exciton state. The master equation (4.1) expresses a balance between gain and loss of occupation probabilities. A conventional method to solve eq. (4.1) is a numerical integration. The numerical integration method needs elaborate computations and moreover it is rather difficult to get better physical understanding. The Yoshida's method is to diagonalize the kernel. The master equation is expressed³⁸⁾ as

$$\frac{dp(t)}{dt} = - \frac{1}{\hbar} \sqrt{2\pi\rho} Q \frac{1}{\sqrt{2\pi\rho}} P(t) , \quad (4.2)$$

where the Q is the real symmetric matrix and the ρ is the level density. The solution of the master equation is

$$P_{mm_0}(t) = \sum_j C_{mm_0}^j e^{-q_j t/\hbar} \quad \textcircled{H}(t) , \quad (4.3)$$

where q_j and $C_{mm_0}^j$ are related as

$$\tilde{Q}Q = q = \text{diagonal}$$

matrix, and the $\textcircled{H}(t)$ is a step function,

$$\textcircled{H}(t) = 1 \quad t \geq 0$$

$$\textcircled{H}(t) = 0 \quad t < 0 .$$

The time development function⁹⁸⁾ for transition $a \rightarrow b$ is given by

$$F_{ab}(t) = \frac{1}{\hbar} (1 + \delta_{ab}) \sum_m \tilde{T}_{bm}^\dagger \frac{1}{2\pi\rho_m} P_{mm_0}(t) T_{m_0 a}^\dagger , \quad (4.4)$$

where T_{mb}^\dagger is the transition probability from a channel b to an exciton state m (exciton number m). Various quantities are derived from this expression. For example if the time development function is integrated over time, one gets the particle emission probability, as

$$\int_{-\infty}^{\infty} dt F_{ba}(t) = (1 + \delta_{ab}) \sum_m \frac{1}{2\pi\rho_m} T_{bm}^\dagger \sum_j C_{mj} / q_j \cdot T_{m_0 a}^\dagger , \quad (4.5)$$

The time for the compound system to reach to an equilibrium is called the equilibration time T_{eq} . It is defined as the time which the time dependent probability gets 99% overlap with the equilibrium distribution. The overlap is defined as

$$I(t) = \sum_m (P_{mm_0}(t) P_{mm_0}(\infty))^{\frac{1}{2}}. \quad (4.6)$$

Then the equilibration time is obtained from the relation

$$I(T_{eq}) = 0.99.$$

The fraction "f" of the preequilibrium decay is defined as the fraction of the probability of particle emission before the system gets equilibrium ($t < T_{eq}$), i.e.

$$f = \frac{\sum_b^{\infty} \int_0^{T_{eq}} F_{ba}(t) dt}{\sum_b^{\infty} \int_0^{\infty} F_{ba}(t) dt}. \quad (4.7)$$

The angular distribution of nucleon in the preequilibrium process is obtained by generalizing the master equation,

$$\frac{d}{dt} P_{mm_0}(\Omega, t) = \sum_k \int d\Omega' P_{km}(\Omega', t) W_{k \rightarrow m}(\Omega' \rightarrow \Omega) - \frac{1}{\hbar} (\Gamma_m^+ + \Gamma_m^-) P_{mm}(\Omega, t) \quad (4.8)$$

where Γ_m^+ and Γ_m^- are the decay and spreading widths, respectively. The angle dependent part in $W_{k \rightarrow m}(\Omega' \rightarrow \Omega)$ is assumed to be inde-

pendent of the exciton number and to be isotropic in the center of mass system.

The level density is

$$\rho_m(E, A, P) = G_A (G_A E)^{m-1} / [P! h! (m-1)!] , \quad (4.9)$$

where E is the excitation energy, A is the mass number of the compound system, and p, h and m are, respectively particle, hole, and exciton numbers ($m=p+h$). The single particle level density at the Fermi energy G_A is assumed to be

$$G_A = \frac{A}{G_0} , \quad (4.10)$$

where G_0 is a single particle level density parameter. The spreading width is given as

$$\Gamma_m^{\downarrow} = 2\hbar\lambda(E) \left[\frac{1}{m+1} + ph(m-1)(G_A E)^{-2} \right] / C , \quad (4.11)$$

where $\lambda(E)$ is the nucleon-nucleon collision probability given by Kikuchi and Kawai¹⁴⁾. It is approximated as

$$\lambda(E) = [1.6 \times 10^{21} E - 6.0 \times 10^{15} E^2] \text{ sec}^{-1}^{4-5} , \quad (4.12)$$

where E is expressed in unit of MeV, and C is the reduction factor for the collision probability in a nucleus. The $\lambda(E)$ is related to nucleon mean free path (MFP) in the nucleus,

$$\begin{aligned}
 \text{MFP} &= \frac{V}{\lambda} \\
 &= 0.138 \times 10^{10} \frac{\sqrt{E}}{\lambda} . \tag{4.13}
 \end{aligned}$$

A large reduction means a longer mean free path. There are many arguments ^{99 ~ 101} on this reduction factor. The escape width is given as,

$$\Gamma_m^{\uparrow} = \frac{2MR^2}{m\hbar^2} \frac{P}{m} \frac{E}{G_A} \left(\frac{A-1}{A}\right)^{m-1} \frac{1}{2} \left[\left(\frac{E-B_n}{E}\right)^m + \left(\frac{E-E_p-V_{\text{coul}}}{E}\right)^m \right] , \tag{4.14}$$

where V_{coul} is the Coulomb barrier height,

$$V_{\text{coul}} = 1.44Z / [r_0(1+A^{1/3})] \text{ MeV} , \tag{4.15}$$

and R is the nuclear radius.

4.2 An application of the exciton model.

We measured neutrons and gamma rays from (i, xn yp za γ) reactions to study the preequilibrium and equilibrium deexcitation processes. The deexcitation process in the preequilibrium stage may be interpreted in terms of the exciton model. The exciton model deals with the first particle emitted under a given initial condition. We calculated preequilibrium fractions, deexcitation probabilities, neutron

energy spectra and angular distributions for the $(i, xn \gamma)$ reactions in terms of the exciton model. On the basis of these exciton model calculations we made simple calculations by using two parameters (temperatures) T_e and T_p for equilibrium and preequilibrium stages. There are two important parameters in exciton model calculation, the reduction factor "C" in eq.(4.11) and the single particle level density in eq.(4.10). We used the value $C=4.8$. This is simillar to those in refs.32 and 34 and somewhat smaller than the value in ref. 14 throughout the calculation. The single particle level density parameter was chosen to be $G_0=11.4$.

The fractions "f"'s for the preequilibrium emission for various incident energies and initial exciton numbers were obtained for proton and alpha projectiles. The results are shown in Fig.4-1. Contributions from various exciton states to the emission probability are shown in fig.4-2. We take a $^{164}\text{Dy} + 90$ MeV α reactions as an example. The 90 MeV excited nuclear system with the initial condition $(p, h) = (4, 0)$, where p and h are the particle and hole numbers, decays mostly at the preequilibrium stages with small exciton numbers around $4 \sim 6$, as shown in the fig.4-2. On the other hand the 70 MeV system with $(p, h) = (6, 3)$ decays partly at the preequilibrium stage with the small exciton number $6 \sim 10$ and partly at the equilibrium stage with the large exciton number ~ 32 . A 50 MeV excited nuclear system with the $(p, h) = (10, 8)$ decays mostly after the system gets the

equilibrium stage. In fig. 4-3 the energy spectra of the emitted nucleons are shown for $E_x = 90$ MeV ($p, h = (4, 0)$, 70 MeV (6, 3) and 50 MeV (10, 8) cases.

In fig. 4-4 the angular distributions of the emitted nucleons are shown at the same initial conditions. The strong forward peaking angular distribution which is characteristic feature of the preequilibrium process is nicely obtained and it is essentially due to the first few collisions.

We found followings from those figures.

- 1) The excited nucleon system produced by 90 MeV α particle [(particles, holes) = ($p, h = (4, 0)$)] bombardment of the ^{164}Dy decays mostly (~98%) by emitting a fast nucleon with $kT_p \approx 6$ MeV at the preequilibrium stage, leaving the residual system at ~70 MeV and the average excitons ($p, h \approx (6, 3)$). This residual system then emits a fast nucleon with 70~80% probability at the preequilibrium stage, and a slow neutron with 30~20% probability after the system gets equilibrium. Since the residual system has fairly low excitation energy (~50 MeV) and large numbers (~20) of the excitons, the deexcitation hereafter is mostly of the equilibrium process.
- 2) The excited nucleon system produced by $E_i = 120 \sim 60$ MeV projectiles decays first by the preequilibrium process, being followed by the equilibrium nucleon evaporation. Therefore the emitted particle spectrum consists of two components, the high energy (forward peaking) part due to the preequilibrium decay and low energy part due to the evaporation.

The fig. 4-5 shows a schematic picture of the preequilibrium and equilibrium deexcitation processes.

4.3 Analysis by a simple model

In order to get a simpler picture and a better insight into the complicated deexcitation process, we analyse these data in terms of a simplified pre-equilibrium-equilibrium deexcitation process. We use a simple analytical form

$$f_i(E_i) = c E_i \exp(-E_i/kT_i) , \quad (4.16)$$

for the energy spectrum of the i -th deexciting nucleon. Here the parameter T_i is the energy parameter for the i -th nucleon deexcitation. The T_i for the equilibrium stage is the normal temperature T_e used in a conventional statistical model. The T_i for the preequilibrium process depends on the exciton number and the level density. It stands for the mean energy of the nucleon emitted at the preequilibrium stage where only a small fraction of the nucleus is excited (heated). Thus it is larger than the T_e . Actually the energy spectrum calculated by the exciton model is approximately given by the eq. (4.16).

The energy spectrum of the total energy $E_T = \sum_i^x E_i$ of the x emitted nucleons is given by the probability to get E_T as

$$f_x(E_T) = c \int \prod_{i=1}^{x-1} f_i(E_i) f_x(E_T - \sum_{i=1}^{x-1} E_i) \prod_{i=1}^{x-1} dE_i . \quad (4.17)$$

Now we introduce two quantities A_x^{\uparrow} and A_x^{\downarrow} for the escape and spreading probabilities, respectively. They are defined

as follows (see fig. 4-6)

$$A_X^\uparrow = \int_{\alpha_1}^{\alpha_2} f_X(E_T) dE_T / \int_0^{\alpha_2} f_X(E_T) dE_T, \quad (4.18)$$

$$A_X^\downarrow = \int_0^{\alpha_1} f_X(E_T) dE_T / \int_0^{\alpha_2} f_X(E_T) dE_T, \quad (4.19)$$

Here $\alpha_2 = E_T^\alpha(\max) = E_0 + Q_\alpha$, $\alpha_1 = E_T^\alpha(\min) = E_p + Q_\alpha - B_\alpha$, where the Q_α is the ground state Q value, and B_α is the nucleon binding energy. Then the $(i, xn \gamma)$ reaction cross-section is approximately given by

$$\sigma_X = \sigma_n \cdot A_X^\uparrow \cdot \prod_{i=1}^{x-1} A_i^\downarrow, \quad (4.20)$$

where σ_n is the total $(i, xn \gamma)$ reaction cross-section.

The energy spectrum of the i -th emitted nucleon for a specific reaction channel α (x neutron emission) is

$$S_i(E_i) = C E_i \exp(-E_i/k T_i) \times \int \prod_{j \neq i}^x f_j(E_j) \cdot f_X(E_T - \sum_{j \neq i} E_j) \prod_{j \neq i}^{x-1} dE_j. \quad (4.21)$$

Let's consider a two step process of the preequilibrium and equilibrium deexcitations. Since the nuclear temperature and the energy parameter are slowly varying functions of the excitation energy, we use for simplicity constant (effective) values T_e and T_p throughout the equilibrium and preequilibrium deexcitation processes, respectively. Then the total energy spectrum is analytically obtained as

$$f_x(E_T n_p n_e) = C \int \exp(-E_p/kT_p) E_p^{2n_p-1} \exp(-(E_T - E_p)/kT_e) (E_T - E_p)^{2n_e-1} dE_p , \quad (4.22)$$

where $0 < E_p < E_T$, $n_p + n_e = x$, and $n_p(n_e)$ is the number of nucleons emitted at the preequilibrium (equilibrium) stage. The energy spectrum of the i -th nucleon emitted at the preequilibrium stage of the reaction channel α is written as

$$S_x^p(E_i, n_p n_e) = C E_i \exp(-E_i/kT_p) \int \exp(-E_p/kT_p) E_p^{2n_p-3} \times \exp(-(E_T + E_p)/kT_e) (E_T - E_p)^{2n_e-1} dE_p . \quad (4.23)$$

The energy spectrum for the equilibrium stage is obtained by exchange of parameters $n_p T_p \leftrightarrow n_e T_e$ in the eq. (4.23)

The angular distribution of the neutrons emitted at the preequilibrium and equilibrium phases is interpreted as follows. The linear momentum and energy introduced by the projectile are distributed over only a small fraction of the nucleons in the preequilibrium phase. Thus the active particles (A') of the excitons in the fraction carry the input linear momentum at the preequilibrium stage. The nucleons are then emitted isotropically in the center of the local mass (A') frame of the active exciton particles. They are emitted forward in the center of the total mass (A) frame because $A' \ll A$. On the otherhand the nucleons emitted in the equilibrium stage are nearly isotropic in the center of the total mass (A) frame, and thus are almost isotropic in the lab. frame.

This is essentially similar to the idea of the fireball model used for relativistic heavy ion reactions¹⁰²⁾. Then the angular distribution in the lab. frame is written as

$$\frac{d\sigma}{d\Omega} = \frac{\sin^2\theta}{\sin^2\theta_\ell} \cdot \frac{1}{\cos(\theta-\theta_\ell)} \cdot \frac{d\sigma}{d\omega} , \quad (4.24)$$

where $d\sigma/d\omega$ is the cross-section in the A' frame. The angles θ and θ_ℓ in the A' frame and the lab. frame are obtained from a relation

$$\sin(\theta-\theta_\ell) = \frac{V'}{V_b} \sin\theta_\ell , \quad (4.25)$$

where V' is the velocity of the hot part (active A' exciton particles), and V_b is the velocity of the emitted neutron in the center of the A' mass frame. Since actually $V' \ll V_b$, $\theta \approx \theta_\ell$, the eq. (4.25) is reduced to a simple form,

$$\frac{d\sigma}{d\Omega} = \frac{d\sigma}{d\omega} [1 + 2 \frac{V'}{V_b} P_1(\cos\theta_\ell) + (\frac{V'}{V_b})^2 P_2(\cos\theta_\ell)] . \quad (4.26)$$

For a simple case of the $d\sigma/d\omega = \text{constant}$ (isotropic distribution) for both the preequilibrium and equilibrium de-excitations, respectively, in the A' and A nucleon frames, we get

$$\frac{d\sigma}{d\Omega} = \frac{\sigma_0}{4\pi} [1 + 2 \frac{V'}{V_b} \frac{n_p}{x} P_1(\cos\theta_\ell) + (\frac{V'}{V_b})^2 \frac{n_p}{x} P_2(\cos\theta_\ell)] , \quad (4.27)$$

where $n_p = x - n_e$ is the number of nucleons emitted at the preequilibrium stage. In fact the $d\sigma/d\omega$ for the equilibrium process is not isotropic but has a $P_2(\cos\theta)$ term, which contributes a little to the last term of the eq. (4.27). The asymmetry term $A_1 P_1(\cos\theta_\ell)$, which is characteristic of the preequilibrium process, is proportional to the velocity V' and the n_p . Thus it is inversely proportional to the effective number (A') of the exciton particles at the preequilibrium stage.

A differential cross-section for a specific reaction channel $(\frac{d\sigma(i, xn)}{d\Omega dE})$ may be calculated by a Monte Carlo method, too. We assumed that neutrons are emitted isotropically in a center of the local mass frame and that the energy spectrum has the Maxwellian distribution with two parameters of T_p and T_e . The random number having the distribution of $E_e - E/T$ is generated by a rejection method. The deexcitation process of losing an excitation energy by emitting nucleons can be simulated and followed. From this calculation we can obtain the $(i, xn \gamma)$ reaction cross-sections and neutron energy and angular distributions simultaneously.

4-4 Comparison with Experimental Results

Numerical calculations were carried out by using the eqs. (4.18)-(4.27). At present, however, we are primarily interested in the qualitative features of the preequilibrium process. Therefore we bear in mind so as to reproduce the experimental results by using a few parameters. The calculated cross-sections using the equilibrium process only, decrease much faster than the experimental values as the energy excess E_T increases. The deviation is larger at higher bombarding energy (see broken lines in the figs. 3-3 ~ 3-6). As we have presented in the fig. 4-5, two different deexcitation paths exist to lead to the same reaction channel for 90 MeV alpha bombardment the cross-section may be written as follows

$$\sum_x \sigma(i, x n \gamma) = f_1 \sum_x \sigma(np, x-np) + f_2 \sum_x \sigma(np-1, x-np+1), \quad (4.28)$$

where the $\sigma(np, n_e)$ stands for the reaction cross-section with the np neutron deexcitation at the preequilibrium stage followed by the n_e neutron evaporation. They are normalized so as to get $\sum_x \sigma(np, x-np) = \sigma_n$, where σ_n is the observed total $(i, x n \gamma)$ cross section. The coefficients f_1 and f_2 can be obtained from preequilibrium fractions in fig. 4-1. The nuclear temperature T_e of medium heavy nuclei with $50 \sim 20$ MeV excitation energy is around $1.8 \sim 1.1$ MeV.¹⁰³⁾ The energy

parameter of the preequilibrium process can be obtained as follows; for Yb+120 MeV- α reaction almost three neutrons are emitted at the preequilibrium process (estimated from the figs. 4-1 and 4-2) and the energy parameter for the preequilibrium process is a mean value for the three neutron emission. Now we introduce quantities E_M and S , which are defined by an expression $\sigma(E_T) = \sigma(E_M) \exp[-(\frac{E_T - E_M}{S})]$ at large E_T region. They are plotted in the fig. 4-7 for the various energy parameters and the number of decaying neutrons at the preequilibrium stage. The dotted area is the region obtained by the experimental results (see figs. 3-3, 3-4). Thus we chose 7 MeV for the energy parameter. The energy parameters for other reaction case can also be obtained in the similar manner. Then the cross sections are expressed as,

$$\sum_x \sigma(\alpha, xn \gamma) = 0.5 \sum_x \sigma(1, x-1) + 0.5 \sum_x \sigma(0, x) \quad (4.29)$$

for $E_\alpha = 50$ MeV reactions,

$$\sum_x \sigma(\alpha, xn \gamma) = 0.9 \sum_x \sigma(1, x-1) + 0.1 \sum_x \sigma(0, x) \quad (4.30)$$

for $E_\alpha = 70$ MeV reactions,

$$\sum_x \sigma(\alpha, xn \gamma) = 0.8 \sum_x \sigma(2, x-2) + 0.2 \sum_x \sigma(1, x-1) \quad (4.31)$$

for $E_\alpha = 90$ MeV reactions and

$$\sum_x \sigma(\alpha, xn \gamma) = 0.7 \sum_x \sigma(3, x-3) + 0.3 \sum_x \sigma(2, x-2) \quad (4.32)$$

for $E_\alpha = 120$ MeV reactions.

The energy parameters of the preequilibrium stage were $kT_p = 6$ MeV for the reactions at $E_\alpha = 50, 70$ and 90 MeV, and $kT_p = 7$ MeV for the reaction at $E_\alpha = 120$ MeV. The temperatures of the equilibrium stage were $kT_e = 1.7$ MeV for $E_\alpha = 50, 70$ and 90 MeV reactions and $kT_e = 2$ MeV for $E_\alpha = 120$ MeV reaction by referring to the level density.¹⁰³⁾ The cross-sections induced by 60 MeV protons are expressed as

$$\sum_x \sigma(p, xn \gamma) = 0.35 \sum_x \sigma(2, x-2) + 0.4 \sum_x \sigma(1, x-1) + 0.25 \sum_x \sigma(0, x) \quad (4.33)$$

with $kT_p = 7$ MeV and $kT_e = 1.7$ MeV. The cross-sections are composed of three different deexcitation processes, being somewhat different from the $(\alpha, xn \gamma)$ reactions. This comes from the fact that the alpha particle being composed of 4-particles has more probability (larger spreading width) to create particle-hole pairs in the nucleus than the proton. The calculated results reproduce well the observed values as shown in the figs. 3-3, 3-4, and 3-6-b.

The slope of the cross-sections for the preequilibrium process ($large E_T \gg kT_e$) is approximately given by $\sigma \approx C \exp(-E_T/n_p \cdot kT_p)$ or $S \approx n_p \cdot kT_p$ as seen from the eq. (4.22).

The number n_p of the preequilibrium decay neutrons and the ratio $n_p/(n_p+n_e)$ for alpha particle induced reactions are calculated as shown in fig. 4-8. The mean number \bar{n}_p of the preequilibrium decay neutrons defined as $\bar{n}_p = \sum_x n_p \cdot \sigma(\alpha, xn \gamma) / \sum_x \Sigma \sigma(\alpha, xn \gamma)$ is also plotted as a function of the incident alpha particle energy in fig. 4-8. The $n_p/(n_p+n_e)$ values increase very rapidly with increase of the E_T . The n_p values with large energy excess E_T are large, while those with small E_T are small. In other words the large E_T region has more contribution from the preequilibrium process. The obtained \bar{n}_p values increase from 0.4 to 2.7 as the E_α goes from 50 to 120 MeV. Projection of the eq. (4.32) of 120 MeV- α reaction on the individual $(\alpha, 4n)$ and $(\alpha, 11n)$ reactions gives

$$\sigma(\alpha, 4n) = 0.90\sigma(3, 1) + 0.10\sigma(2, 2), \quad (4.34)$$

$$\sigma(\alpha, 11n) = 0.41\sigma(3, 8) + 0.59\sigma(2, 9). \quad (4.35)$$

The (α, xn) reactions with $x = 4 \sim 6$ are mainly due to three preequilibrium decay neutrons, while those with $x = 9 \sim 11$ are due to the combinations of two and three preequilibrium decay neutrons. Projection of the eq. (4.29) ($E_\alpha = 50$ MeV reaction) on the individual $(\alpha, 2n)$ and $(\alpha, 4n)$ reactions gives

$$\sigma(\alpha, 2n) = 0.99\sigma(1, 1) + 0.01\sigma(0, 2), \quad (4.36)$$

$$\sigma(\alpha, 4n) = 0.35\sigma(1, 1) + 0.65\sigma(0, 2). \quad (4.37)$$

If one neutron is emitted at the preequilibrium stage, the (α, xn) reactions with $x = 2 \sim 3$ are likely, while the (α, xn) reactions with $x = 4 \sim 5$ are likely for the equilibrium phase.

The cross-sections following (${}^3\text{He}$, $\text{xn}\gamma$) reactions induced by 80 MeV ${}^3\text{He}$ particles are also expressed in a similar way as

$$\sum_x \sigma({}^3\text{He}, \text{xn}\gamma) = 0.8 \sum_x \sigma(1, x-1) + 0.2 \sum_x \sigma(2, x-2) \quad (4.38)$$

with $kT_p=6$ MeV and $kT_e=1.7$ MeV. The calculated values by using the eq. (4.38) reproduce well the observed values as shown in the fig. 3-7.

The calculation of the cross-sections for the (${}^3\text{He}$, $\text{pxn}\gamma$) reaction where a charged particle is emitted is rather complicated. For simplicity we assume that protons with energy below the Coulomb barrier are suppressed, and that the proton emission takes place at the beginning of the doorway for the projectile-target collision process. The Coulomb barrier energy for proton is expressed as

$$E_B = \frac{Z_e^2}{R_0} \cdot \frac{Z}{A} \text{ MeV} \quad (4.39)$$

where R_0 is the nuclear radius and the Z and A are charge and mass of the residual nucleus, respectively. The calculated result under these assumptions is shown in fig. 3-7. Here we used the same parameters as used in the eq. (4.38). The predicted cross-sections are not in good agreement with the experimental results at the large E_T region. The similar disagreement is also seen in the ${}^{165}\text{Ho}(\alpha, \text{pxn}\gamma)\text{Er}$ reaction (see fig. 3-5). We have to know the energy and angular distributions of the emitted proton to get better agreements.

The neutron energy spectra for the $(\alpha, 6n)$ and $(\alpha, 8n)$ reactions induced by 120 MeV alpha particles were calculated in terms of the preequilibrium and equilibrium processes (eqs. 4.23, 4.32) and shown in fig. 4-9. The energy sums of the emitted neutrons of these reaction channels are as large as $E_T = 66.4$ MeV and 50.4 MeV and the average energies per neutron are $E_n \sim 11$ MeV and ~ 6.3 MeV, for the $(\alpha, 6n)$ and $(\alpha, 8n)$ reactions respectively. Thus even the neutrons evaporated from the equilibrium stage must have fairly large energy in order to result in the $(\alpha, 6n)$ and $(\alpha, 8n)$ reactions. The successive emissions of most probable neutrons with $E_n \sim kT_e$ would result in $(\alpha, 10n)$ or $(\alpha, 11n)$ reactions. Since most of these low energy neutrons following the $(\alpha, 10n)$ reaction are below the present lower limit for the neutron detector, we do not discuss the energy spectrum for this reaction channel. The neutron energy spectrum for the $(p, 4n)$ reaction is also calculated in the similar manner (fig. 4-10) by using the eqs. (4.23) and (4.33).

The angular distributions of the neutrons following the (α, xn) reactions induced by 120 MeV alpha particles were calculated by using the eqs. (4.27) and (4.32). The number of neutrons emitted at the preequilibrium stage was obtained from the fig. 4-8. The kinetic energies E_b of the neutrons emitted at the preequilibrium stage were assumed to be 14, 10 and 7 MeV for the $(\alpha, 6n)$, $(\alpha, 8n)$ and $(\alpha, 10n)$

reactions, respectively, and the average number of exciton particles was assumed to be $A'=8$. These values for the E_b and A' are based on the exciton model calculation. The calculated A_1 and A_2 values reproduce well the observed one as shown in the fig.3-20-a. The angular distributions of the neutrons following (particle, xn) reactions induced by 90 MeV alpha particles and by 60 MeV protons were also calculated in the similar manner as shown in figs.3-19-b,3-20-b.

The observed asymmetry term A_1 is related to the calculated (raw) A_1 term as $A_1 = \frac{n_p}{x} A_1'$, where n_p is the number of nucleons emitted at the preequilibrium stage (eq. 4.27). The observed A_1 is reduced by a factor n_p/x . If the nucleon-nucleon cross section is assumed to be isotropic in the center of mass system, the A_1' term in the lab. system is given by $A_1' = 2$. The $A_1 x$ values are around 5 as shown in the fig. 4-11 for the α -120 MeV reactions. Then we get the value $n_p \approx 2.5$ being similar to one obtained in the fig. 4-8 where $\bar{n}_p \approx 2.8$.

§ 4.5 Analysis of the K-isomer ratio

We analyze the observed isomer ratio in terms of a simple function of the median spin of the input angular momentum \bar{I}_i of the projectile and the mass number A_i . It is

$$P_K(J)/P(J) \equiv P_K(J)/(P_0(J) + P_K(J)) = g(\bar{I}_i) f(A_i).$$

The $g(\bar{I}_i)$ is the statistical factor which has been treated on the K-band deexcitation model.^{8,43)} Here levels with K larger than a critical value K_C feed the K-isomer. Thus

$$g(\bar{I}_i) = \frac{\sum_{K=1}^{K_m} \rho(K)}{\sum_{K=1}^{K_m} \rho(K)},$$

where $\rho(K)$ is the K distribution, and K_m is the maximum K.

We use the $K_m = 12$ which corresponds to the maximum K of the two quasi-particle states if $I_i \geq 12$, and the $K_m = I_i$ if $I_i \leq 12$. (note $I_i > K$). Use of the K_m larger than 12 changes little the $g(\bar{I}_i)$ because the number of levels with $K > 12$ is anyway quite small. The K distribution is obtained from the refs. 109 and 110. as $\rho(K) = \exp(-0.01K^2)$ for the $2 \sim 4$ quasi-particle states at about 4-8 MeV excitation energy. The critical value K_C depends on the location of the K-isomer and other high K levels , and we use for the ^{182}Os the $K_C = 5$ because the levels with $K \leq 4$ may decay directly or through the $K = 2$ γ -band levels to the gsb. The function $f(A_i)$ should be such that the value $f(A_i)$ is unity at the extreme case of $A_i = 0$ and approaches to zero at $A_i \approx$ target mass. In the former there is no mass effect, and in the latter the whole compound nucleus has a

new symmetry axis perpendicular to the input momentum of the heavy mass projectile and rotates with $K=0$. We use for such a function a simple form $f(A_i) = \exp(-bA_i)$. Thus one gets finally

$$P_K(J)/P(J) = \frac{\sum K_m \exp(-aK^2)}{\sum K_C \exp(-aK^2)} (\exp(-A_i/\lambda)),$$

where $K_m = 12$ for $I_i \geq 12$ and $K_m = I_i$ for $I_i < 12$, $a = 0.01$, and $K_C = 5$. The observed values are well reproduced by choosing the value $\lambda = 8$.

Similar features of the projectile dependence are observed in the isomer of $J^{\pi}K = 6^+$ in the $^{172},^{174}$ Hf. Here the dependence is less clear than in the ^{182}Os case because the reactions available for comparison are in the low angular momentum range where the K -isomer depends on the angular momentum.

§5 Discussions

i) Very few measurements of neutron spectra following (particle, $xn\gamma$) reactions have been reported^{117,118}, since they required elaborate techniques. Neutron energy and angular distributions were successfully measured by use of a single stilbene scintillator crystal as a neutron spectrometer by Broek for the first time¹¹⁷. Detailed angular distributions were measured by means of nuclear emulsions, using the internal-radiator method. The n-p collision occurring within the emulsion itself serves to evaluate the neutron flux¹¹⁸. These two works aimed to study the effect due to high angular momentum introduced by 160MeV ^{16}O ions on the compound (equilibrium) reaction process.

The present study differs obviously from their data in the following points; i) the present neutrons were measured by use of an organic liquid scintillator NE213 as a neutron spectrometer and were identified to the specific reaction channels by requiring coincidence with specific discrete gamma-rays, while they measured inclusively whole neutrons without identifying the reaction channels. ii) the present projectile energies ($E_p = 60\text{MeV}$, $E_\alpha = 22.5, 30\text{ MeV/amu}$) are much higher than their values ($E_{^{16}\text{O}} = 10\text{MeV/amu}$) and this is essential to study the preequilibrium process. As a result we found characteristic behaviours of the preequilibrium process in neutron energy and angular distributions.

Very recently the multiplicity of neutrons in the inelastic scattering of 7.5 MeV/amu ^{132}Xe ions from ^{197}Au have been studied as a function of total energy loss by Gould et al¹¹⁹. Use of

two NE213 liquid scintillators were made as neutron detectors.

Coincidence between inelastically scattered ^{132}Xe ions and emitted neutrons were made. They found that the absolute multiplicity values are lower than expected and these suggest the significant preequilibrium effect. Thus the neutron-gamma coincidence measurement is very useful to study the reaction mechanism and should be employed more widely.

ii) A number of works^{7,8,104-108)} have been carried out to investigate angular momentum transfer through (particle, $xn\gamma$) reactions. They are studied mostly by gamma-ray multiplicity measurements. The spin of the entry state I_γ (see fig. 1-1) where gamma-decays start can be obtained simply by using the relation $I_\gamma = 2(M_\gamma - 3)$, where M_γ is the multiplicity. Very recently systematic studies of the γ -ray multiplicity through the (α , $xn\gamma$) reactions in an energy range of $E_\alpha = 40 \sim 110$ Mev^{106,111,116} have been carried out by using a multi-detector system. They gave higher moments of multiplicity, σ_M (standard deviation) and/or S_M (skewness), together with multiplicity M_γ . Using these values they could deduce the angular momentum distributions at the entry state. They found that the multiplicity for (particle, xn) reactions with small x , where the preequilibrium process is important, is smaller than those for reactions with large x . On the other hand the preequilibrium process is considered to occur at the outer part of the nucleus, transferring large angular momentum. It is considered that the fast neutron emission at the preequilibrium stage takes out large angular momentum. Thus the measurements of energy and angular distributions of the decaying neutrons is essential to clarify the angular momentum carried out by the neutrons at the preequilibrium stage of the (particle, $xn\gamma$) reactions.

The present systematic studies on cross-sections $\sigma(E_T)$, median spins I_M and neutron energy and angular distributions

$d\sigma_n(xn)/d\Omega \cdot dE$, together with the γ -ray multiplicity data are useful to understand the angular momentum transfers through neutron and gamma deexcitation processes of the (particle, $xn \gamma$) reactions. The angular momenta removed by the deexciting neutrons are evaluated as follows. The neutrons from the equilibrium stage carry small angular momenta because their energies are small. They are mostly of p and d waves. Therefore the spin change $\Delta\ell_n$ (eq.) by the neutron evaporation is evaluated to be $\Delta\ell_n \approx 3-4$ for the 90-120 MeV alpha projectiles, and it is small ($\Delta\ell_n \lesssim 0.5$) for the 60 MeV proton projectile. Angular momenta removed by the fast neutrons emitted at the preequilibrium stage may be estimated as follows;

$$\begin{aligned} \ell\hbar &= \vec{r} \times \vec{p} \\ &= r \cdot \sin\theta \cdot \bar{P}W(\omega) \cos\omega, \end{aligned} \quad (5.2)$$

where \bar{P} is the average momentum, $W(\omega)$ is the angular distribution of the fast neutron being defined by

$$W(\omega) = 1 + A_1' P_1(\cos\omega) + A_2' P_2(\cos\omega),$$

and θ and ω are the direction angles of r and \bar{P} with respect to the incident particle. After the average of all over the nucleus and taking into the number of preequilibrium neutrons, we get

$$\bar{\ell}_n \hbar \sim \frac{\pi}{16} n_p A_1' \bar{P} R, \quad (5.3)$$

where R is the nuclear radius, n_p is the number of the neutron emitted at the preequilibrium phase. The quantity $n_p \cdot A_1'$ is obtained from the observed A_1 coefficient by using a relation $A_1 = n_p A_1' / x$. The \bar{P} is approximately obtained from the observed mean energy E_n . As an example hereafter we will consider mainly the reaction induced by 120 MeV alpha particles. The mean energies are ~ 25 , ~ 15 and ~ 7 MeV for the preequilibrium neutrons due to the $(\alpha, 6n \gamma)$, $(\alpha, 8n \gamma)$ and $(\alpha, 10n \gamma)$ reactions, respectively. Here we assumed that R is $1.4 \cdot A^{1/3}$. Finally we obtained the values $\bar{\ell}_n \hbar \sim 8.3\hbar$, $\sim 6.4\hbar$ and $\sim 4.4\hbar$ for the $(\alpha, 6n \gamma)$, $(\alpha, 8n \gamma)$ and $(\alpha, 10n \gamma)$ reactions, respectively. Since most of the low energy neutrons following the $(\alpha, 10n \gamma)$ reaction are below the present lower limit for the neutron detector, the obtained value $\bar{\ell}_n \hbar \sim 4.4\hbar$ for the $(\alpha, 10n \gamma)$ reaction may be overestimated. On the other hand, the $(\alpha, 6n)$ reaction has the neutrons higher than present upper limit of the neutron detector. Thus the obtained $\bar{\ell}_n \hbar$ value for the $(\alpha, 6n)$ reaction may be underestimated.

Our preliminary data¹¹¹⁾ on the γ -ray multiplicity measurements at $E_\alpha = 120$ MeV give $I_\gamma \hbar \sim (16 \pm 3)\hbar$, $\sim (15 \pm 3)\hbar$, and $\sim (13 \pm 3)\hbar$ for $(\alpha, 10n)$, $(\alpha, 8n)$ and $(\alpha, 6n)$ reactions, respectively. Angular momenta removed by the statistical decay neutrons are estimated as $\sim 3.7\hbar$, $\sim 3.2\hbar$ and $\sim 2\hbar$ for $(\alpha, 10n)$, $(\alpha, 8n)$ and $(\alpha, 6n)$ reactions, respectively. Combining these results, the mean values $I_c \hbar \sim I_\gamma \hbar + \bar{\ell}_n \hbar$ for the spin population at the initial (pre)compound system is

obtained as $I_c \hbar \approx (23.3 \pm 3)\hbar$, $(24.6 \pm 3)\hbar$ and $(24.1 \pm 3)\hbar$ for $(\alpha, 6n \gamma)$, $(\alpha, 8n \gamma)$ and $(\alpha, 10 \gamma)$ reactions, respectively.

The mean spin I_c' of the initial spin population introduced by the 120 MeV alpha particle is estimated using the relation $I_c' = 2 \cdot I_{\max} / 3$, where I_{\max} is the maximum angular momentum and corresponds to the impact parameter equal to the nuclear radius. Then we get $I_c' \hbar \approx 24\hbar$. The obtained $I_c \hbar$ values are very close to the mean spin value I_c' . It indicate that even $(\alpha, 6n)$ reactions where preequilibrium process is important is considered to be originated from collisions with a whole of the nucleus. Thus we can not conclude from the present experimental results that the preequilibrium process occurs at the outer region (larger impact parameter) of the nucleus.

iii) The median spin I_m of the gsb levels is much smaller than the average spin I_γ for the entry states. The large difference between the I_m and I_γ is explained by the K-band deexcitation model. The I_γ values for the $^{164}\text{Dy}(\alpha, xn \gamma)$ $^{168-x}\text{Er}$ reactions at $E_\alpha = 120$ MeV are nearly independent of the reaction channel, namely of the number x of the emitted neutrons. On the other hand the I_m values decrease a little as the number x of the emitted neutrons decreases. This may be interpreted as follows. The fast neutron emitted at the preequilibrium stage causes the spread of the width of the spin distribution at entry point. Consequently gamma ray deexcitation flow from the increased low spin part makes the reduction of the median spin I_m . The I_m values for a given reaction channel are nearly constant in a wide range of the projectile energy (see 3-11-a). The I_γ values also show the same trend.¹⁰⁶⁾ This is interpreted as follows. As the incident alpha energy goes higher, the specific reaction is going to occur at outer region of the nucleus and deexciting neutrons emitted at the preequilibrium stage take out more angular momenta. As a result the width of the spin population becomes wider, and I_γ and I_m are kept rather constant.

iv) It is interesting to obtain the number n_p of the preequilibrium decay neutrons in view of reaction mechanism. Sarantites et al. carried out calculations of cross sections and particle energy spectra with the geometry-dependent hybrid model with one preequilibrium particle emission in ref. 116), and analyzed their multiplicity data. They concluded that for reaction channels corresponding to a small number of emitted neutrons, more than one preequilibrium neutron emission occurs following the (α , xn) reactions on ^{166}Er at 95.3 MeV. We also obtained the number n_p of the preequilibrium decay neutrons in the projectile energy range of $E_\alpha = 50 \sim 120$ MeV using a simple two step model (preequilibrium-equilibrium) (see fig. 4-8). Our results are consistent with that of Sarantites results.

The number of prequilibrium decay nucleons is also obtained for the proton projectile by Sadler et al.¹²⁰⁾ They measured production of various nuclei following bombardments of median mass nuclei ($^{58-64}\text{Ni}$, $^{54,56}\text{Fe}$, ^{59}Co , ^{48}Ti) with intermediate energy protons ($E_p = 80-160$ MeV) by observing gamma-rays. By the variation of production cross-section with target mass and bombarding energy they estimated that one or two nucleons are emitted in the preequilibrium phase in every case. This results are also consistent with that of our results (see eq. 4.33).

v) The medium heavy nuclei excited by 90-120 MeV alpha particles were found to deexcite firstly down to around 50 MeV excitation energy by emitting two or three nucleons at the preequilibrium stage. After this they decay by evaporating low energy neutrons at the equilibrium stage. The nucleus excited by 60 MeV protons decays down to around 40 MeV by emitting 1~2 nucleons at the preequilibrium stage. At this point the nucleus reaches the equilibrium. Thus the critical energy $E_c \approx 50$ MeV for the phase transition between the pre-equilibrium and equilibrium processes for the alpha projectile is somewhat larger than the critical energy $E_c \approx 40$ MeV for the proton bombardment. The difference is considered to be due to the different number of excitons at the initial stage. The existence of the phase transition was firstly predicted theoretically by Yoshida in the frame work of exciton model and this is the reason why our simple two step model reproduce well the experimental results.

§6 Summary and Concluding Remarks

Preequilibrium and equilibrium deexcitation processes in the (particle, $xn\; yp\; \gamma$) reactions induced by medium energy ($E \sim 100$ MeV) projectiles were studied by measuring the detailed singles gamma ray spectra and the decaying neutrons in coincidence with the gamma rays. Projectile dependence of the K-isomer ratio was also studied. The results are summarized as follows.

- i) The cross-sections $\sigma(E_T)$ and the median spin values I_m of the gsb levels were studied on the (particle, $xn\; yp\; \gamma$) reactions at various projectile energies and particles.
- ii) The cross sections for the small number (x) of emitted neutrons with large E_T (sum of energies of the emitted neutrons) are much larger than expected from the compound process. This feature gets pronounced more as the projectile energy gets higher.
- iii) The obtained I_m values increase very slowly as E_α goes from 50 to 120 MeV. They are much smaller ($\sqrt{I_m(CN)}/2$) than the mean value ($I_m(CN) = \frac{2}{3}I_{max}$) of the angular momenta introduced by the alpha projectile. The I_m values for a given reaction channel are fairly flat in a wide range of the alpha energy. The I_m 's for the large E_T region, where the preequilibrium process is impor-

tant, are definitely smaller than that for the small E_T region.

- iv) The $n-\gamma$ coincidence method was successfully used to study the preequilibrium and equilibrium processes following the $^{164}\text{Dy}(\alpha, xn \gamma)$ reactions at $E_\alpha = 90$ and 120 MeV and the $^{165}\text{Ho}(p, xn \gamma)$ reaction at $E_p = 60$ MeV.
- v) The neutron energy spectra have a high energy ($10 \sim 16$ MeV) part and a low energy ($2 \sim 4$ MeV) part. The high energy part is particularly conspicuous in the neutron energy spectra at forward angles in the reaction with large E_T .
- vi) Neutron angular distributions following (particle, $xn \gamma$) reactions are asymmetric with respect to 90° . The asymmetry term $A_1 P_1(\cos\theta)$ is larger in the reaction with larger E_T and small x , and gets pronounced more as the projectile energy gets higher.
- vii) The exciton model was applied for the deexcitation process of the (particle, $xn \gamma$) reactions. The particle decay width at the preequilibrium stage (the escape probability), the fraction of the preequilibrium decay, and the energy and angular distributions of the decaying neutrons were calculated. On the basis of these calculation the simple analytical model with two energy parameters was made.
- viii) The cross sections were reproduced in terms of the

preequilibrium-equilibrium process. For example $\sigma(\alpha, xn)$

$$= 0.7 \sum_x \sigma(3, x-3) + 0.3 \sum_x \sigma(2, x-2) \text{ with } kT_p = 7 \text{ MeV}$$

and $kT = 2$ MeV for $E_\alpha = 120$ MeV reactions. Other reactions were also well reproduced in a similar manner.

- ix) The mean number \bar{n}_p of the preequilibrium decay neutrons in the $(\alpha, xn \gamma)$ reactions induced by 50, 70, 90 and 120 MeV alpha particles are 0.5, 0.8, 1.8 and 2.8, respectively.
- x) The asymmetric (forward peaking) angular distribution is reproduced by assuming n_p neutrons emitted isotropically in the center of mass system of the local exciton particles in the preequilibrium stage.
- xi) The critical energy for the phase transition between the preequilibrium and equilibrium stages is around $E_C \approx 50$ and 40 MeV for the alpha and proton bombardments.
- xii) The preequilibrium process is more important at the outer region (larger impact parameter) of the nucleus.
- xiii) The K-isomer ratios in ^{182}Os and $^{172,174}\text{Hf}$ were studied by (particle, $xn \gamma$) reactions for various kinds of projectiles in a wide range of the projectile energy. They were found to depend on the projectile mass.

Finally some remarks should be made on further extensions of this work. Combining the energy and angular distributions of the neutrons and the gamma ray multiplicity, the mean values $I_C \hbar = I_\gamma \hbar + \bar{\lambda} n \hbar$ for the spin population at the initial (pre)com-

pound system can be obtained. Thus we can obtain the mean impact parameter for individual (particle, $xn\gamma$) reaction channels. Systematic studies will advance understanding of the reaction mechanism.

The simple model with two temperatures reproduces well the cross sections following (particle, $xn\gamma$) reactions, though the model does not work well for reactions involving the charged particle emission. Charged particles are emitted mainly at the preequilibrium stage for the present mass region since low energy charged particles evaporated at the equilibrium stage are suppressed much by the Coulomb barrier. Thus the preequilibrium and equilibrium deexcitation processes may be selectively obtained by observing gamma rays in coincidence with charged particles. Measurements of the charged particle angular and energy distributions are useful for clarifying the mechanism. Recently a break up process of composite projectiles such as α and ^3He was extensively studied.^{113,114)} The cross-sections by this process at present energy region are about 10% of the total cross section. It is also interesting to study how much contributions are there in (particle, $xn\gamma$) reactions from the break up process.

In our simple model with two energy parameters (temperature for the equilibrium phase) the effect due to the angular momentum dependence of the level density is not taken into account in the deexcitation process. The spin dependent

temperature was defined by Williams and Thomas¹¹⁵⁾ as

$$T_I \approx T \left[1 - \frac{E_{\text{rot}}(I)}{E^*} \right]^{\frac{1}{2}}$$

where $E_{\text{rot}}(I)$ is the rotational energy, E^* is the excitation energy and T is the nuclear temperature. In the present energy region $E_{\text{rot}}(I) \ll E^*$ and $T_I \approx T$. Thus we do not need to consider the effect due to the angular momentum. In the HI induced reaction, the angular momentum is so large that the deexcitation is largely affected by the angular momentum dependence of the level density, etc. It is very interesting to investigate how the preequilibrium and equilibrium processes are affected by this high angular momentum introduced by the HI projectile.

Acknowledgement

The author would like to express his cordial thanks to Professor H.Ejiri for his valuable and stimulating discussions and warm guidance during the course of this work. The author is much indebted to Prof. S.Yoshida for valuable discussions and for making | the computer program, and to Prof. S.Yamabe for encouragement and criticism. The author is also indebted to Prof. A.Shimizu and Drs. Y.Nagai, T.Shibata, T.Itahashi, K.Okada and M.Hoshi for their excellent collaborations and valuable discussions. Many thanks are also due to Messrs. S. Nakayama, T.Kishimoto, K.Maeda, H.Suzuki, the RCNP staffs and the cyclotron crew for kind help and discussions.

References

- 1) R.Vandenbosch and J.R.Huizenga, Phys. Rev. 120 (1960) 1313
- 2) G.B.Hansen et.al., Nucl. Phys. 47 (1963) 529
- 3) H.Ejiri, et.al., Nucl. Phys. 89 (1966) 641
- 4) N.Bohr, Nature 137 (1936) 344
- 5) H.Morinaga and P.C.Gugelot, Nucl. Phys. 46 (1963) 210
- 6) B.J.Shepherd, C.F.Williamson and I.Halpern, Phys. Rev. Lett. 17 (1966) 806
- 7) C.F.Williamson, S.M.Ferguson, B.J.Shepherd and I.Halpern, Phys. Rev. 174 (1968) 1544
- 8) S.Ferguson, H.Ejiri and I.Halpern, Nucl. Phys. A188 (1972) 1
H.Ejiri and I.Halpern, Bull. Amer. Phys. Soc. 13 (1968) 700
- 9) G.Bernardini, E.T.Booth, and S.J.Lindenbaum, Phys. Rev. 85 (1952) 826
- 10) R.M.Eisberg, Phys. Rev. 94 (1954) 739
- 11) B.L.Cohen, et.al., Phys. Rev. 94 (1954) 620
- 12) S.Hayakawa, M.Kawai and K.Kikuchi, Prog. Theor. Phys. 13 (1955) 415

- 13) S.Z.Belensdy and L.D.Landau, *Nuovo Cimento, Supplement* 3 (1956) 15
- 14) K.Kikuchi and M.Kawai, *Nuclear Matter and Nuclear Interactions*, North Holland Publishing Co., Amsterdam (1968)
- 15) W.Swenson and N.Cindro, *Phys. Rev.* 123 (1961) 910
- 16) A.Chevarier, et.al., *Phys. Rev.* C8 (1973) 3155
- 17) A.Chevarier, et.al., *Nucl. Phys.* A231 (1974) 64
- 18) F.E.Bertrand, R.W.Peele and C.K.Cline, *Phys. Rev.* C10 (1974) 1028
- 19) M.T.Magda, A.Alevra and I.R.Lukas, *Proc. Conf. Highly Excited states in Nuclei*, (1975), Jülich, Germany
A.Alevra et.al., *Nucl. Phys.* A265 (1976) 376
- 20) J.Bisplinghoff, J.Ernst, R.Löhr, T.Mayer-Kuckuk and P.Meyer, *Nucl. Phys.* A269 (1976) 147
- 21) F.E.Bertrand and R.W.Peele, *Phys. Rev.* C8 (1973) 1045
- 22) G.Chenevert, *Thesis*, Univ. Washington, G.Chenevert, I.Halpern, and D.L.Hendrie (unpublished) (1970)
- 23) R.R.Dering et.al., *Nucl. Phys.*, (1975)
- 24) C.Birattari et. al., *Nucl. Phys.* A201 (1973) 579
- 25) P.Jahn, H.J.Probst, A.Djaloeis, W.E.Davidson and C.Mayer-Böricke, *Nucl. Phys.* A209 (1973) 333
- 26) R.Serber, *Phys. Rev.* 72 (1947) 1114
- 27) H.W.Bertini, *Phys. Rev.* 131 (1963) 1801
- 28) H.W.Bertini, G.D.Harp and F.E.Bertrand, *Phys. Rev.* C10 (1974) 2472

29) J.J.Griffin, Phys. Rev. Lett. 17 (1966) 478

30) G.D.Harp, J.M.Miller and B.J.Berne, Phys. Rev. 165 (1968) 1166; G.D.Harp and J.M.Miller, Phys. Rev. C3 (1971) 1847

31) C.K.Cline and M.Blann, Nucl. Phys. A172 (1971) 225

32) M.Blann, Phys. Rev. Lett. 27 (1971) 337

33) M.Blann, Lecture Notes in Physics, vol. 22, ed. by N. Cindro et.al., (Springer Verlag, Berlin, 1973) p.43

34) E.Gadioli, E.Gadioli-Erba, and P.G.Sona, Nucl. Phys. A217 (1973) 589

35) C.Birattari, et.al., Nucl. Phys. A201 (1973) 579

36) M.Blann, Phys. Rev. Lett. 28 (1972) 757, Nucl. Phys. A213 (1973) 570

37) G.Mantzouranis, D.Agassi and H.A.Weidenmüller and D.A.Agassi, Z.Physik A276 (1976) 145, G.Mantzouranis, Phys. Lett. 63B (1976) 25

38) S.Yoshida, Proc. Int. Symp. Hakone HI and Preeq. Reactions 1977

39) B.Blann, Phys. Rev. Lett. 21 (1968) 1357

40) J.Ernst and Jayanti Rama Rao, Z. für Physik A281 (1977) 129

41) M.Blann, Ann. Rev. Sci., 25 (1975); Nukleonika 21 (1975) 335

42) E.Gadioli and E.Gadioli Erba, Nucl. Instr. Method 146 (1977) 265

43) H.Ejiri, G.B.Hagemann and T.Hammer, Proc. Int. Conf. on Statistical Properties of Nuclei, Albany, 1971, p.483

44) J.O.Newton, F.S.Stephens, R.M.Diamond, W.H.Kelly, and
D.Ward, Nucl. Phys. A141 (1970) 631

45) M.Ishihara, et.al., Nucl. Phys. A179 (1972) 769

46) H.Ejiri et.al., Proc. Int. Conf. Nucl. Structure, Tokyo,
1977 J. Phys. Soc. Japan 44 (1978) Suppl. 655

47) H.Ejiri et.al., to be published on Nucl. Phys.

48) H.Sakai, H.Ejiri, T.Kishimoto and S.Yoshida, Proc. Int.
Symp. HI and Preeq. Reactions, Hakone (1977)

49) RCNP Annual Report 1976

50) M.Kondo et al. Proc. 7th Int. Conf. Cycl. 1975

51) R.A.Wingard, J.E.Lutkin and G.W.McBeth, Nucl. Instr. and
Meth. 95 (1971) 141

52) R.A.Winyard and G.W.McBeth, Nucl. Instr. and Meth. 98
(1972) 525

53) V.V.Verbinski et al., Nucl. Instr. and Meth. 65 (1968) 8

54) R.Batchelor, W.B.Gilboy, J.B.Parker and J.H.Towle,
Nucl. Instr. and Meth. 13 (1961) 70

55) V.V.Verbinski, J.C.Courtney and N.Betz, Nucl. instr. and
Meth. 52 (1967) 181

56) W.R.Burrus and V.V.Verbinski, Nucl. Instr. and Meth.
67 (1969) 181

57) P.Sperr, H.Spieler, M.R.Maier and D.Evers, Nucl. Instr.
and Meth. 116 (1974) 55

58) S.A.Hjorth, H.Ryde, K.A.Hagemann, G.Løvhøiden, and
J.C.Wakkington, Nucl. Phys. A144 (1970) 513

59) R.Broda et al. A248 (1975) 356

60) J.K.Tuli, Nuclear Data Sheets, 9 (1973) 435, 12 (1974) 477; 13 (1974) 493

61) J.H.Jett and P.A.Lind, Nucl. Phys. A155 (1970) 182

62) S.Ferguson, H.Ejiri and I.Halpern, Nucl. Phys. A188 (1972) 1

63) A.Johnson, H.Ryde, and S.A.Hjorth, Nucl. Phys. A109 (1972) 753

64) H.Ryde et al., Nucl. Phys. A207 (1973) 513

65) R.M.Lieder et al., Z.Physik 257 (1972) 147

66) E.Grosse, F.S.Stephens and R.M.Diamond, Phys. Rev. Lett. 31 (1973) 840

67) R.Janssens et al., Nucl. Phys. A283 (1977) 493

68) J.R.leigh, F.S.Stephens and R.M.Diamond, Phys. Lett. 33B (1970) 410

69) E.Grosse, F.A.Stephens and R.M.Diamond, Phys. Rev. Lett. 32 (1974) 74

70) L.Funke et al., Nucl. Phys. A170 (1971) 593

71) L.Funke et al., Nucl. Phys. A190 (1972) 576

72) K.G.Rensfelt, A.Johnson and S.A.Hjorth, Nucl. Phys. A156 (1970) 529

73) J.Rezanda, H.Ryde and S.Huitberg, Physica Scripta 8 (1973) 239

74) G.D.Dracoulis, S.M.Ferguson, J.O.Newton and M.G.Slocombe, Nucl. Phys. A279 (1977) 251

75) H.Ejiri and G.B.Hagemann, Nucl. Phys. A161 (1971) 449

76) T.L.Khoo, J.C.Waddington, Z.Preibisz and M.W.Johns, Nucl. Phys. A202 (1973) 289

77) I.Rezanka, J.O.Rasmussen, F.M.Bernthal, C.T.Alonso, J.R.Abnso, S.Hultberg and H.Ryde, Nucl. Phys. A197 (1972) 430

78) S.Hultberg. I.Rezanka and H.Ryde, Nucl. Phys. A205 (1973) 321

79) A.Andre, D.Barneoud, C.Foin, B.Ader and N.Perrin, Nucl. Phys. A279 (1977) 347

80) J.O.Newton, F.S.Stephens and R.M.Diamond, Nucl. Phys. A210 (1973) 19

81) B.Skaali, R.Kalish, J.Eriksen and B.Herskind, Nucl. Phys. A238 (1975) 159

82) B.Bochev, etal., Nucl. Phys. A282 (1977) 159

83) I.Rezanka, I.M.Ladenbauer-Bellis, J.O.Rasmussen, W.Ribbe and E.der Mateosian, Phys. Rev. C11 (1975) 1767

84) H.Ejiri, Private Communication

85) P.M.Walker, G.D.Dracoulis, A.Johnston and J.R.Leigh, Private Communication

86) I.Rezanka et al., Nucl. Phys. A197 (1972) 430

87) S.Hultberg. I.Rezanka and H.Ryde, Nucl. Phys. A205 (1973) 321

88) C.Foin et al., Nucl. Phys. A199 (1973) 129

89) P.Kemnitz et al., Nucl. Phys. A209 (1973) 271

90) C.Foin, S.Andre and S.A.Hjorth, Nucl. Phys. A219 (1974)
347

91) S.A.Hjorth, H.Ryde and B.Skanberg, J.Phys. (PARIS) 33
(1972) 23

92) D.BarneouD et al., J.Phys. (PARIS) 33 (1972) 15

93) A.D.Veselkin, Y.A.Egorov and M.E.Netecha, Engineering
Compendium on Radiation Shielding p.270 Springer-Verlay
Berlin 1968

94) J.O.Newton, Nucl. Phys. A108 (1968) 353

95) E.A.Straker et al., Nucl. Instr. and Meth. 97 (1971) 275

96) T.Ericson and V.Strutinski, Nucl. Phys. 8 (1958) 284
and 9 (1958/59) 689

97) D.Agassi, H.A.Weidenmüller and G.Mantzouranis, Phys. Rep.
C22 (1975) 145
D.Agassi and H.A.Weidenmüller, Phys. Lett. 56B (1975)
305

98) S.Yoshida, Ann. Rev. Nucl. Sci. 24 (1974) 1
K.Yazaki and S.Yoshida, Nucl. Phys. A232 (1974) 249,
A255 (1975) 173

99) E.Gadioli et al., Phys. Lett. 65B (1976) 311

100) M.Blann, Phys. Lett. 67B (1977) 145

101) J.Ginocchio and M.Blann, Phys. Lett. 68B (1977) 405

102) S.Z.Belensky and L.D.Landau, Nuovo Cimento, Supplement
3 (1956) 15
G.D.Westfall et al., Phys. Rev. Lett. 37 (1976) 1202

103) A.Bohr and B.Mottelson, Nuclear Structure, Benjamin, 1969, New York, Amsterdam

104) P.O.Tjom, et al., Phys. Rev. Lett. 33 (1974) 593; G.B.Hagemann, et al., Nucl. Phys. A245 (1975) 166

105) E.Der Mateosian, O.C.Kistner and A.W.Sunyar, Res. Rev. Lett. 33 (1974) 596, J.O.Newton, et al., Phys. Rev. Lett. 34 (1975) 99

106) M.Ogawa et al., Z .Physik A284 (1978) 271

107) J.O.Newton, et al., Phys. Rev. Lett. 38 (1977) 810

108) K.A.Geoffroy and J.Natowitz, Phys. Rev. Lett. 37 (1976) 1198

109) W.F.Davidson,et al., Z.Physik, 264 (1973) 235

110) D.W.Lang and K.J.Le Couteur, Nucl. Phys. 14 (1959) 21

111) Y.Nagai et al. to be published

112) R.J.Liotta and R.A.Sorensen, Nucl. Phys. A297 (1978) 136

113) N.Matsuoka, private communication.

114) J.R.Wu, C.C.Chang, and H.D.Holmgren, Phys. Rev. Lett. 40 (1978) 1013

115) D.C.Williams and T.D.Thomas, Nucl. Phys. A92 (1967) 1

116) D.G.Sarantites et al., Phys. Rev. C17(1978)601

117) H.W.Broek, Phys. Rev. 124(1961)233

118) W.G.Simon and S.T.Ahrens, Phys.Rev. C2(1970)1292

119) C.R.Gould et al., Z.Physik A284,(1978)353

120) M.Sadler et al., Phys. Rev. Lett. 38(1977)950

Figure Captions

- 1-1. Schematic deexcitation process of a nucleus following (particle, xn yp γ) reactions.
- 1-2. Schematic representation of the equilibration process in the exciton model.
- 1-3. Schematic energy levels and deexcitation process for the 120 MeV (α , xn γ) reaction (upper), and the total energy E_T of the emitted neutrons (see text) and the average kinetic energy $\bar{E}_n = E_T/x$ per neutron as a function of the number (x) of the emitted particles (right hand side).
- 2-1. The F beam transport system.
- 2-2. Circuit diagram to pick up the cyclotron R-F signal.
- 2-3. Typical counter arrangement
- 2-4-a Absolute efficiency curve for the ORTEC-II 55cc Ge(Li) detector.
- 2-4-b Absolute efficiency curve for the LEPS detector.
- 2-5. Neutron energy vs. electron energy for NE213 liquid scintillator (taken from ref.(53))
- 2-6. Schematic representation of pulse height distribution for monoenergetic neutrons E_n . B is the lower discrimination level and ΔE is the width of the i-th neutron energy window.
- 2-7. Efficiency of an organic scintillator for 0.04 Cobalt lower threshold (taken from ref.(55)). The open circle results from a Monte Carlo calculation.

2-8 Pulse height distributions for monoenergetic neutrons of two different energies. The solid line results from V.V.Verbinski.⁵³⁾ The dashed line corresponds to a Monte Carlo calculation.

2-9 Block diagram of electronics used in the $n-\gamma$ coincidence measurements.

2-10 Neutron-gamma ray pulse shape discrimination property for four different energies following $^{164}\text{Dy} + 120 \text{ MeV-}\alpha$ reactions.

2-11 Neutron-TOF spectra following $^{164}\text{Dy} + 110 \text{ MeV-}\alpha$. The dot and cross are neutron spectra without lead shield and with 2cm lead shield, respectively (upper). The attenuation factor due to the 2cm lead absorber (lower).

3-1 Energy spectrum of gamma ray observed at $\theta_\ell = 125^\circ$. Gamma ray energies are given in units of keV.

3-2 Energy spectrum of gamma ray observed at $\theta_\ell = 40^\circ$. Gamma ray energies are given in units of keV. The A_i , B_i , C_i , D_i and E_i stand for the rotational gamma rays following the $(p, 6n)$, $(p, 5n)$, $(p, 4n)$, $(p, 3n)$ and $(p, 2n)$ reactions, respectively. The attached numbers $i = 1, 2, 3, \dots$ indicate, respectively, the transitions $2^+ \rightarrow 0^+$, $4^+ \rightarrow 2^+$, $6^+ \rightarrow 4^+$, and so on. The P, Q, R, S , stand for the gamma rays following $(p, p5n)$, $(p, p4n)$, $(p, p3n)$ and $(p, p2n)$ reactions, respectively.

3-3 Relative cross-sections for the $^{174},^{176}\text{Yb}$ (α , xn γ) $^{178},^{180}\text{-X}\text{Hf}$ reactions as a function of the total energy E_T (energy excess above the reaction threshold) of the emitted neutrons induced by 50, 70, 90 and 120 MeV alpha particles. The solid lines are the present calculations for the preequilibrium and equilibrium processes. (see text)

3-4-a Absolute cross-sections following $^{164}\text{Dy}+120$ MeV α reaction as a function of the total energy E_T . The solid line is the present calculation for the preequilibrium and equilibrium processes with $kT_p = 7$ MeV and $kT_e = 2$ MeV. The notation EQ results from the equilibrium process only with the effective temperature $kT_e = 2$ MeV. Other dotted lines are drawn to guide the eye.

3-4-b Absolute cross sections following $^{174},^{176}\text{Yb}+120$ MeV α reaction as a function of the total energy E_T . The solid line is the present calculation for the preequilibrium and equilibrium processes with $kT_p = 7$ MeV and $kT_e = 2$ MeV. The notation EQ results from the equilibrium process only with effective temperature $kT_e = 2$ MeV. Other dotted lines are introduced to guide the eye.

3-5 Absolute cross-sections following $^{165}\text{Ho}+120$ MeV reaction as a function of the total energy E_T . The dashed line results from the equilibrium process only with effective temperature $kT_e = 2$ MeV.

3-6-a Absolute cross-sections following $^{165}\text{Ho}+60\text{MeV-p}$ and $^{175}\text{Lu}+40\text{MeV p}$ reactions as a function of the total energy E_T of the emitted neutrons. The results by $E_p = 39$ and 51 MeV

are taken from ref. 67. The solid lines are introduced just to guide the eye.

3-6-b Absolute cross sections for the $^{165}\text{Ho}(p, xn \gamma)^{166-x}\text{Er}$ reactions as a function of the total energy E_T of the emitted neutrons. The solid (PE) line is the present calculation for the preequilibrium and equilibrium process. The dotted (E) and dott-dash lines are evaluated for the equilibrium process only with the effective temperature $kT_e = 1.7 \text{ MeV}$ and 2.2 MeV , respectively.

3-7 Relative cross sections induced by He particles as a function of E_T . The solid lines for ^3He -80 MeV reactions results from the present calculation (see text). Other lines are introduced just to guide the eye.

3-8 The "E_M" (the energy at which cross-section is maximum) and "S" (the slope of cross-sections at large E_T region) are plotted as a function of projectile energy (see text).

3-9 The slope S as a function of E_M for p, ^3He and α projectiles.

3-10 The observed gamma ray yield Y(I), normalized as Y(4)=1, of the gsb's following the $^{174}\text{Yb}(\alpha, 6n)^{172}\text{Hf}$ reactions at three different bombarding energies.

3-11-a The median spin values I_m as a function of alpha particle energy. The solid line denoted by I_m(CN) is expected for a compound nucleus. Other solid lines are introduced just to guide the eye.

3-11-b The median spin values I_m as a function of alpha particle energy. The dashed line denoted by \bar{L} is expected for a compound nucleus.

3-12 The I_m values as a function of E_T induced by 70, 90 and 120 MeV alpha particles on $^{174},^{176}\text{Yb}$.

3-13 A typical example of the gamma ray spectrum following the $^{182}\text{W}(\text{He}^3, 3n)^{182}\text{Os}$ reaction at $E(\text{He}^3) = 31$ MeV
A: ^{183}Re , B: ^{184}Os .

3-14-a Isomer ratios following $(p, xn \gamma)$, $(\text{He}^3, xn \gamma)$ and
3-14-b $(\alpha, xn \gamma)$ reactions as a function of I_m . (Other lab. data included). The solid lines are just to guide eyes.

3-15 Gamma-ray spectra in coincidence with the neutrons. The bin number gives the eight energy windows of the coincident neutron pulse (see text).

3-16 The relative gamma ray yield of individual $(\alpha, 10n)$, $(\alpha, 8n)$ and $(\alpha, 6n)$ reaction channels as a function of the eight neutron energy windows.

3-17 The unfolded spectra from same raw data by two different methods, differential method and response matrix method (see text).

3-18-a Neutron energy spectra $d^2\sigma_n(\alpha, xn)/d\Omega/dE_n/x$ for the $^{164}\text{Dy}(\alpha, xn)^{168-x}\text{Er}$ reactions, where x is the neutron multiplicity. Solid lines are just to guide the eyes. The arrow indicates the mean neutron energy $\bar{E}_n = E_T/x$. The observed values $d^2\sigma_n(\alpha, xn)/d\Omega/dE_n$ are factor 6 and 10 larger for the $(\alpha, 6n)$ and $(\alpha, 10n)$ reactions, respectively, because of their multiplicities.

3-18-b Neutron energy spectra $d^2\sigma_n(p, xn)/d\Omega/dE_n/x$ for the $^{165}\text{Ho}(p, xn)^{166-x}\text{Er}$ reactions. The A,B,C and D stand for the spectra at $\theta_\ell = 35^\circ, 62.5^\circ, 90^\circ$ and 145° , respectively. Solid lines are just to guide the eyes.

3-19-a Angular distributions of neutrons following (α, xn) reactions with $x = 6-11$ on ^{164}Dy . Closed circles are the data points for all neutrons above 2.5 MeV. Solid lines are the results from least square fittings.

3-19-b Angular distribution of neutrons following $(p, 4n)$ and $(p, 6n)$ reactions on ^{165}Ho . Closed circles are the data points for all neutrons above 1.1 MeV. Solid lines are the present calculations.

3-20-a The A_1 and A_2 terms of neutrons following $^{164}\text{Dy} + 120 \text{ MeV}\alpha$ reaction as a function of E_T . Solid lines are present calculations (see text).

3-20-b The A_1 and A_2 terms of neutrons following $^{164}\text{Dy} + 90 \text{ MeV}\alpha$ reactions as a function of E_T . Solid lines are present calculations (see text).

4-1 The fractions of the preequilibrium emission for various incident energies and initial exciton numbers for alpha projectile (upper) and proton projectile (lower).

4-2 The escape probability results for three initial states as a function of an exciton number. (see text).

4-3 Neutron energy spectra for three initial conditions.
(see text)

4-4 Angular distributions of emitted neutrons for three initial conditions.

4-5 Schematic picture of the preequilibrium and equilibrium deexcitation processes.

4-6 Schematic picture of the deexcitation process for the $^{165}\text{Ho}(p, xn \gamma)$ Er reaction. The $f_i(E_i)$ is the energy spectrum of all i -th neutrons ($i = 1, 2, \dots, x$), the $S_i(E_i, E_T)$ is the energy spectrum of such i -th neutron that gives the total energy $E_T = E_i$. The $E_x(E_T)$ is the sum spectrum for $E_T = \sum_i^x E_i$. The (p, xn) reaction channel is defined by such reaction as $\alpha_1 < E_T < \alpha_2$, where $\alpha_2 = E_p + Q(x)$, $\alpha_1 = E_p + Q(x+1)$. The $Q(x)$ is the Q value for the (p, xn) reaction.

4-7 The E_M and S being defined by an expression $\sigma(E_T) = \sigma(E_M) \exp[-(\frac{E_T - E_M}{S})]$ at large E_T region, for the valious energy parameters (temperatures) and the number of decaying neutrons at the preequilibrium stage.

4-8 The mean number \bar{n}_p as a function of alpha projectile energy (upper left side). The number n_p of the neutrons emitted in the preequilibrium stage and the ratio n_p/x for the $(p, xn \gamma)$ reactions as a function of E_T . These values are calculated on the basis of eqs. (13) ~ (15).
(see text).

4-9 The neutron energy spectra $d\sigma_n/dE/6$ and $d\sigma_n/dE/8$ for the $(\alpha, 6n \gamma)$ and $(\alpha, 8n \gamma)$ reactions and the present calculations (the solid lines) with $kT_e = 2$ MeV and $kT_p = 7$ MeV.

4-10 The neutron energy spectra $d\sigma_n/dE/4 = \int d^2\sigma_n/(4 \cdot dE \cdot d\Omega) d\Omega$ for the $(p, 4n \gamma)$ reactions and the present calculations (the solid lines). The dotted lines are for the pre-equilibrium process only. The A and B are the calculations with $kT_e = 1.7$ MeV, $kT_p = 7$ MeV, and $kT_e = 2.0$ MeV, $kT_p = 7$ MeV, respectively.

4-11 The A_{1x} where A_1 is the experimentally obtained anisotropy and x is the reaction channel as a function of E_T (see text).

Table 1

Target	Target Isotopic Enrichment (%)	Projectile	Projectile Energy Elab (MeV)	Comment
^{162}Dy	95	α	50, 70, 90, 110, 120	A
^{164}Dy	98.4	α	50, 70, 90, 110, 120	A
^{165}Ho	100	P, ^3He	60, 65	A
^{174}Yb	95.8	α	70, 90, 120	A
^{176}Yb	96.4	α , ^3He	50, 70, 90, 120	A
^{175}Lu	97.4	P, ^3He	40 80	A A
^{182}W	94.3	^3He	27, 32	B,C
^{184}W	94.3	α	90	A
^{185}Re	96.3	P	40	A

A: The 230 cm RCNP cyclotron at the Osaka Univ.

B: 110 cm variable energy cyclotron at the Dept. Physics.

C: IPGR cyclotron

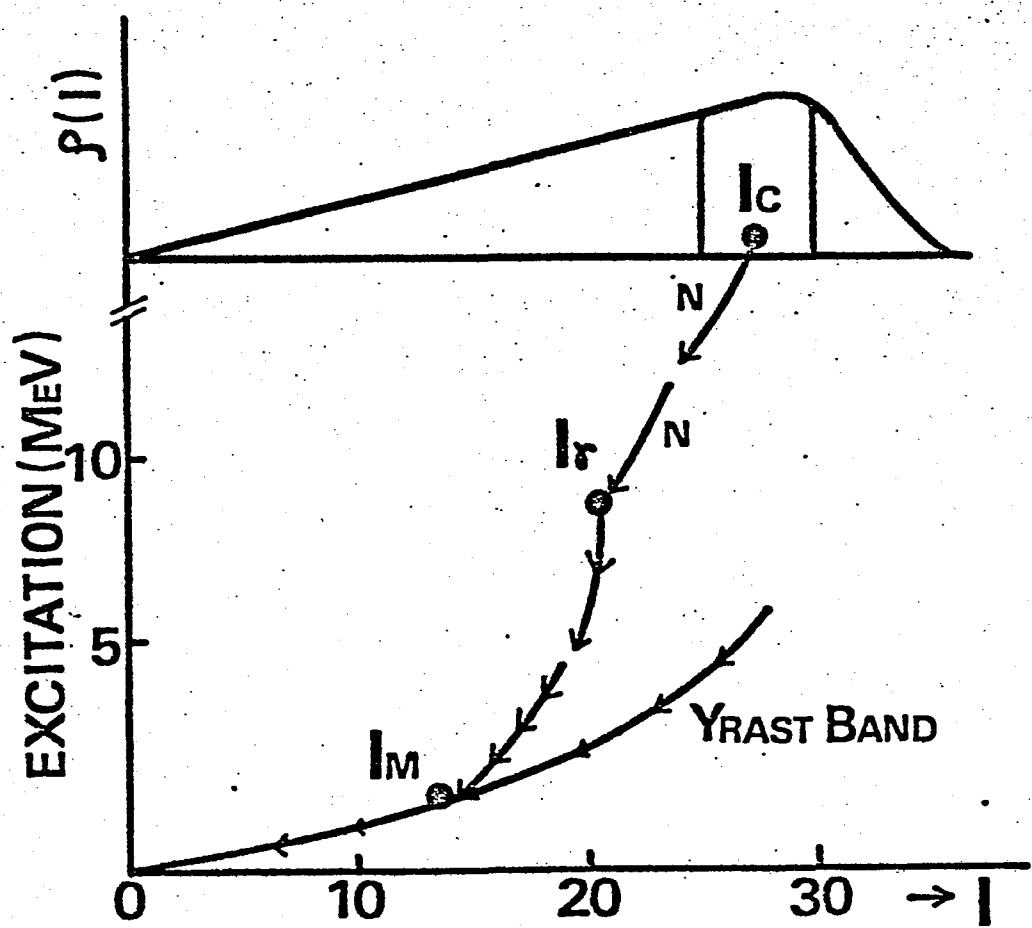


Fig.1-1

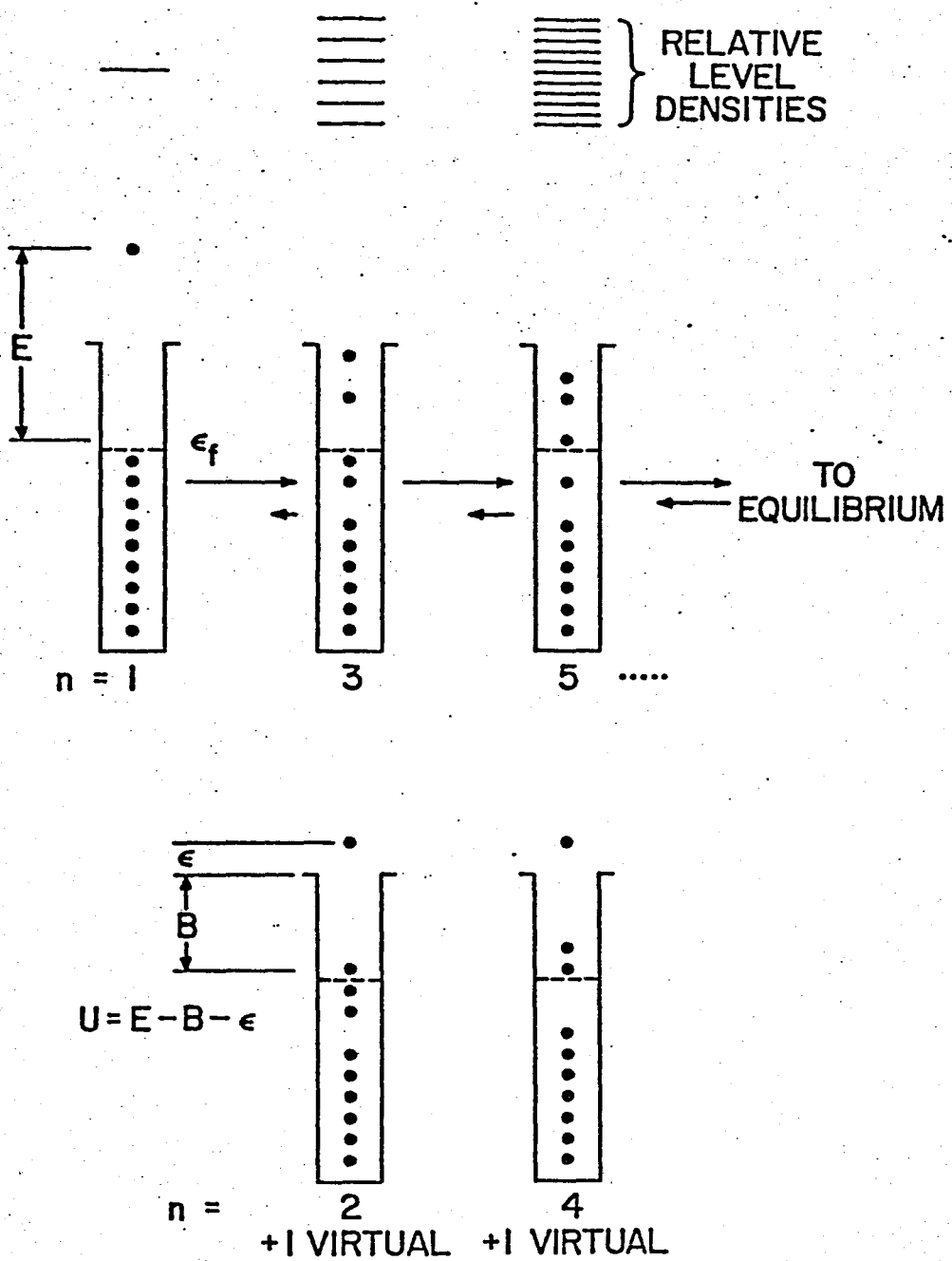
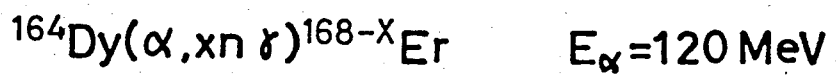
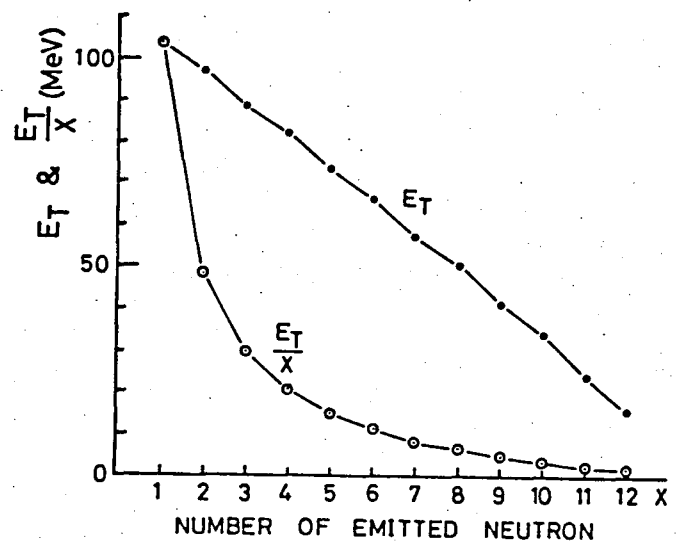
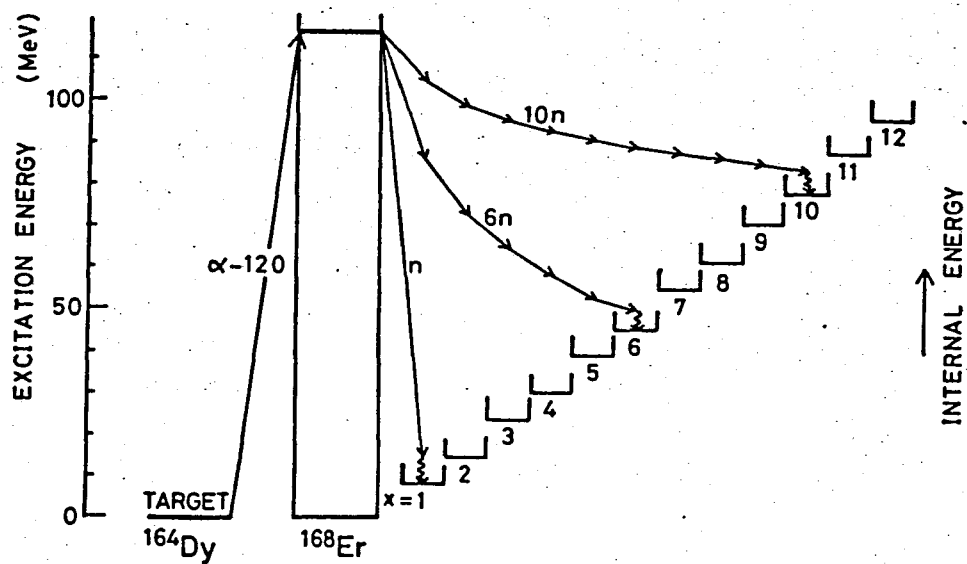


Fig.1-2

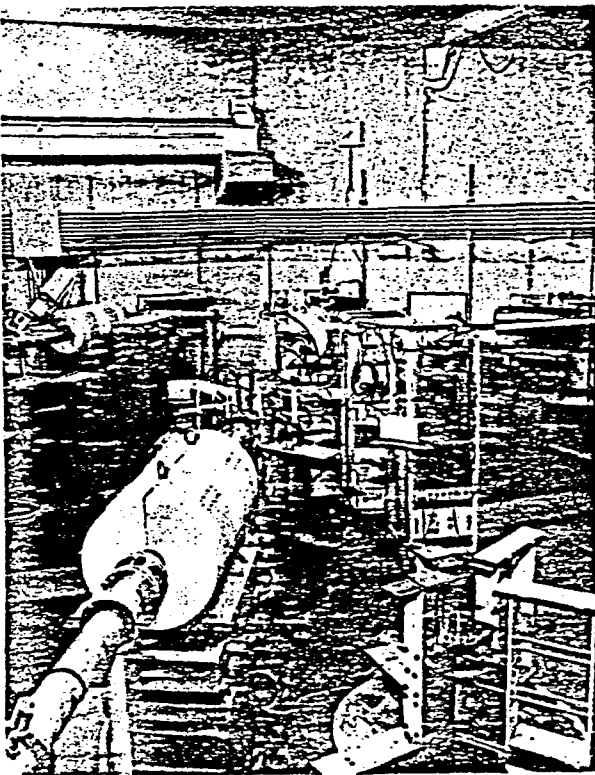
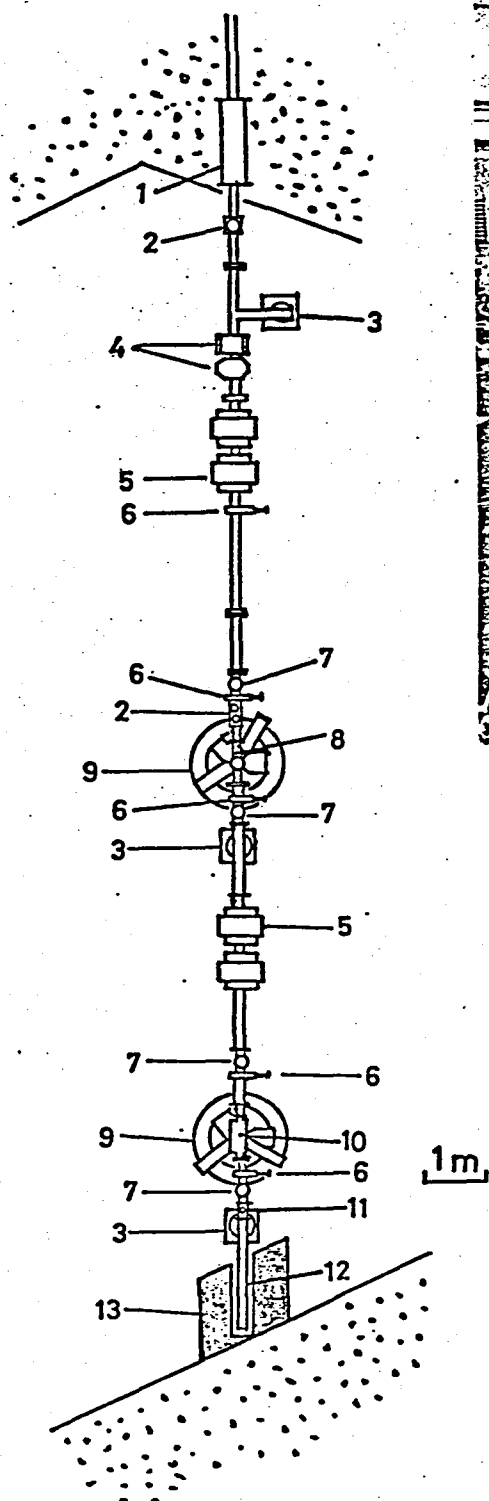


DIRECT ← PREEQ → COMPOUND



$$E_T = E_\alpha + Q(xn) - 5 \text{ MeV}$$

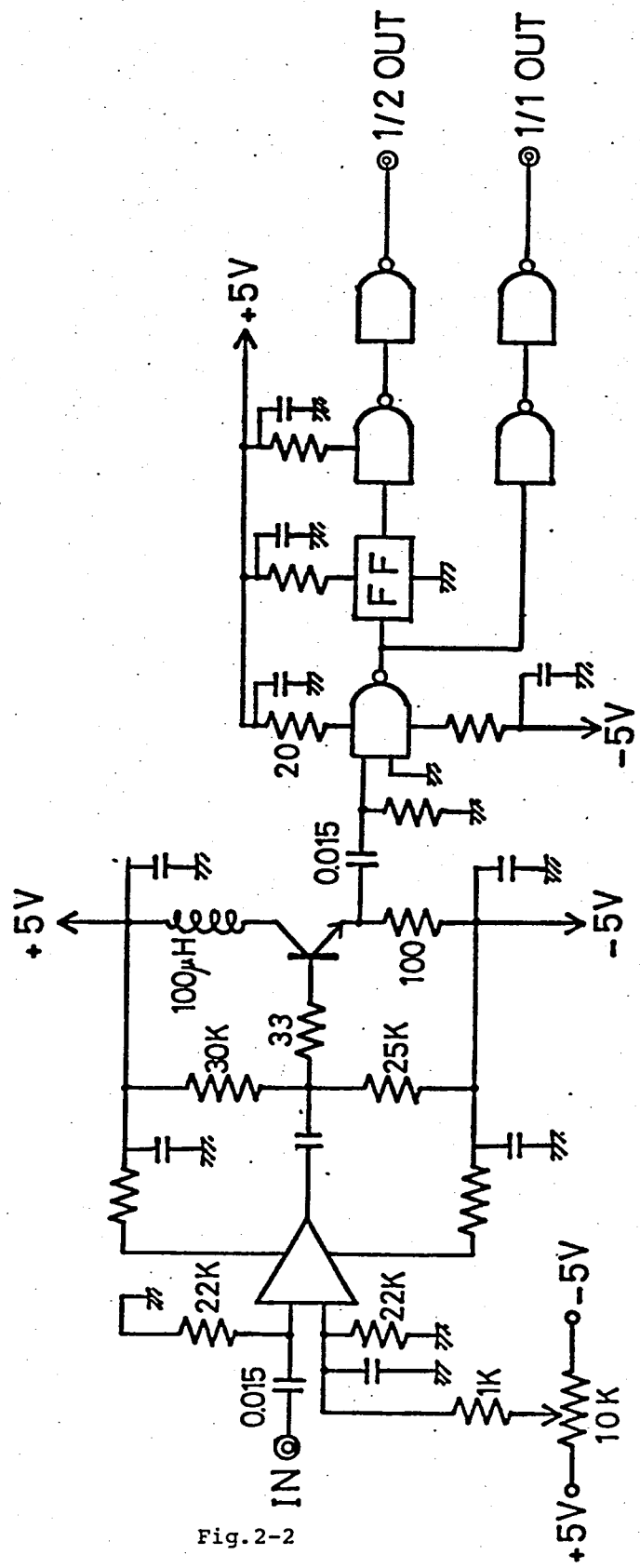
Fig. 1-3



- 1 rotary shutter
- 2 beam viewer
- 3 terbo-molecular pump(250 l/s)
- 4 steaming magnets
- 5 magnetic Q doublet
- 6 gate valve
- 7 liq. N₂ trap
- 8 target chamber for γ -ray
- 9 goniometer
- 10 target chamber for particle- γ
- 11 beam signal pickup (plastic film)
- 12 Faraday cup
- 13 beam dumper shield (iron,Pb, and paraffin blocks)

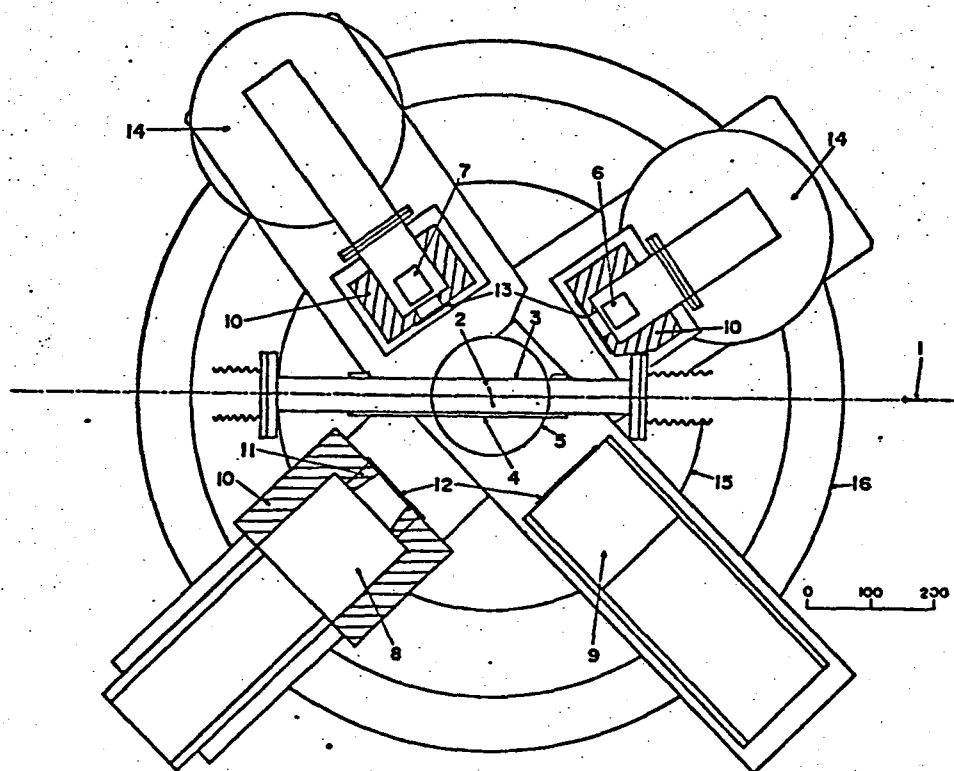
Fig.2-1

RF PICKUP CIRCUIT



733

2SC387AG 75107 7470 7400



Goniometer and an example of counter arrangement used for the photon and particle spectroscopy. 1: Incident beam. 2: Target. 3: Thin mylar (Al) window. 4: Lucite window. 5: Remote control devices for adjusting the target position. 6: Ge(Li) detector. 7: Monitor counter [Ge(Li)]. 8: NaI(Tl) detector for unresolved gamma rays. 9: Liquid scintillator (Ne 213). 10: Lead shield. 11: Lead collimator. 12: Cu or brass absorber for low energy gamma rays and X rays. 13: Cu absorber for low energy gamma rays and X rays. 14: Liquid nitrogen vessel. The scale in units of mm is shown in the right hand side.

Fig.2-3

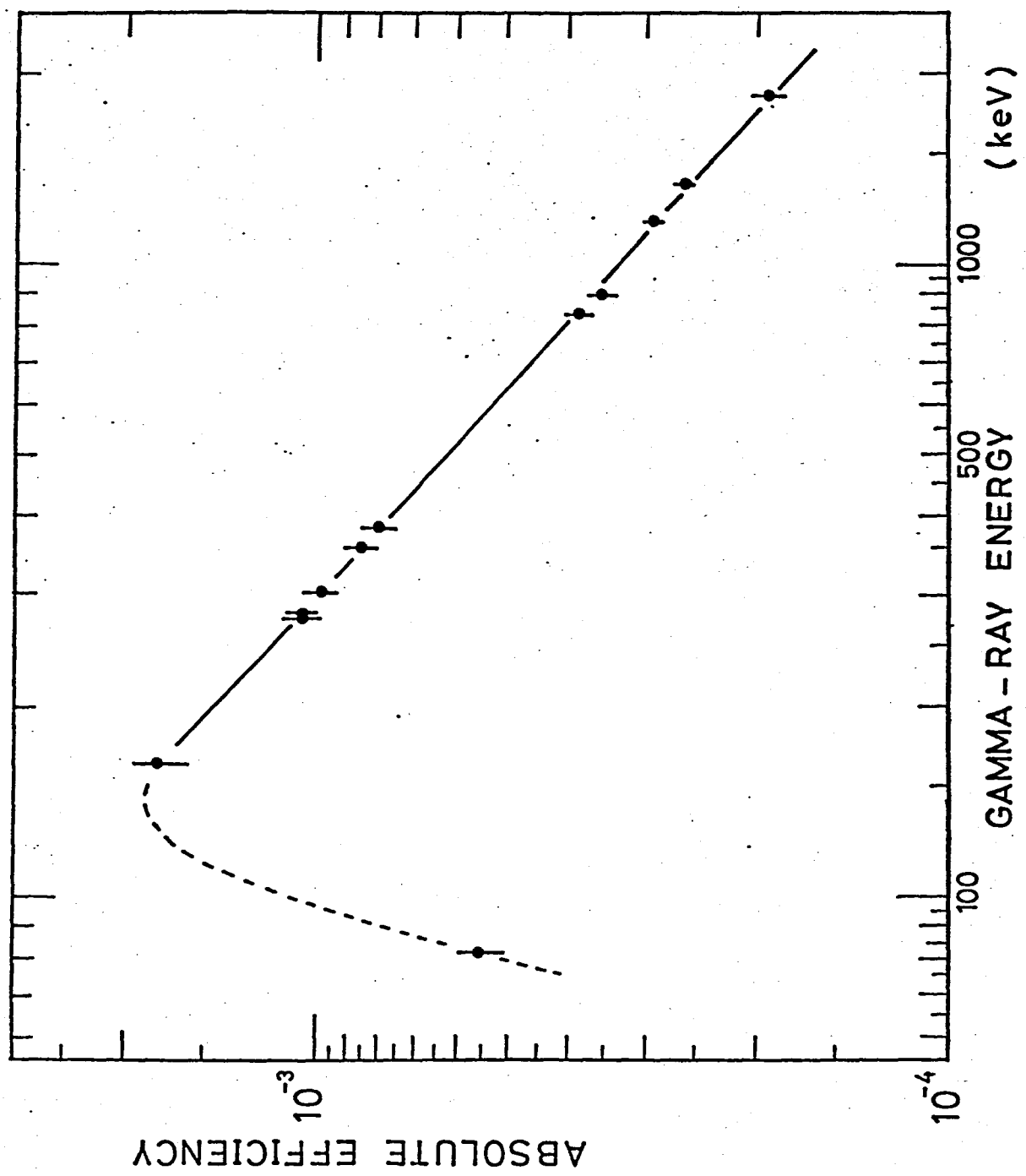


Fig.2-4-a

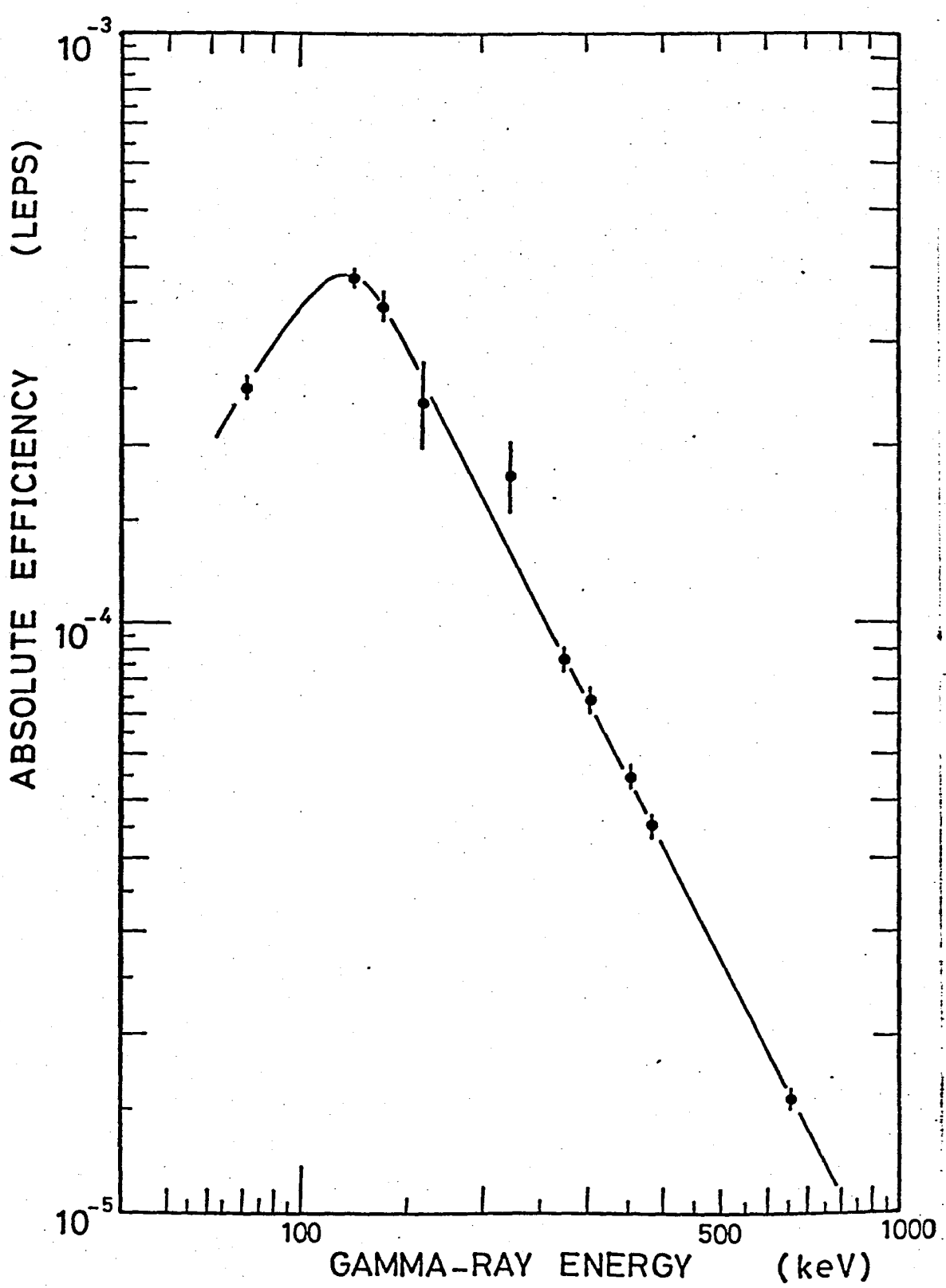


Fig. 2-4-b

Neutron Energy vs. Electron Energy for NE213 Liquid Scintillator

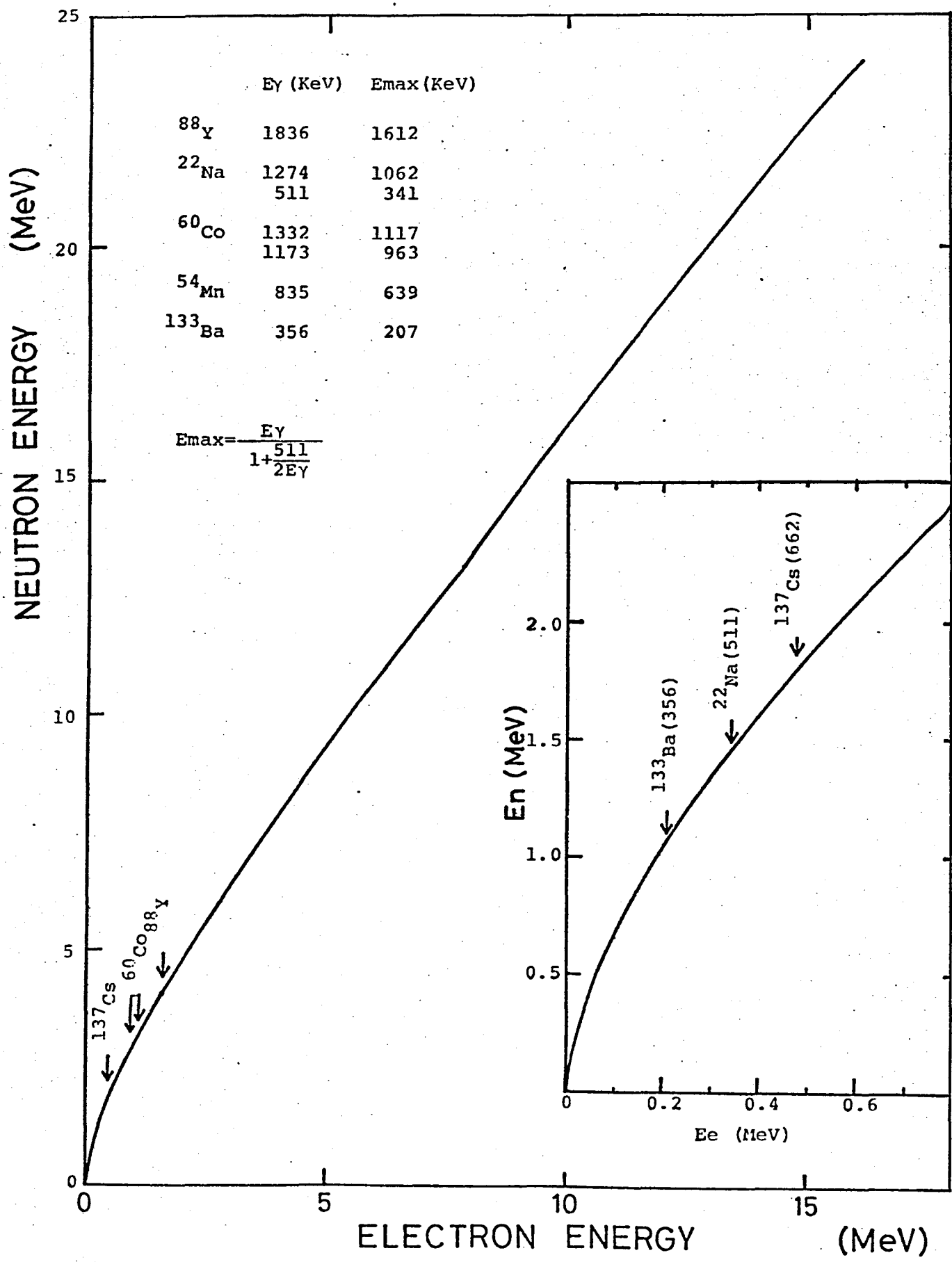


Fig. 2-5

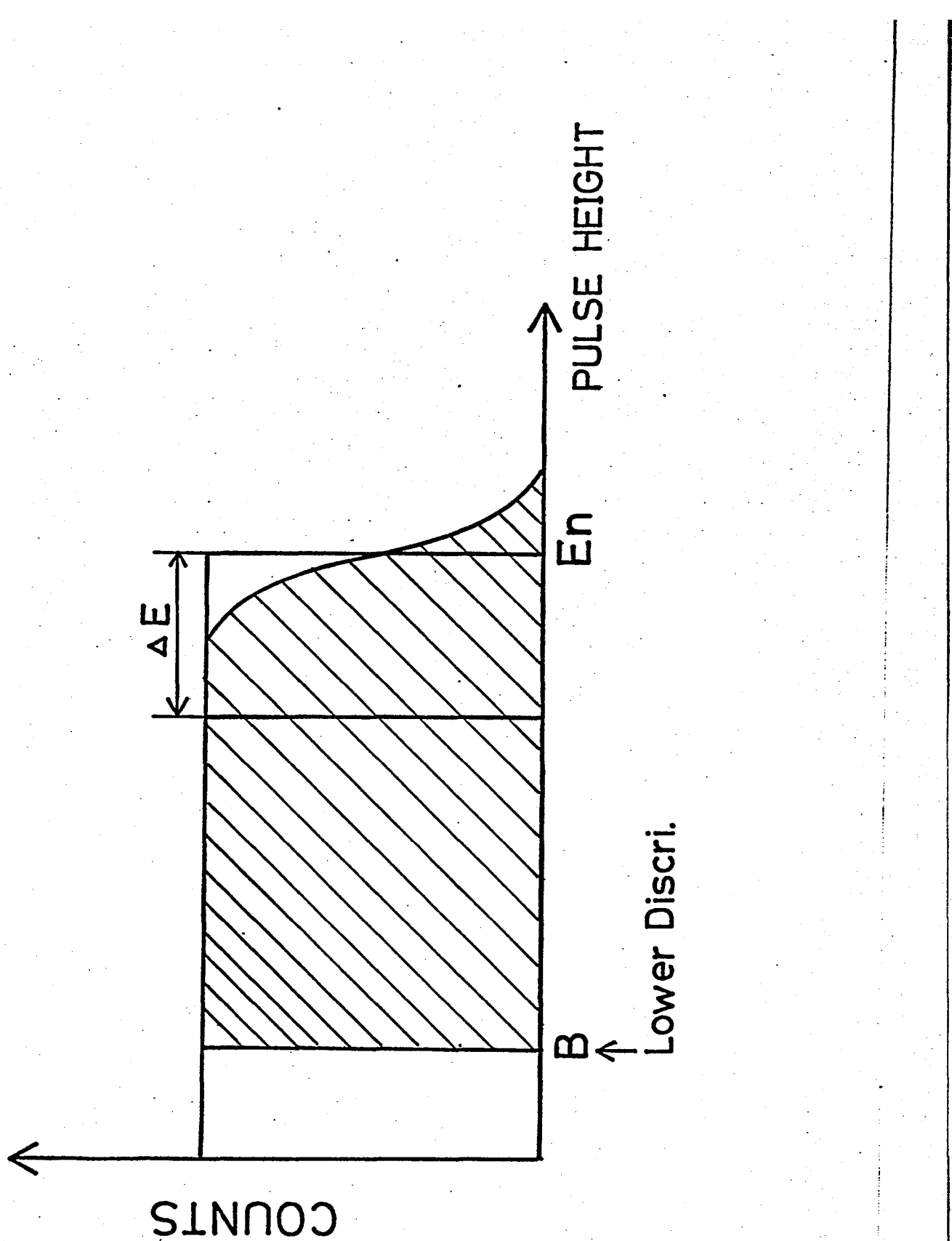


Fig. 2-6

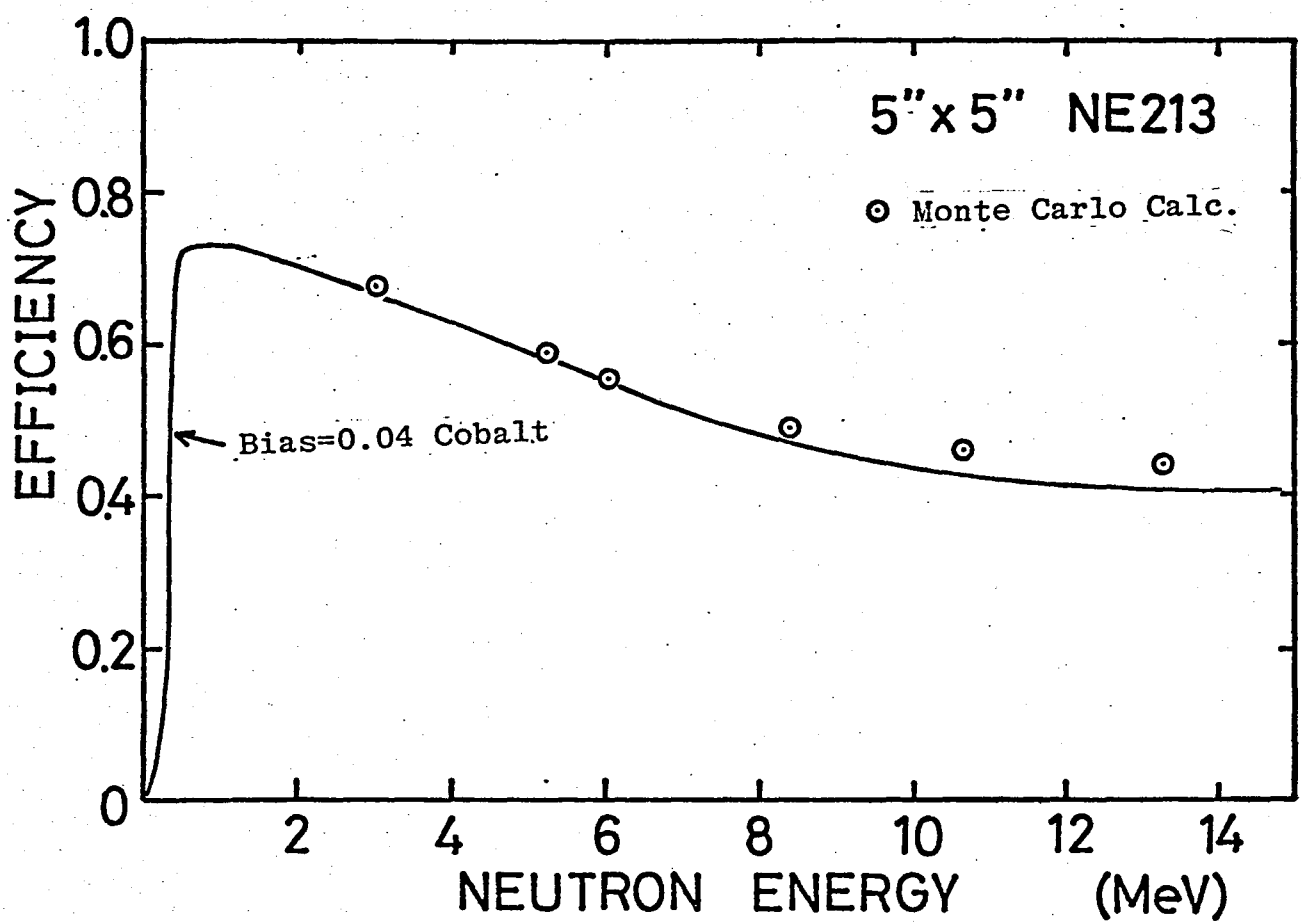


Fig. 2-7

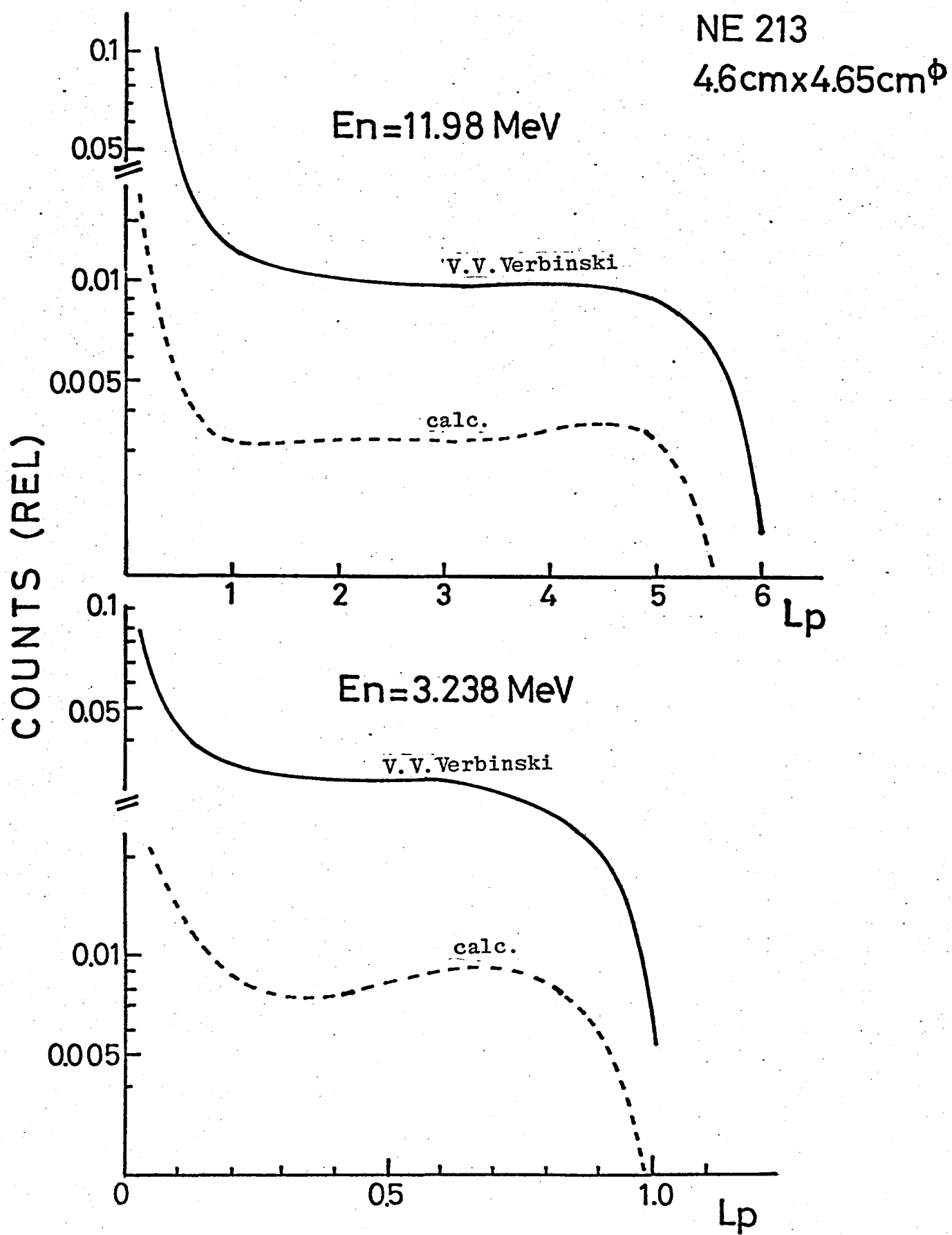


Fig. 2-8

BLOCK DIAGRAM of ELECTRONICS for $n-r$ COINCIDENCE MEASUREMENTS

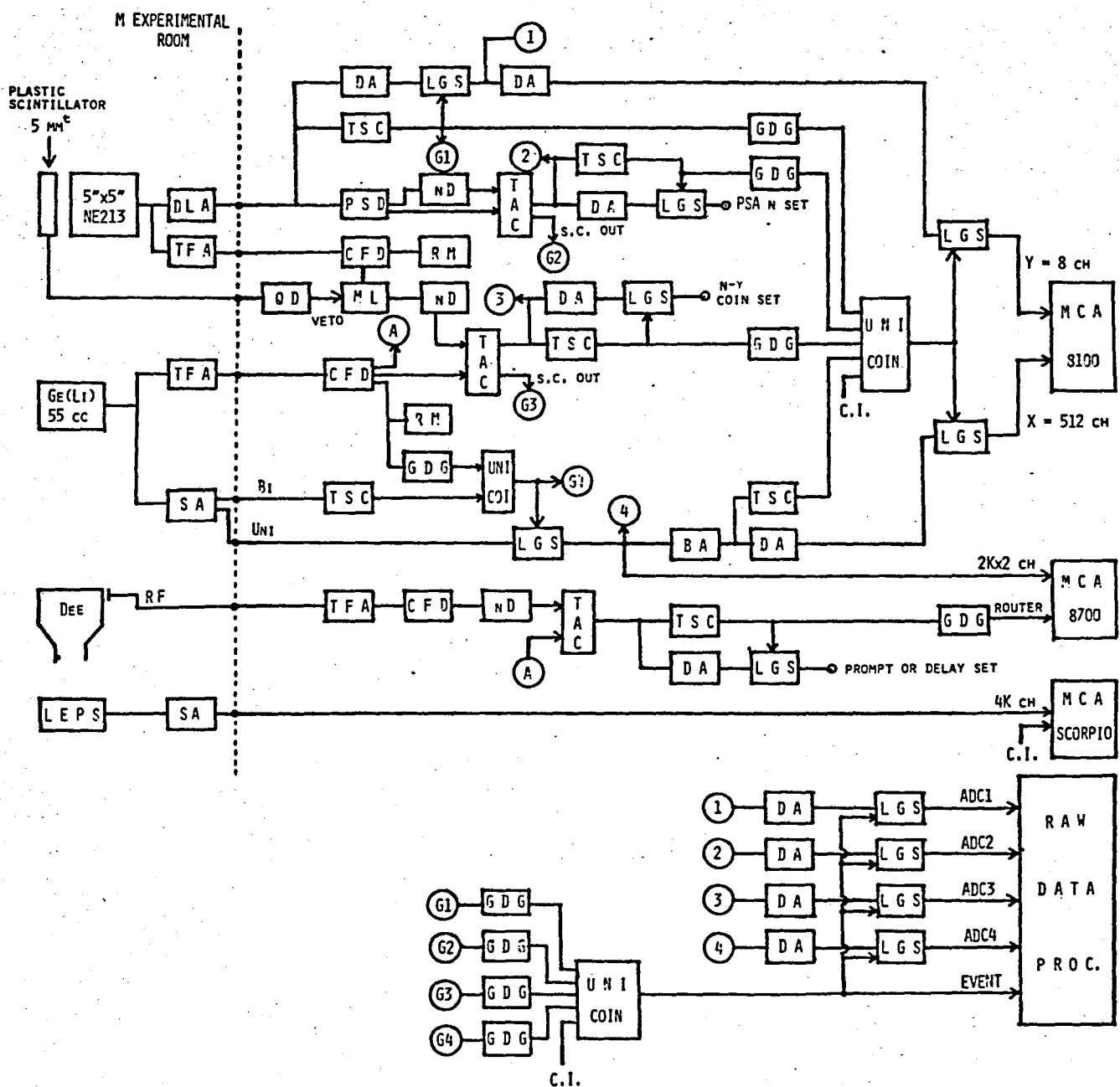


Fig. 2-9

NEUTRON - GAMMA DISCRIMINATION

5" ϕ x 5" NE 213
PSD Canberra 2160

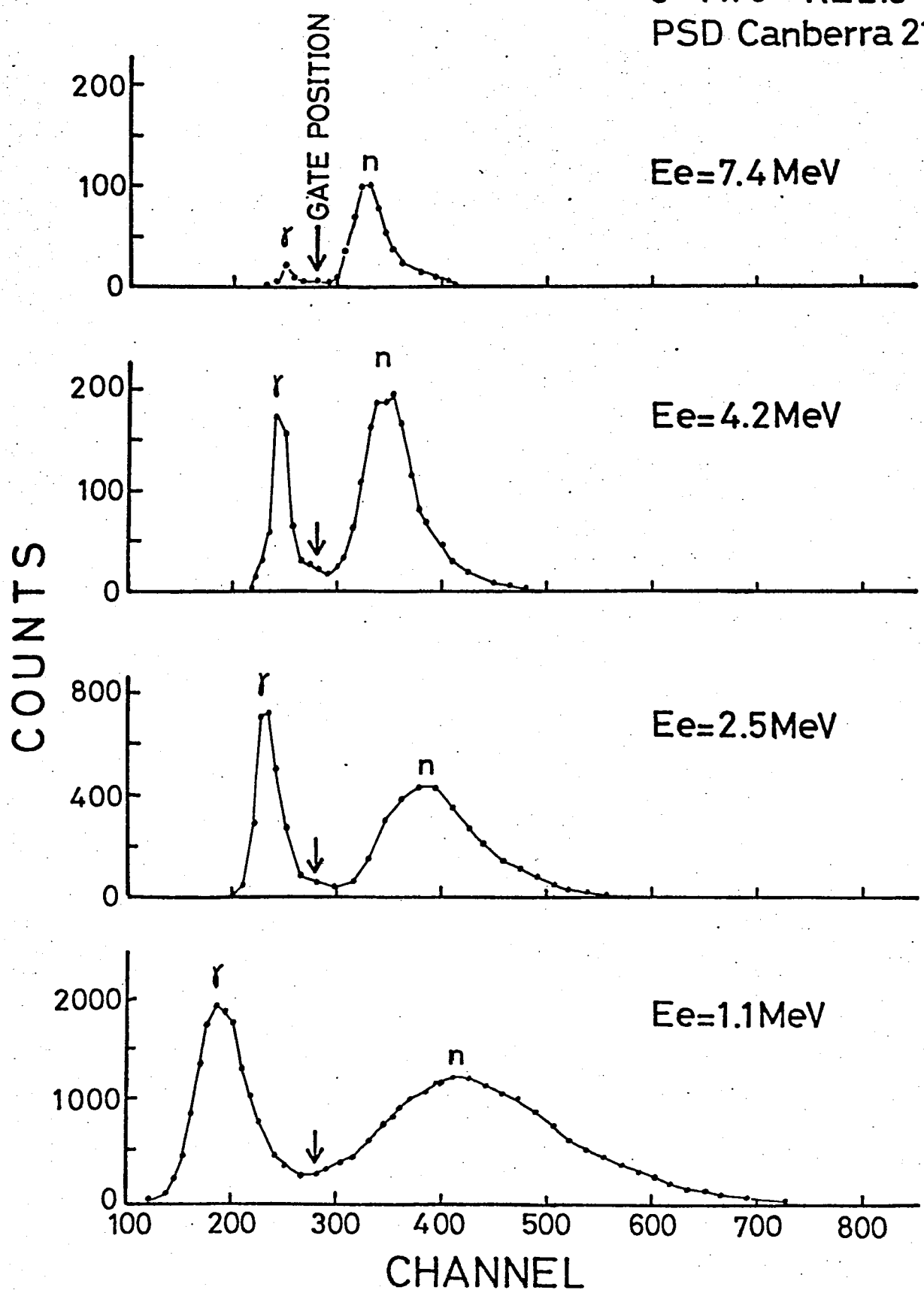


Fig. 2-10

n-TOF Spectra from $^{165}\text{Ho} + 110\text{MeV-}\alpha$ Reaction

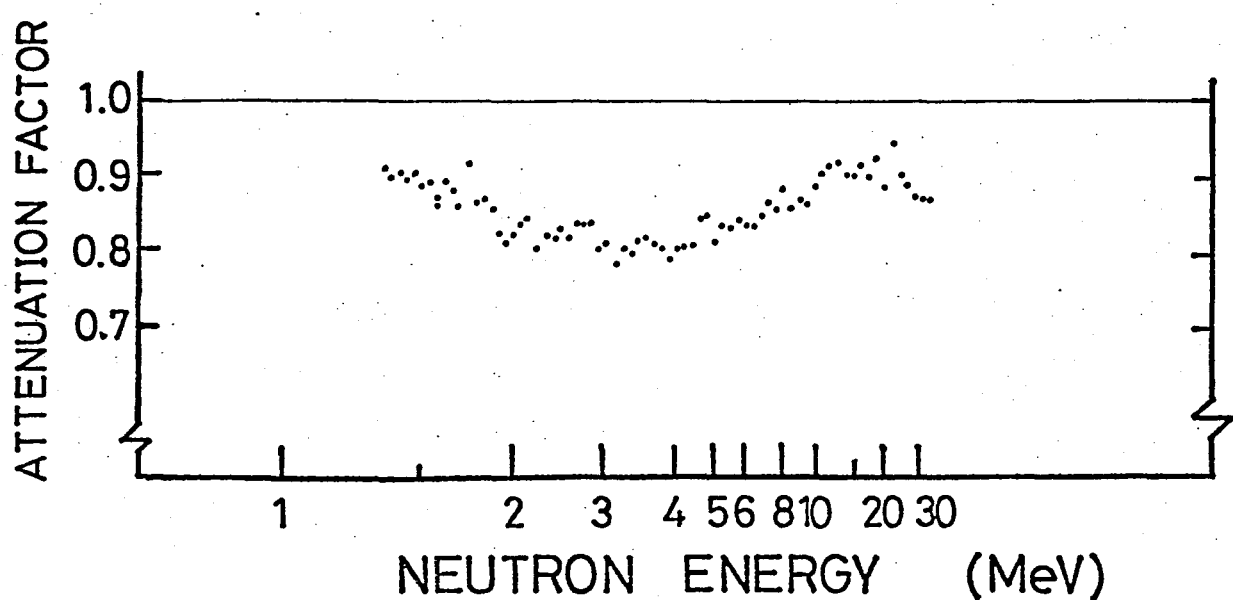
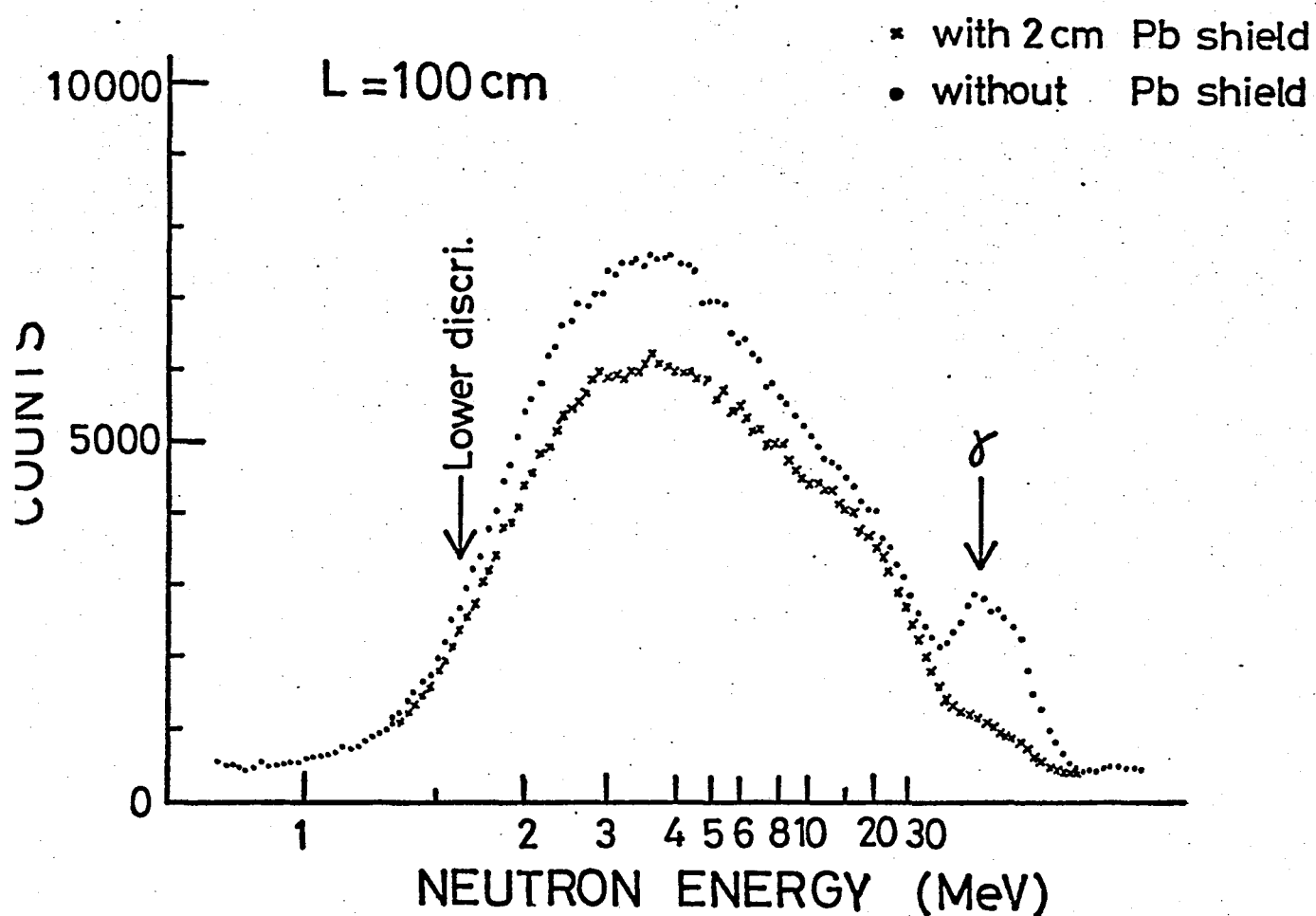


Fig. 2-11

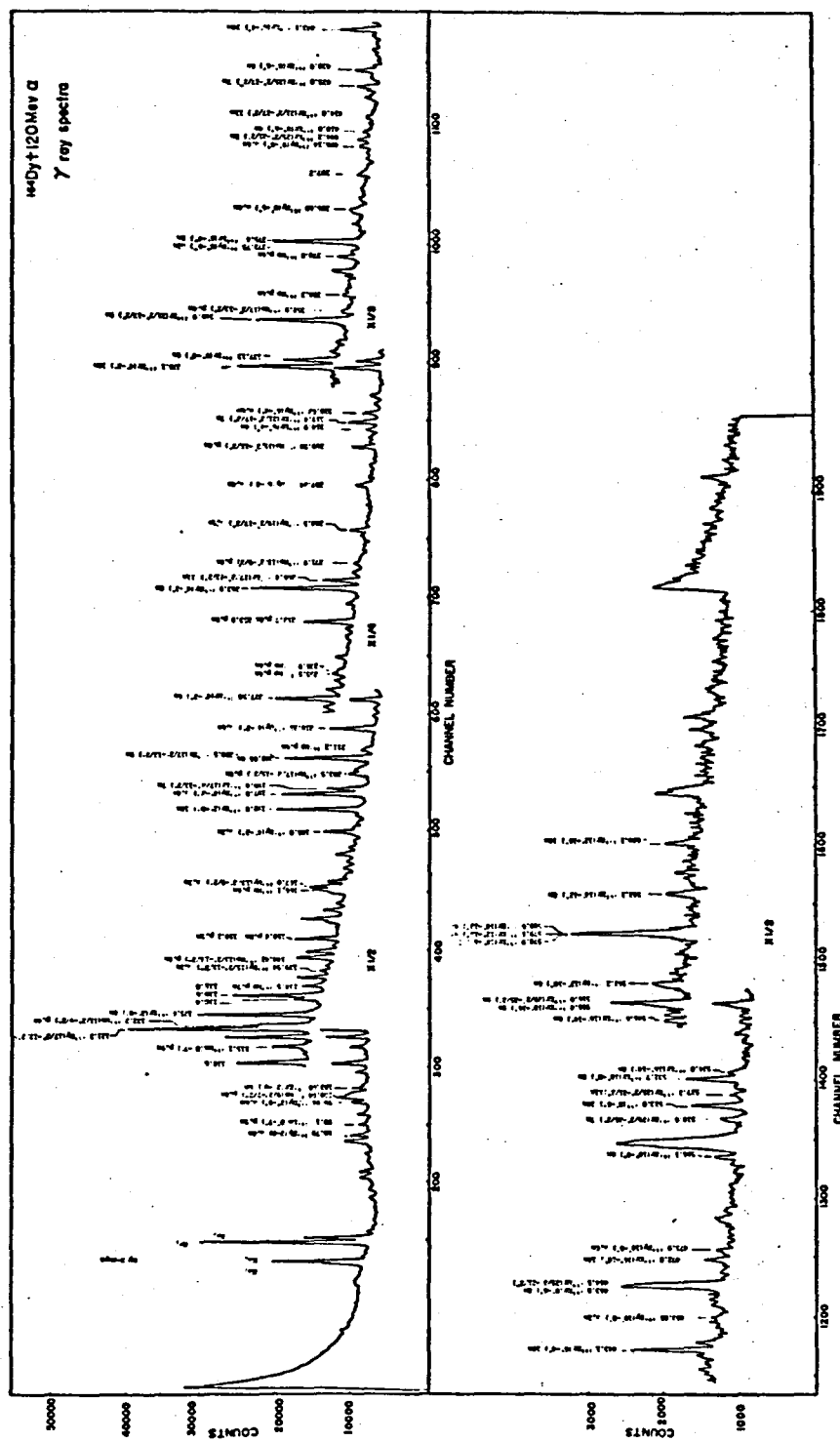


Fig. 3-1

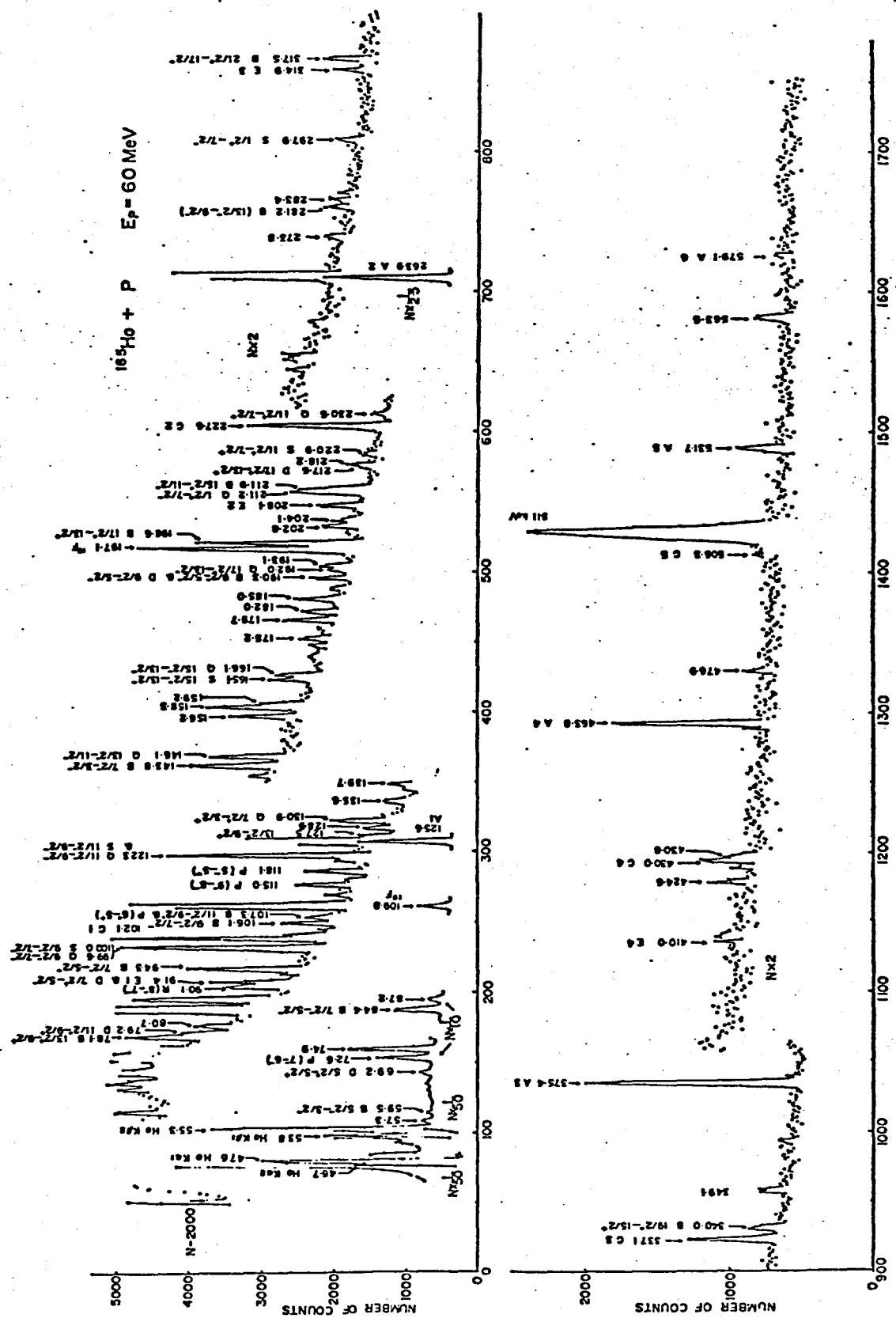


Fig. 3-2

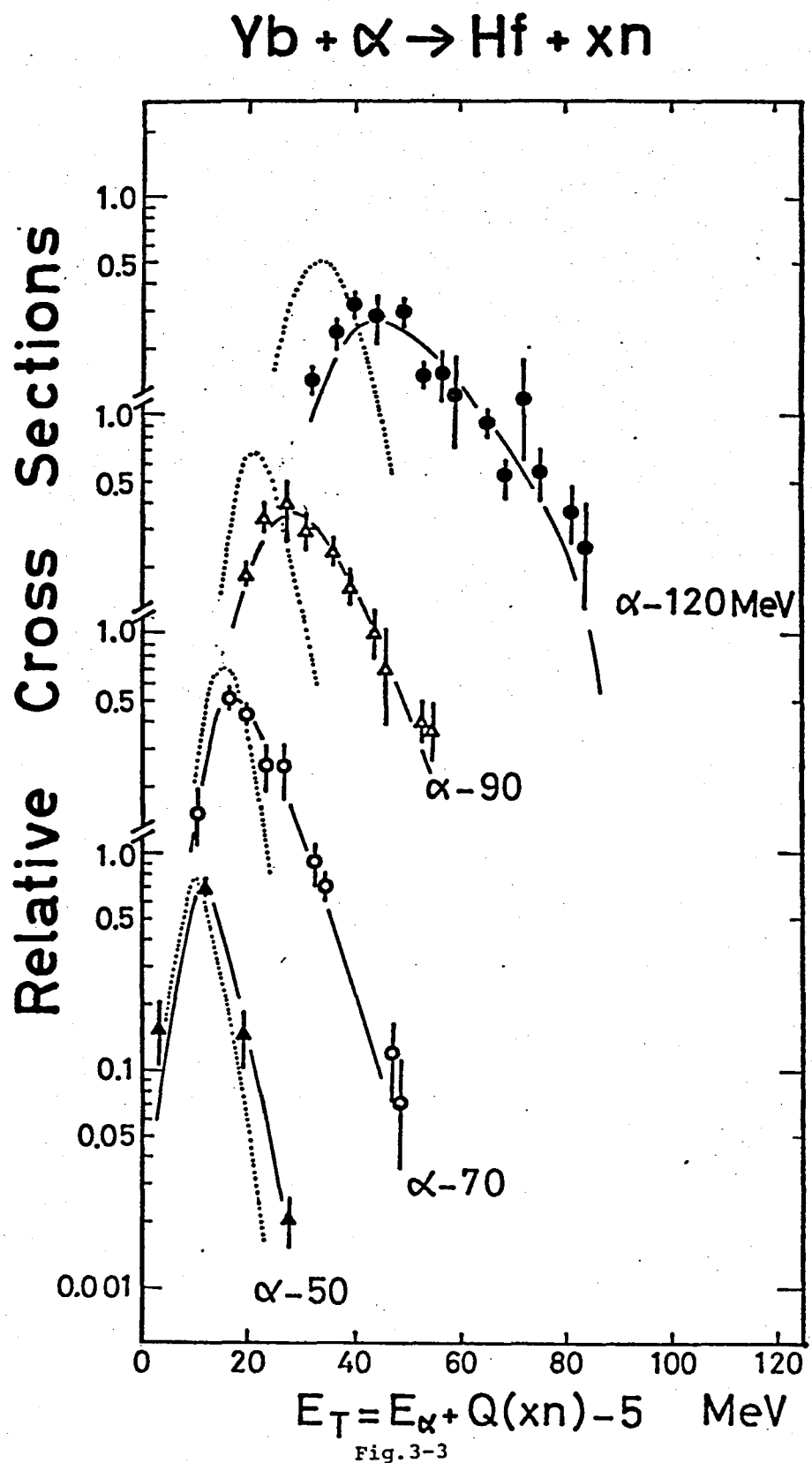


Fig. 3-3

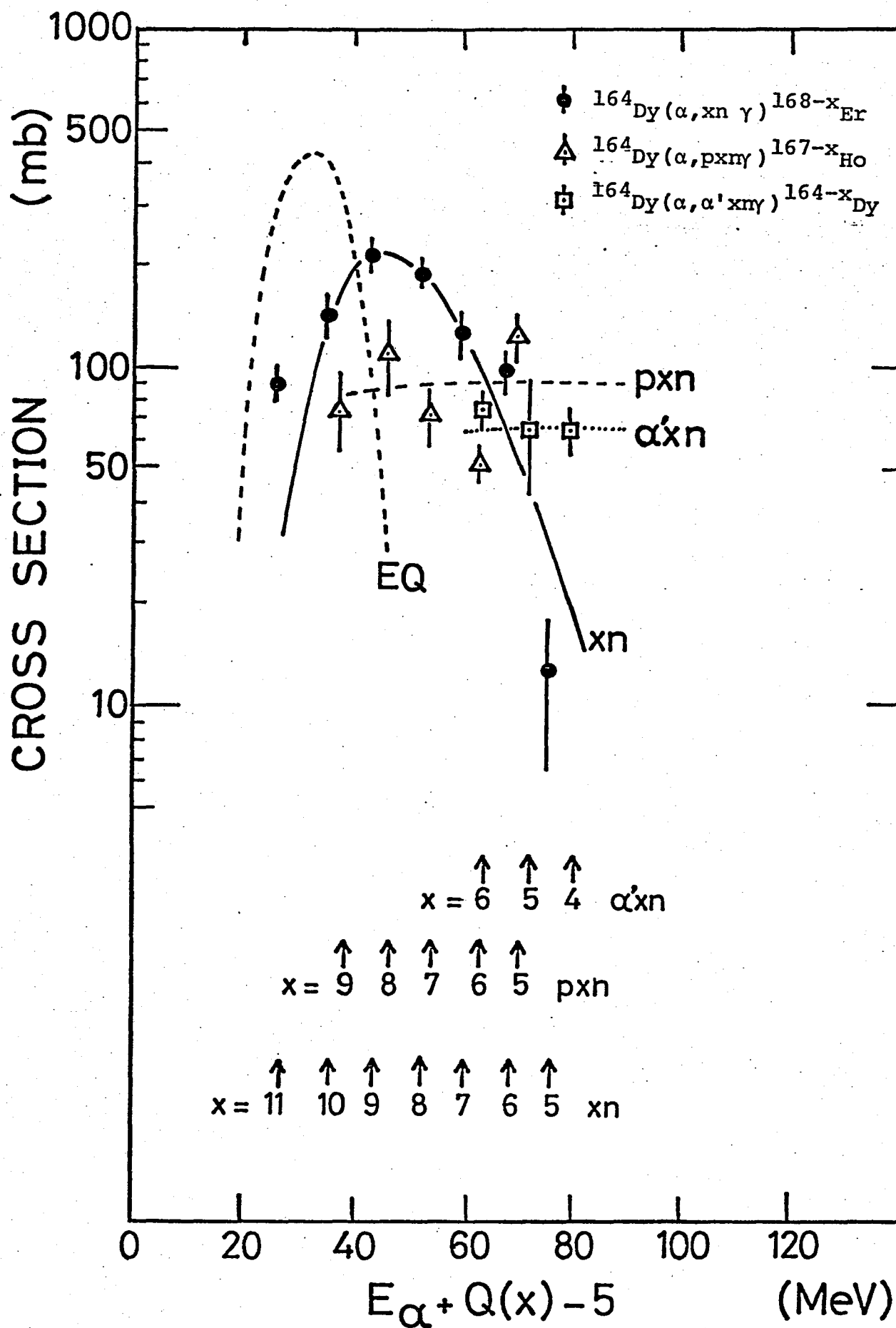


Fig. 3-4-a

174, 176 Yb + 120 MeV α

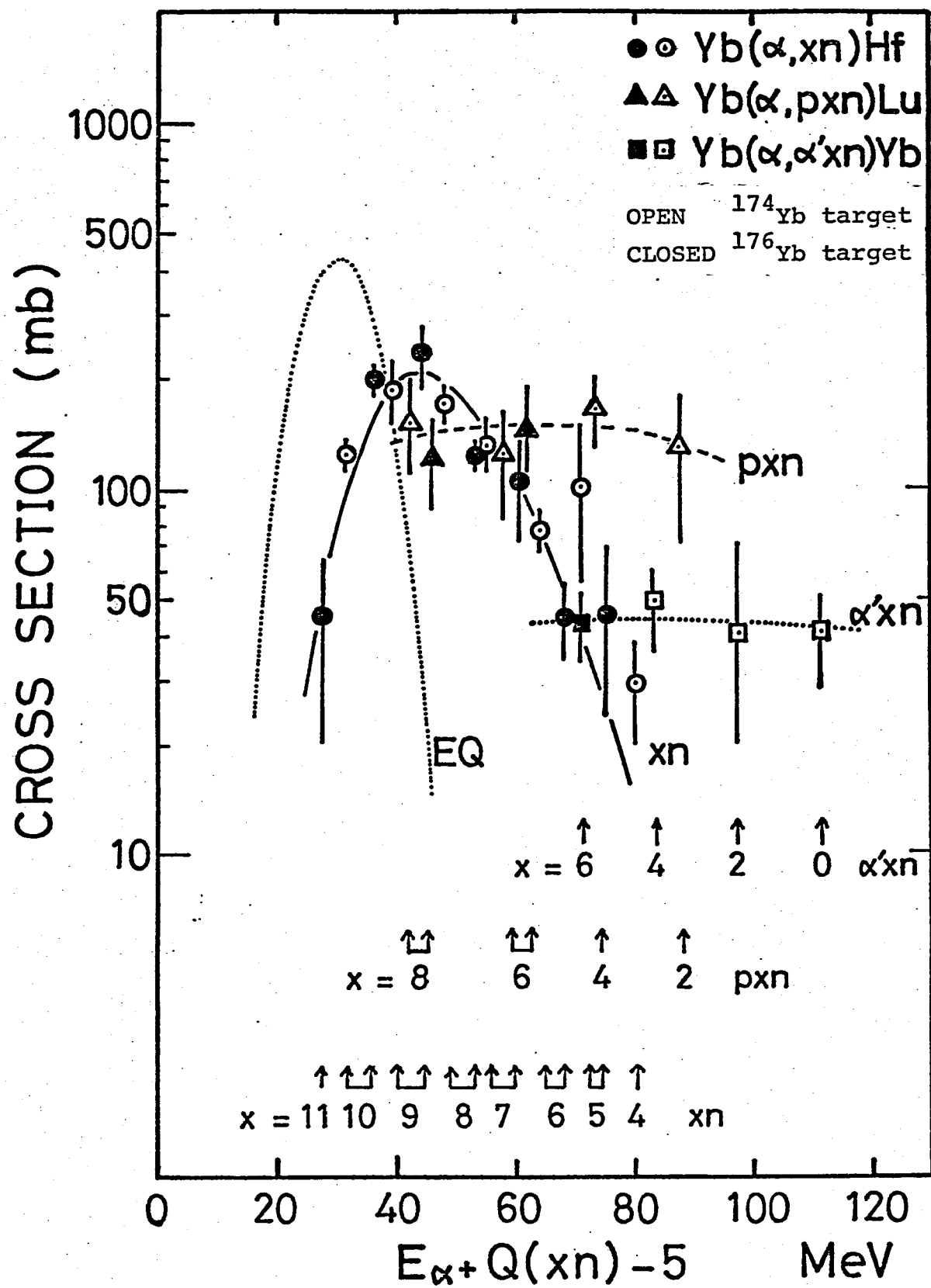


Fig. 3-4-b

$^{165}\text{Ho} + 120\text{ MeV } \alpha$

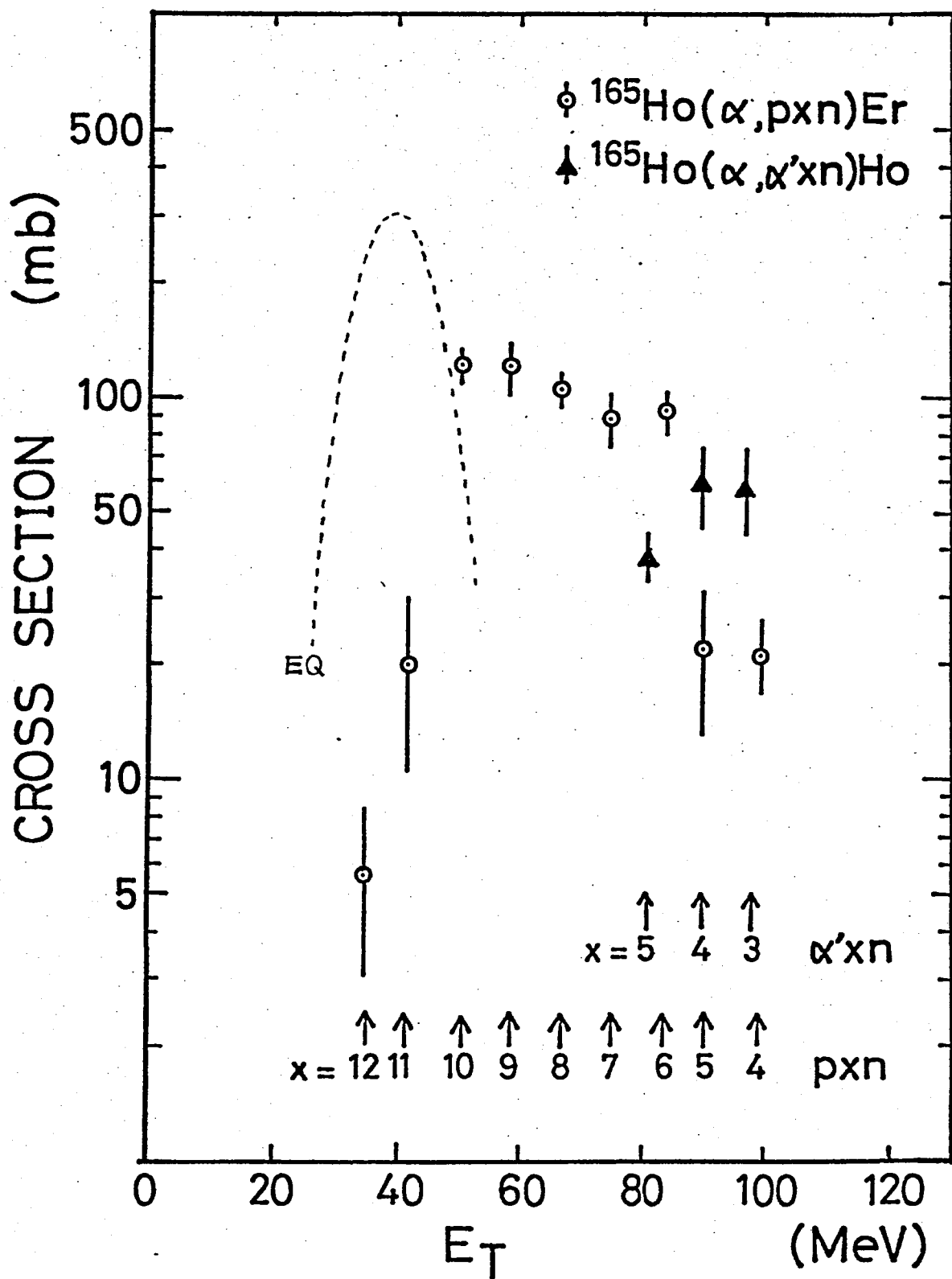


Fig. 3-5

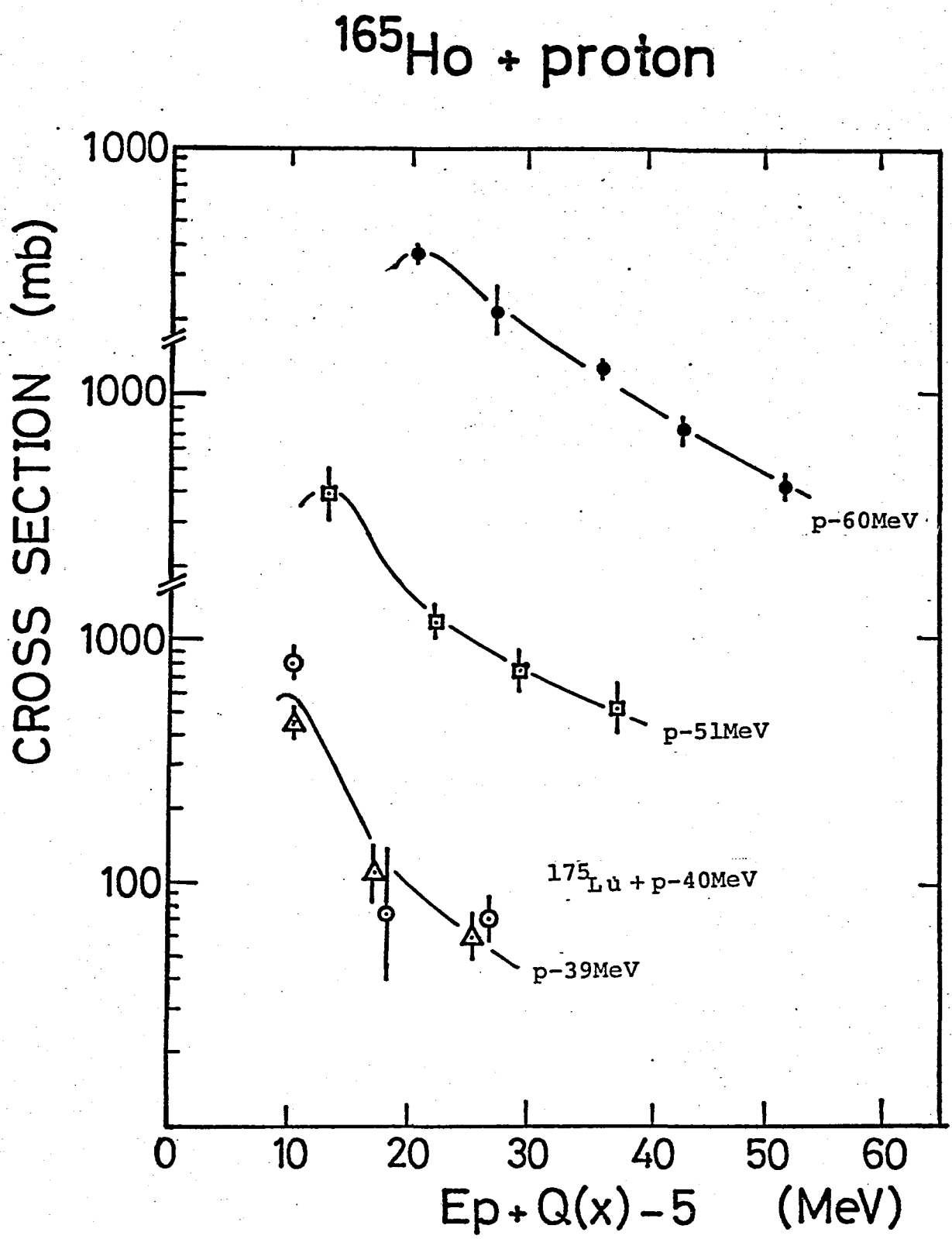


Fig. 3-6

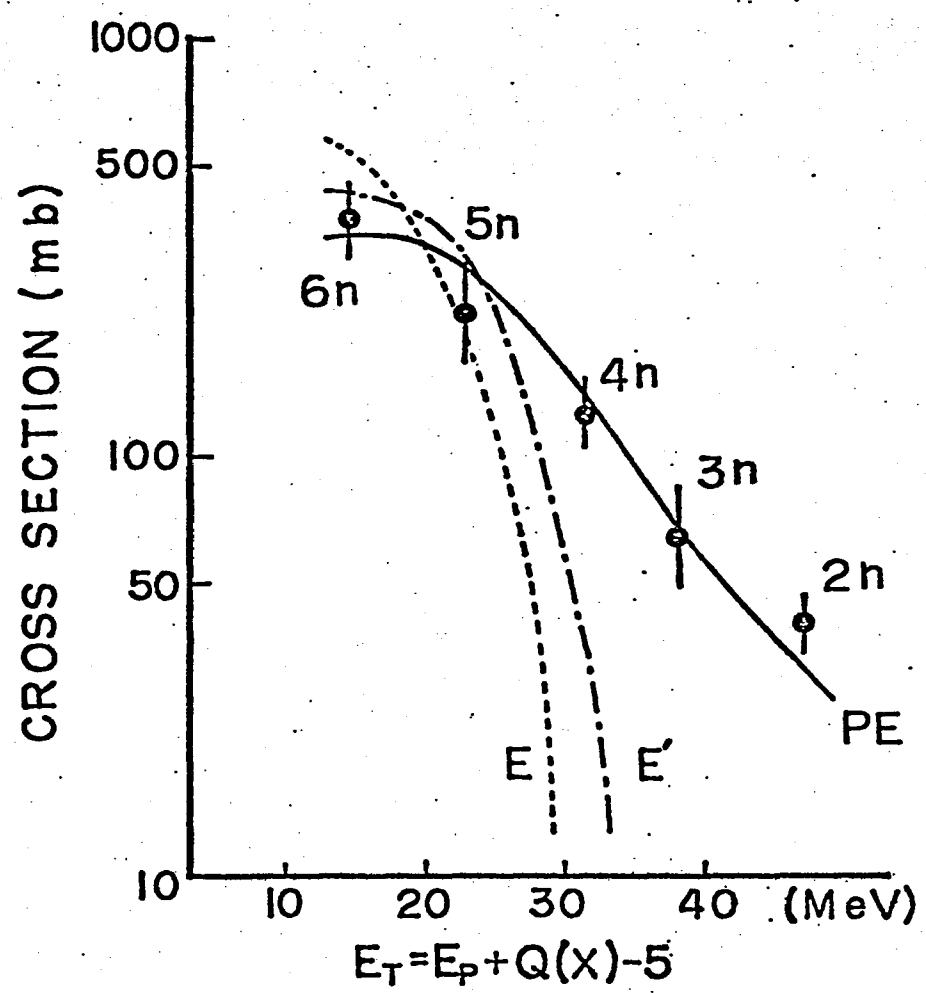


Fig. 3-6-b

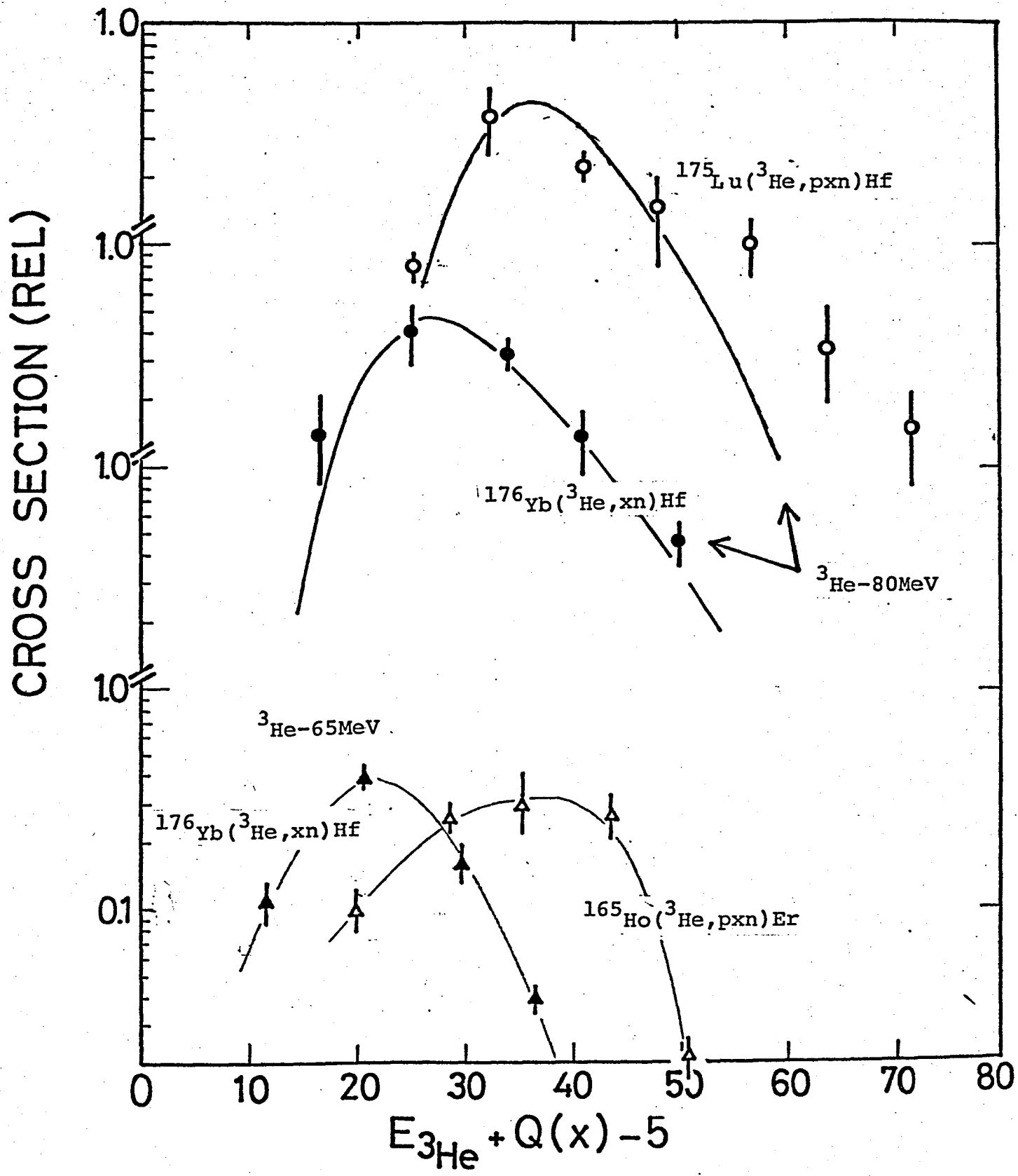


Fig. 3-7

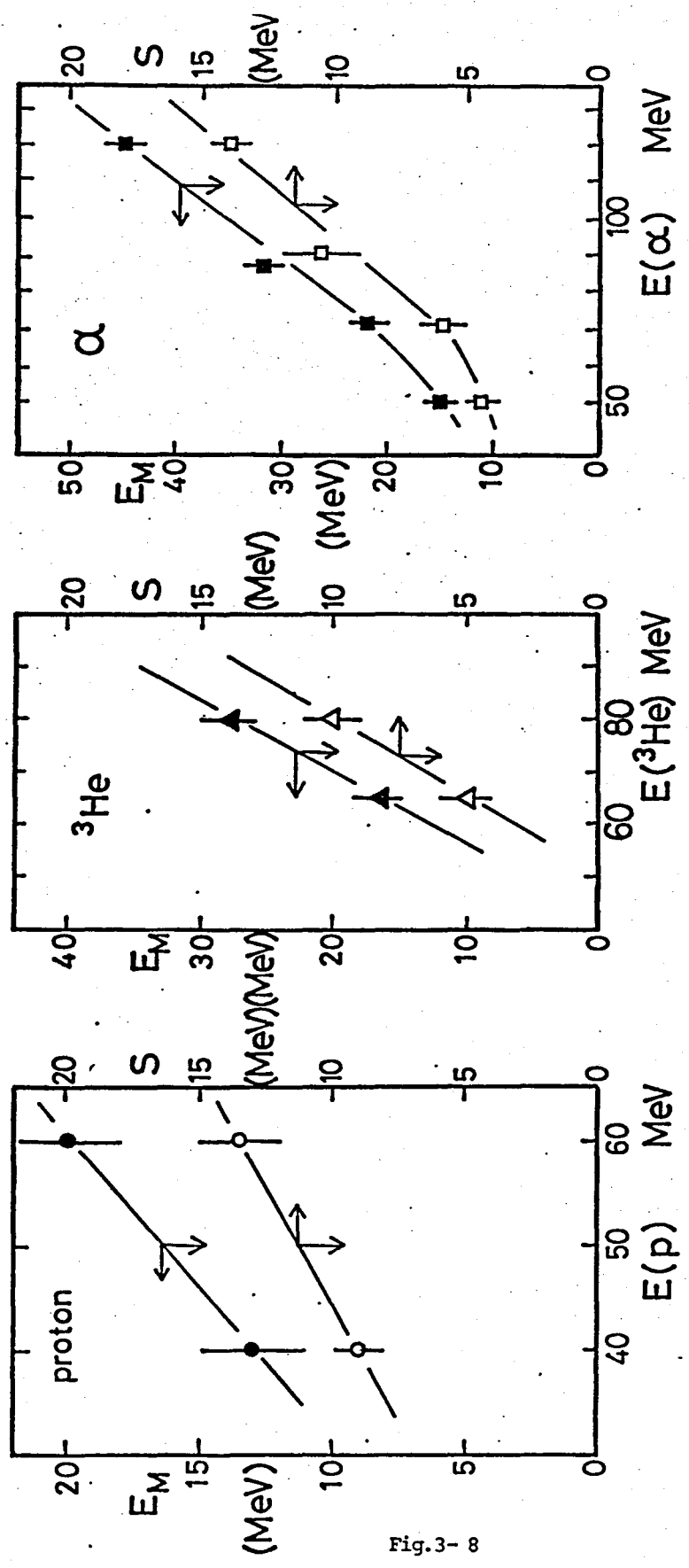


Fig.3-8

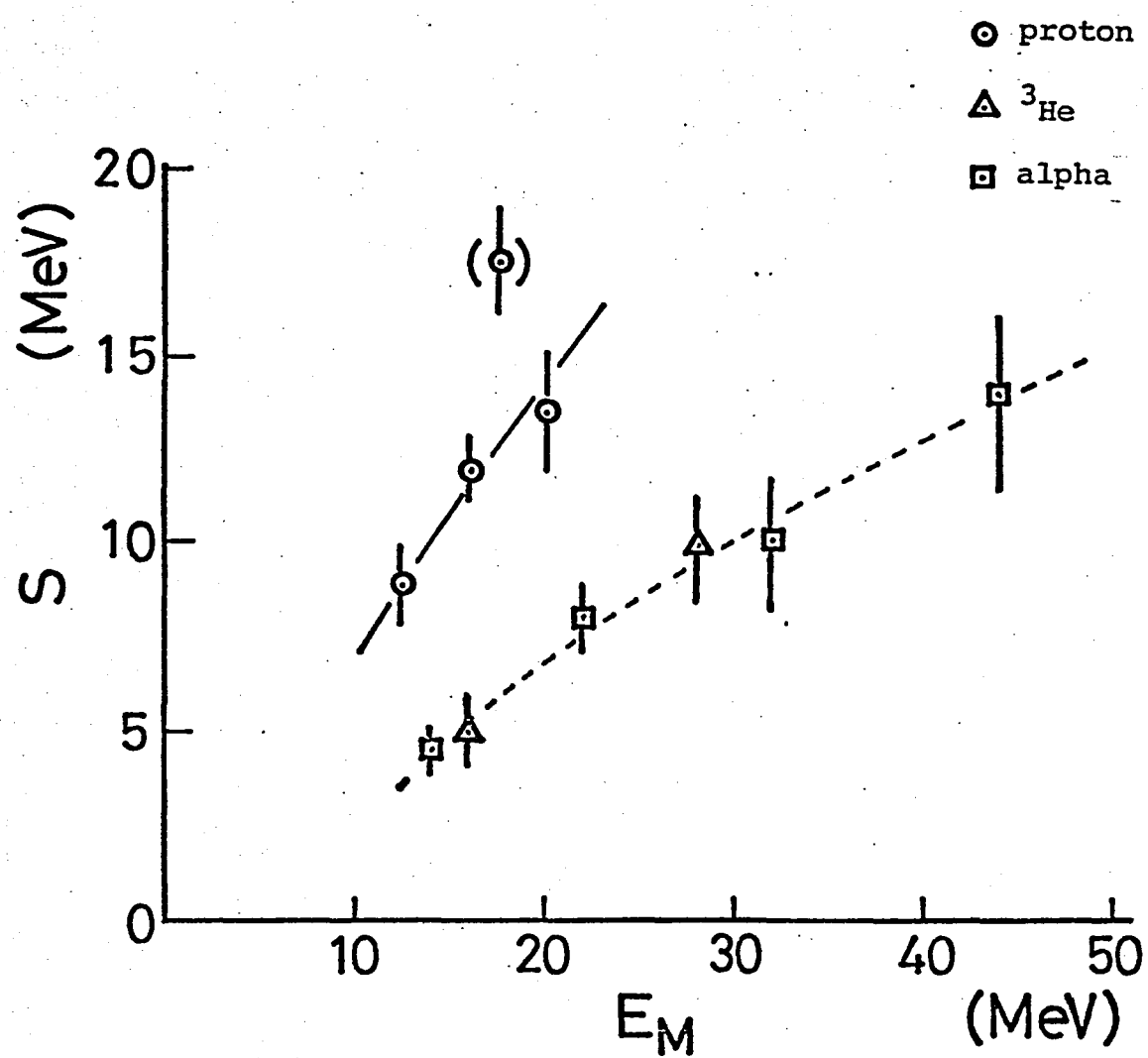


Fig. 3-9

IM MEDIAN SPIN

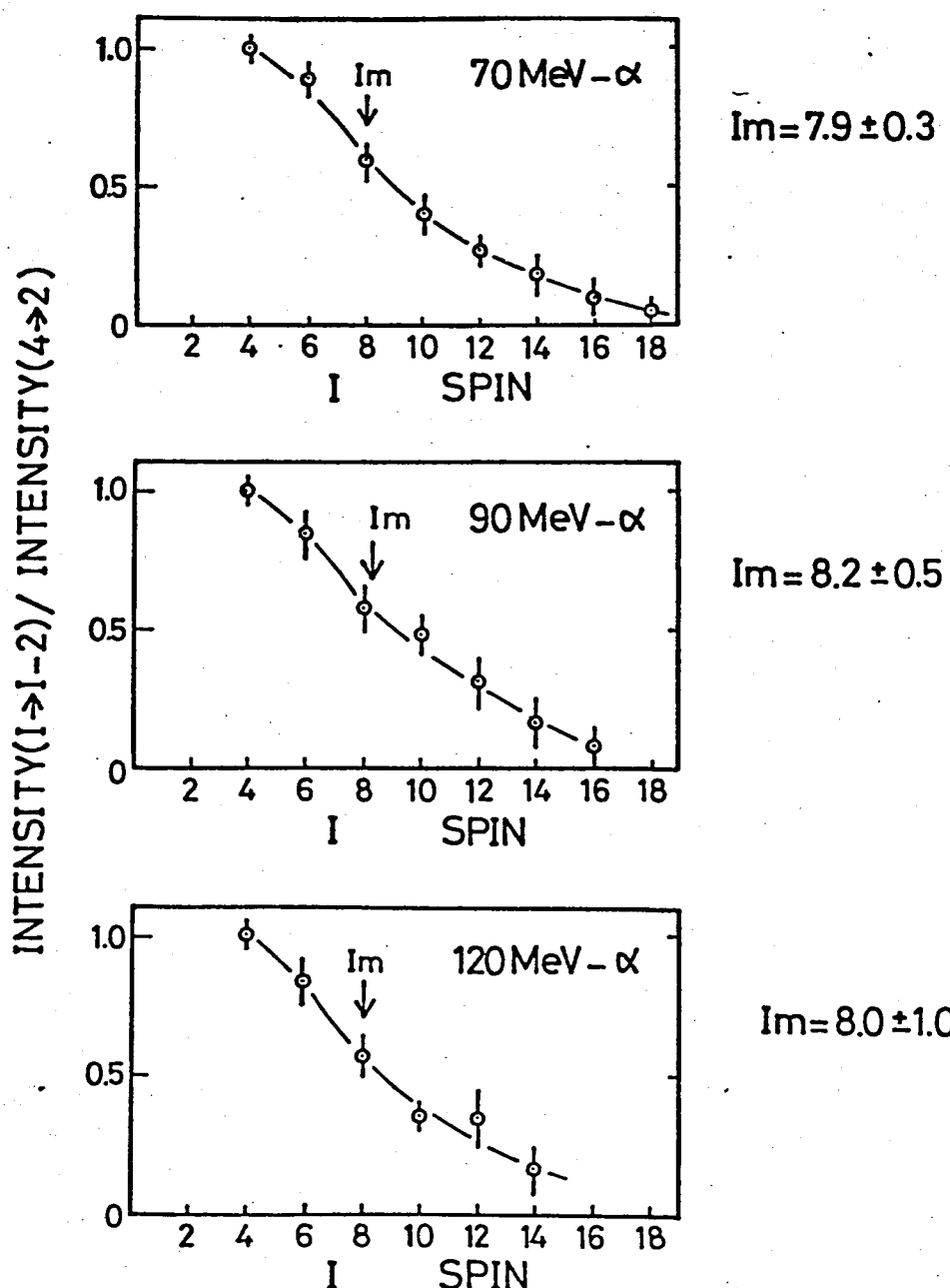
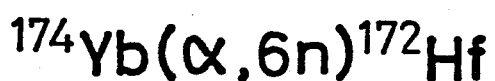


Fig. 3-10

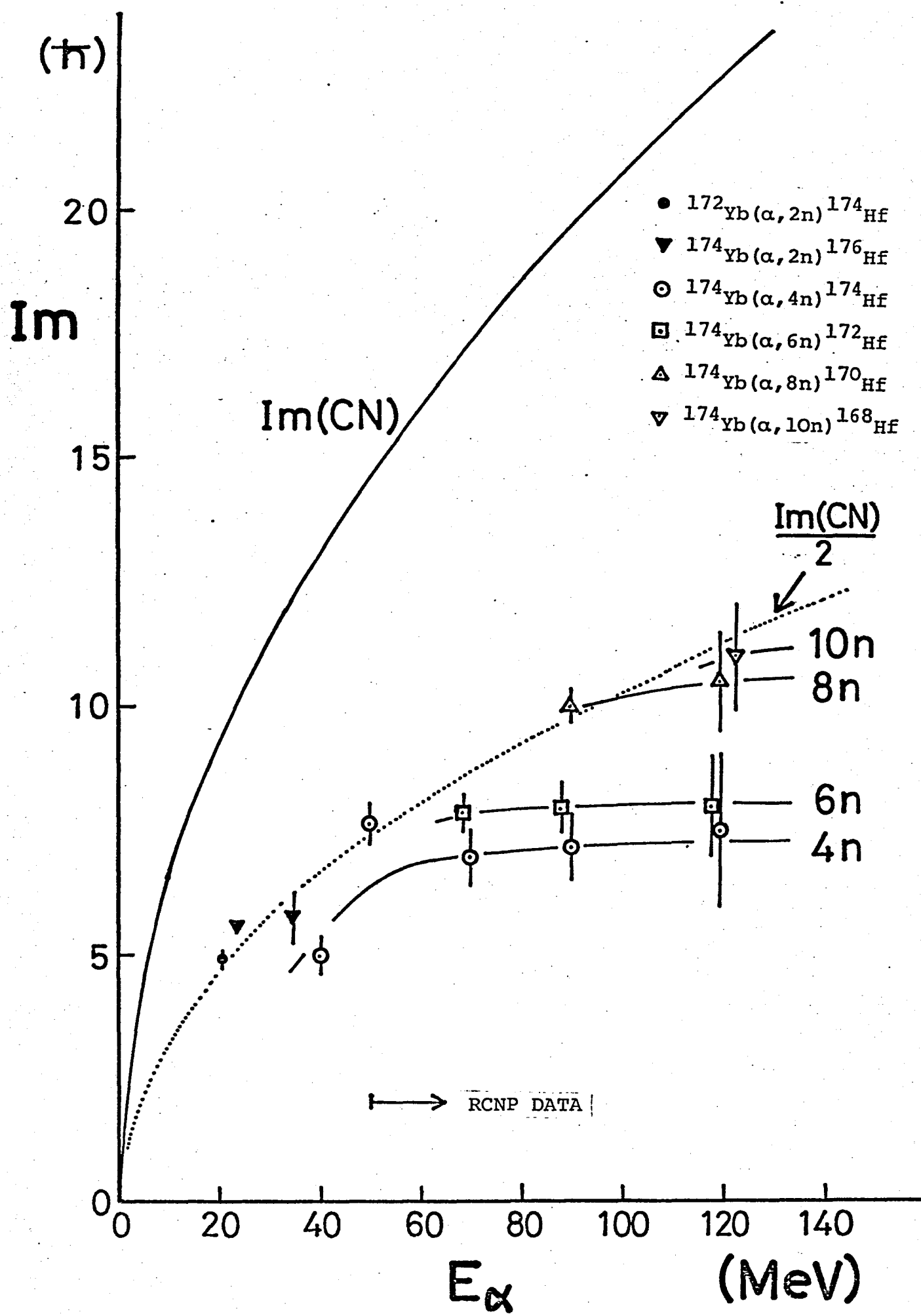


Fig. 3-11-a

Er ISOTOPE I_m DISTRIBUTION

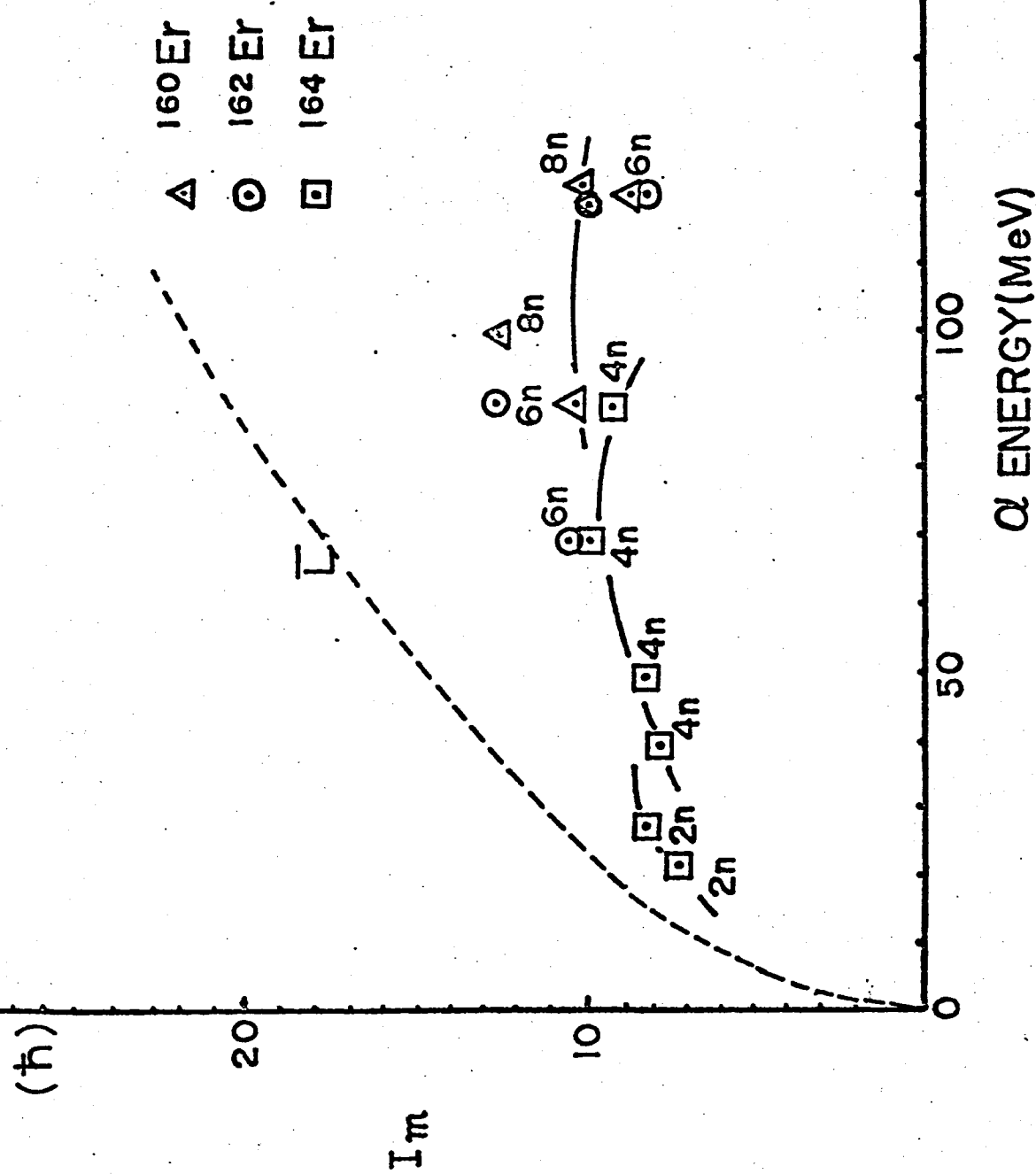
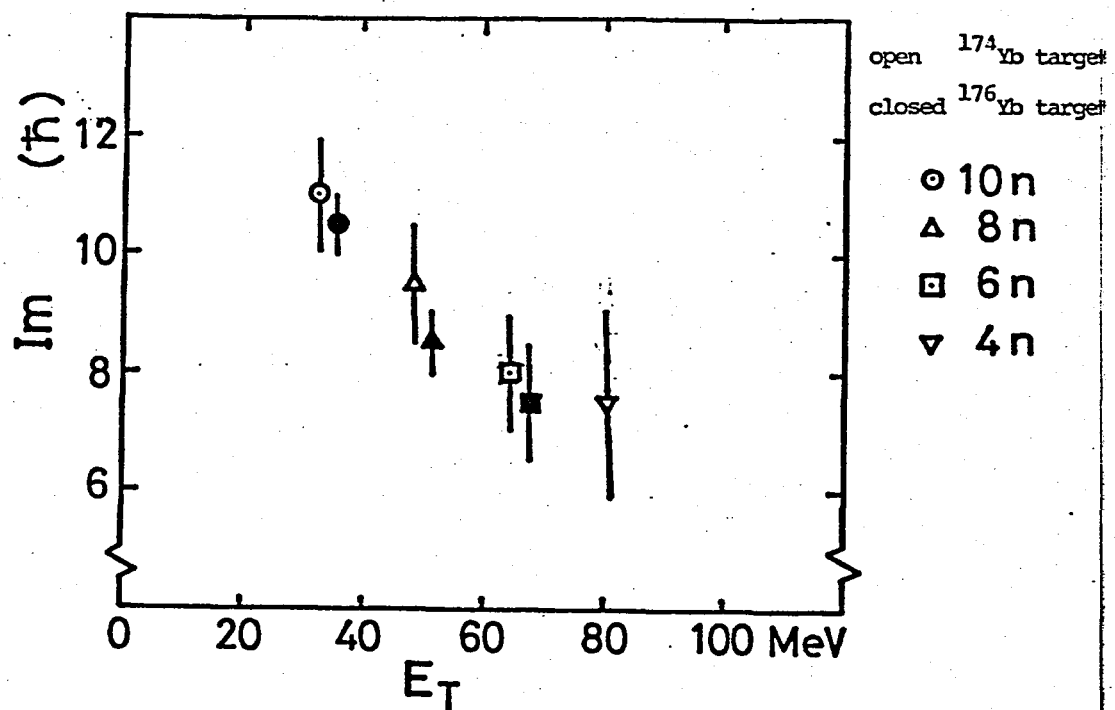
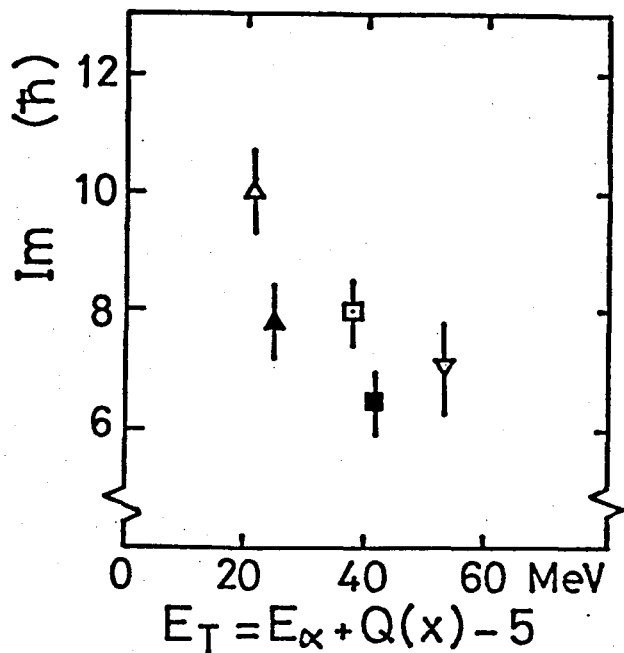


Fig. 3-11-b

Yb + 120 MeV α



Yb + 90 MeV α



Yb + 70 MeV α

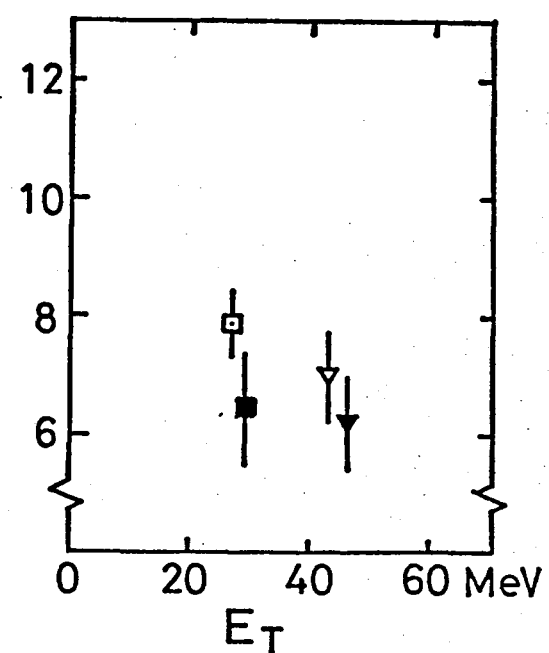


Fig. 3-12

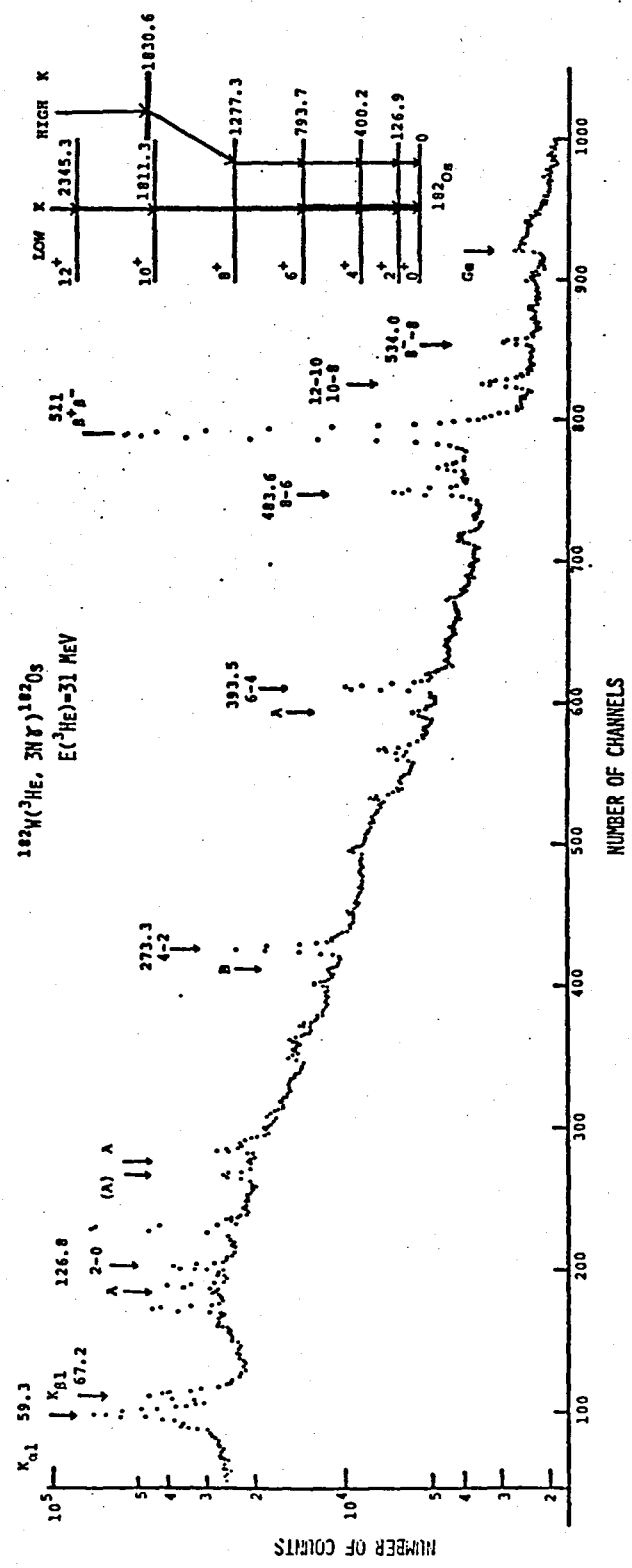
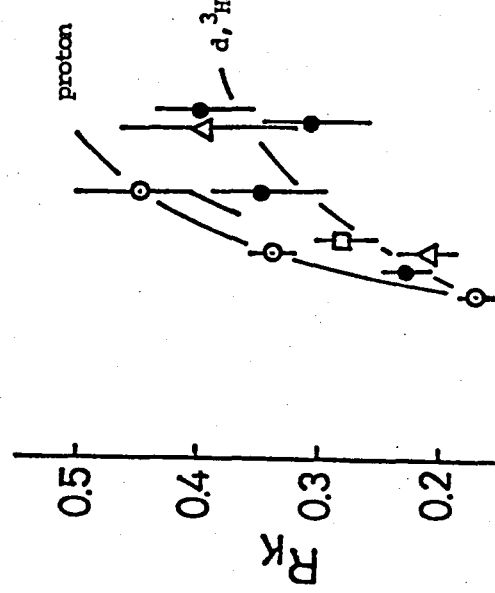


Fig. 3-13

K -isomer (6_6^+) Ratio

174Hf



172Hf

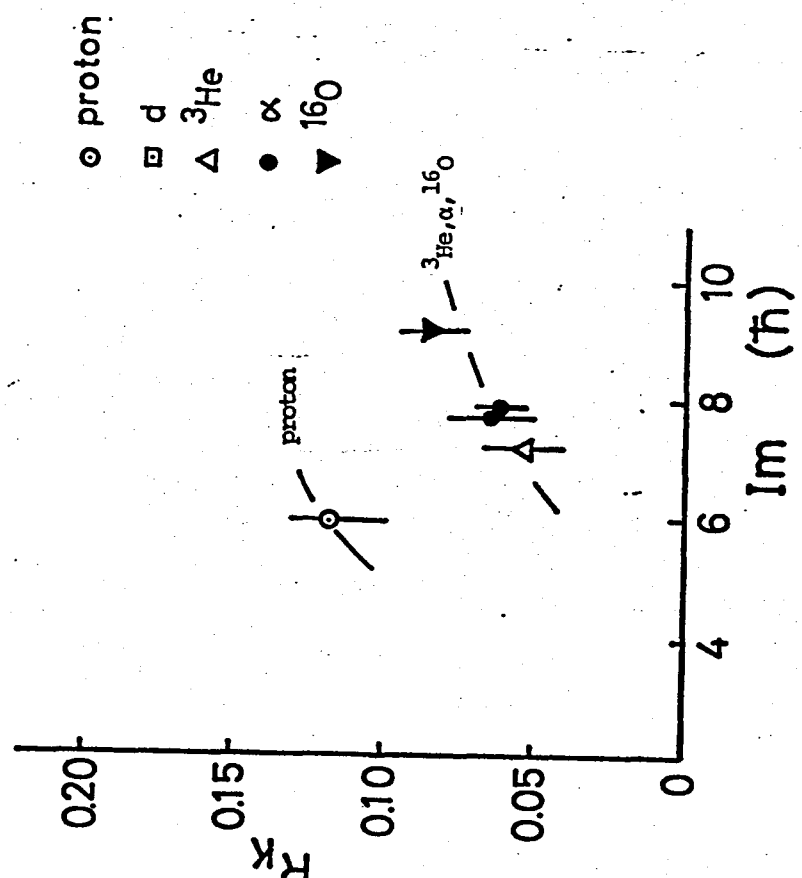


Fig. 3-14-a

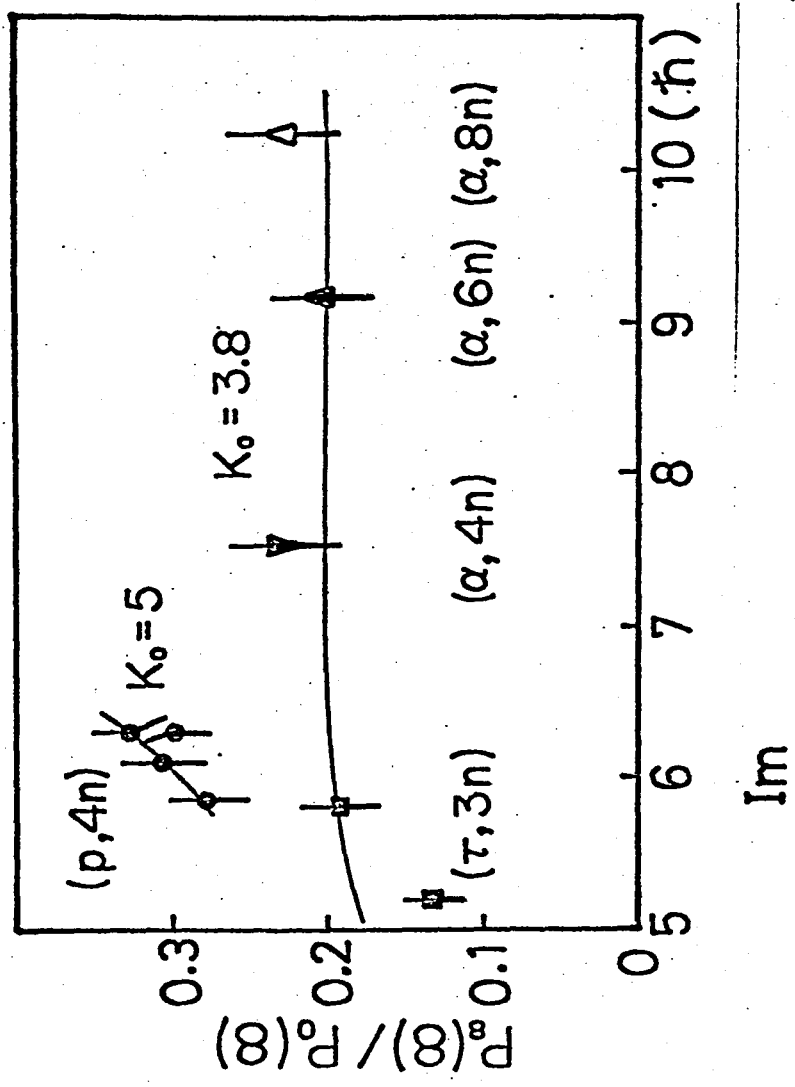


Fig. 3-14-b

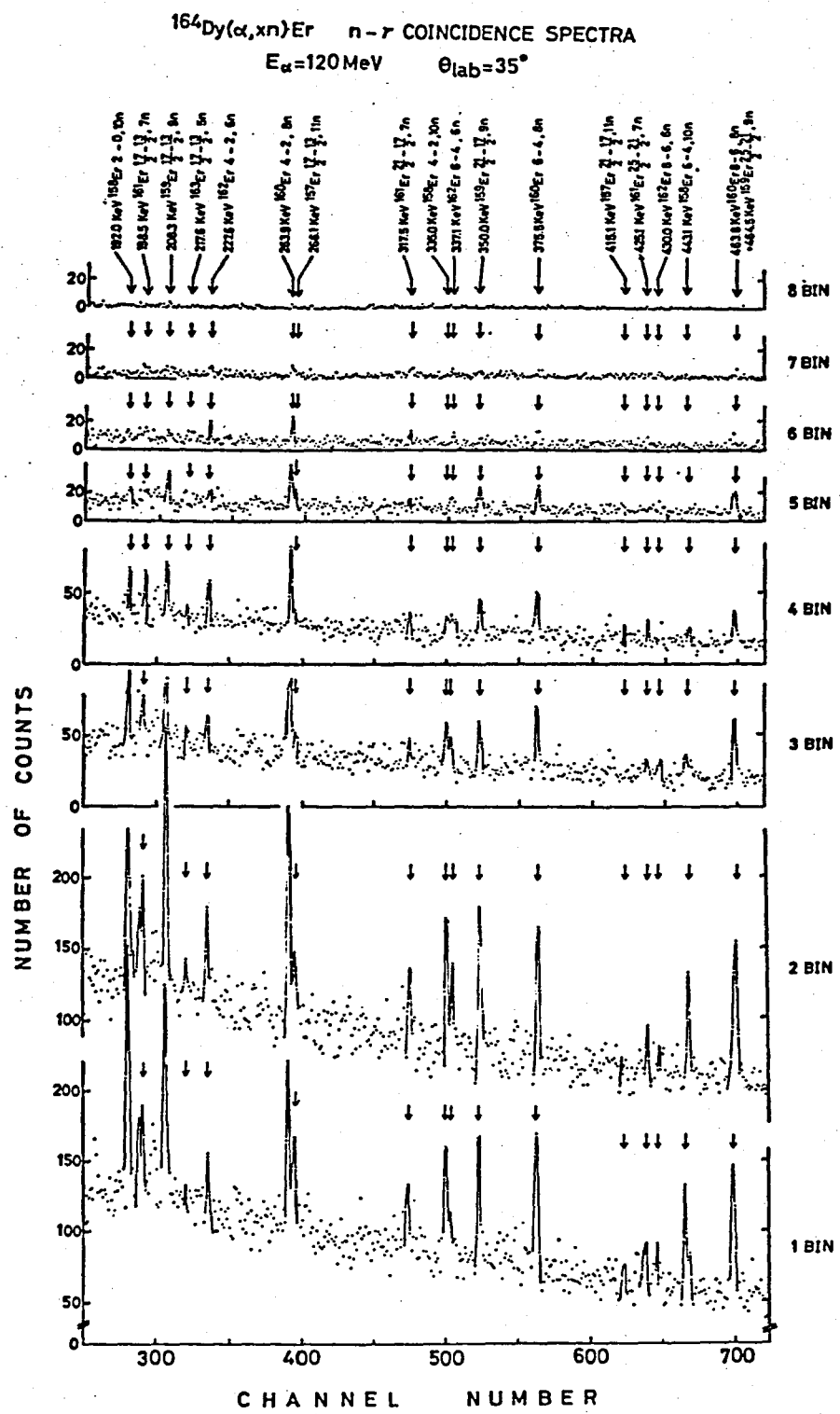


Fig. 3-15

Relative yield (MeV⁻¹)

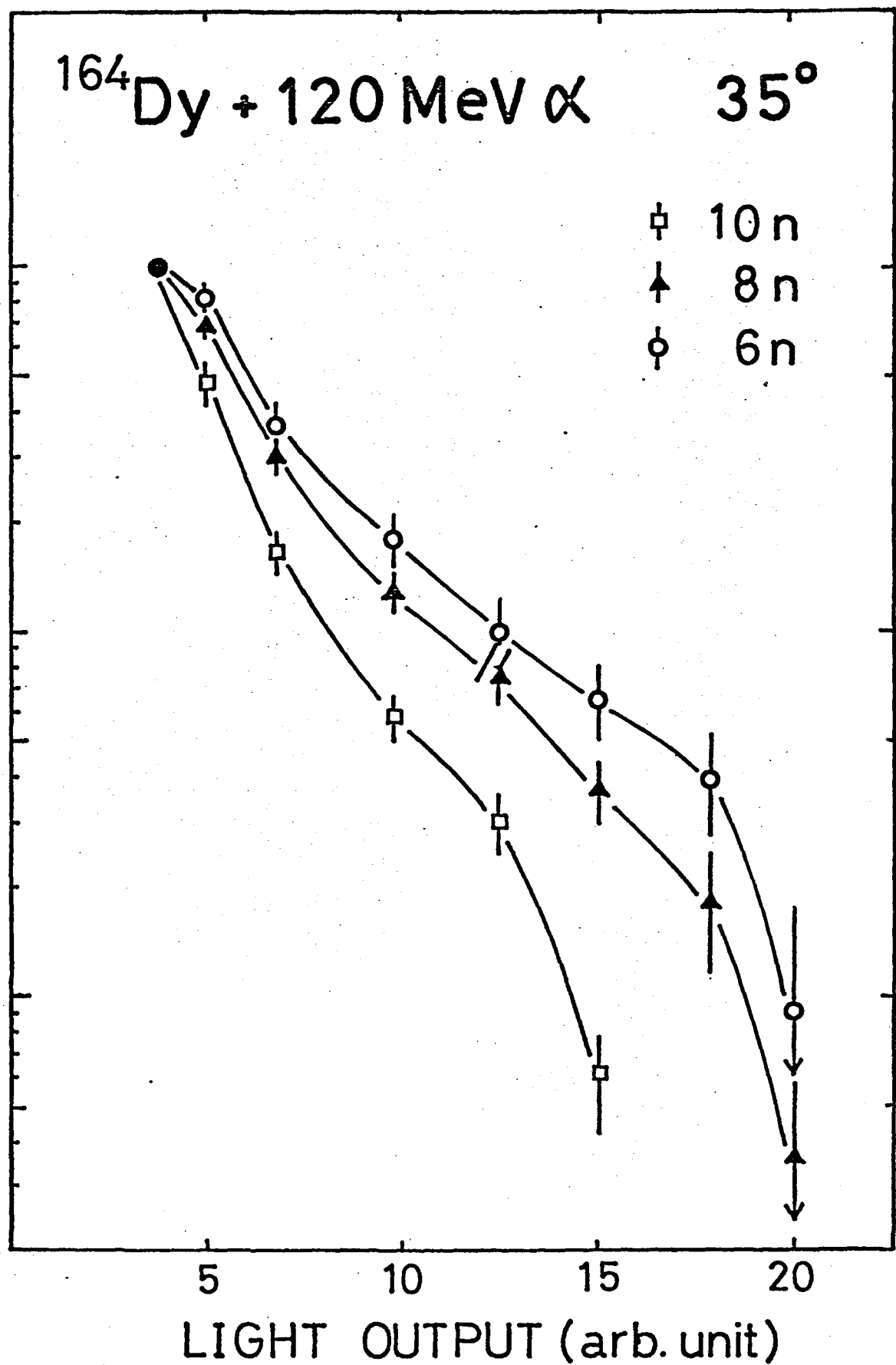
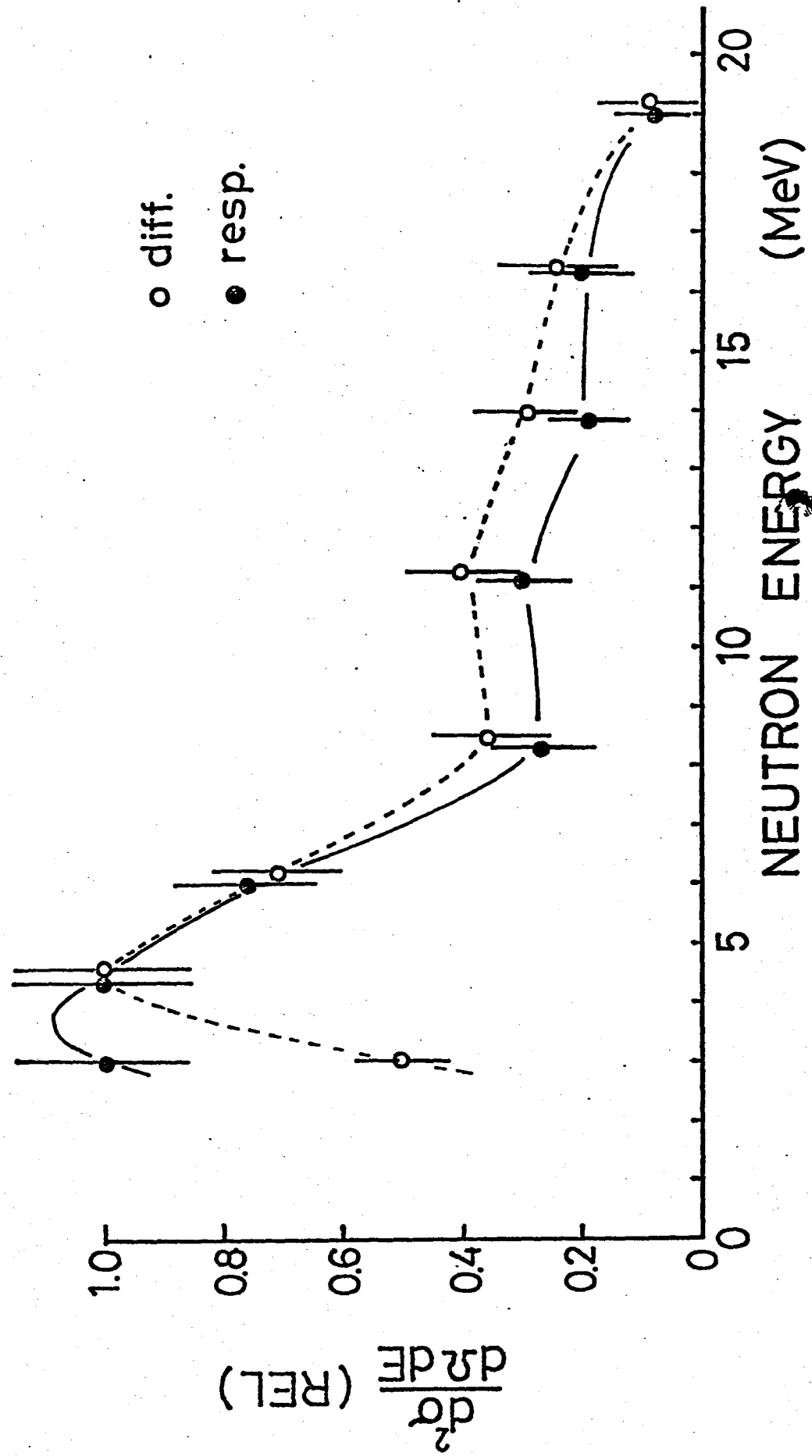


Fig. 3-16

$^{164}\text{Dy}(\alpha, 8n\delta)^{160}\text{Er}$

$\Theta = 35^\circ$



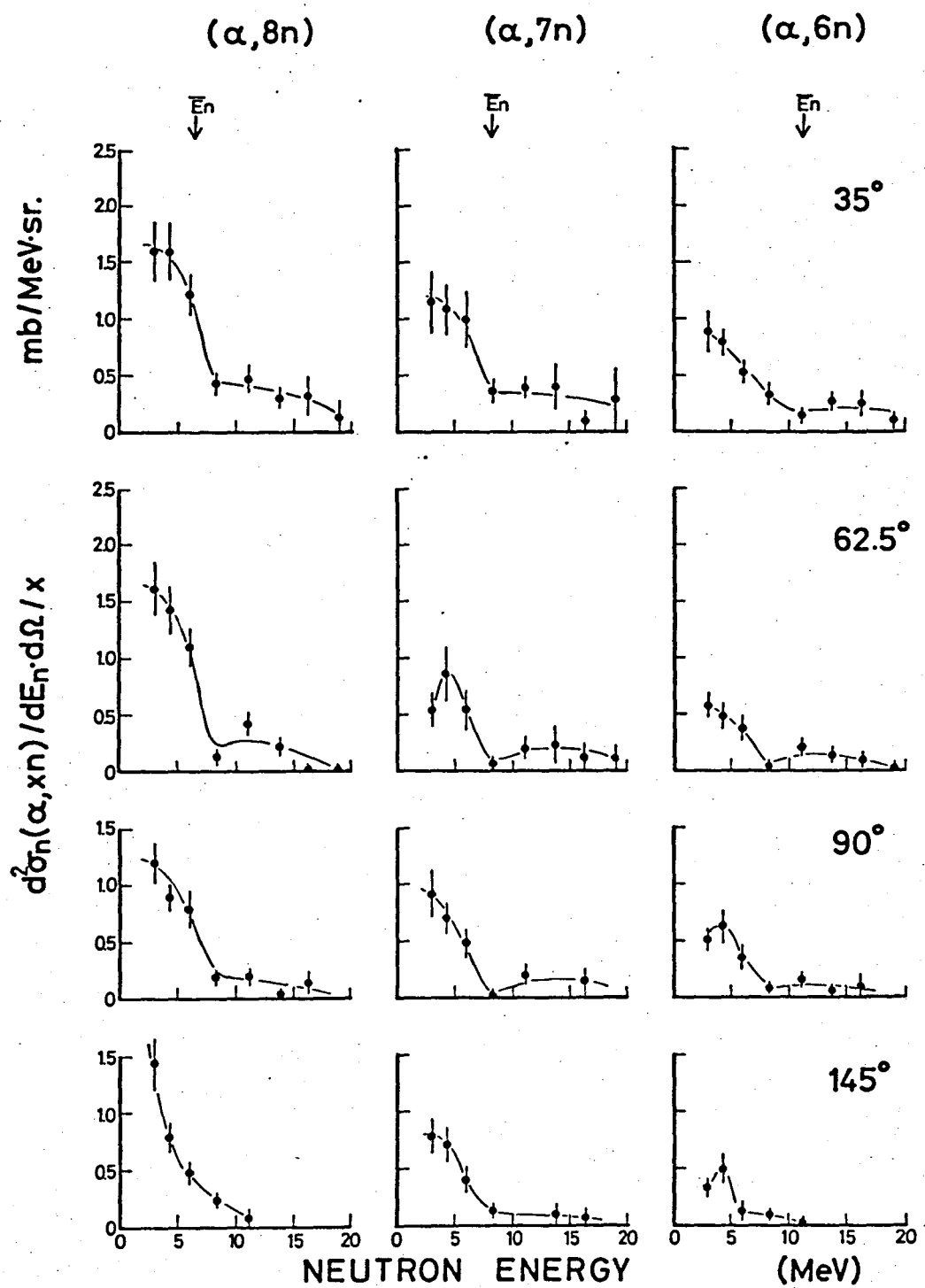


Fig. 3-18-a

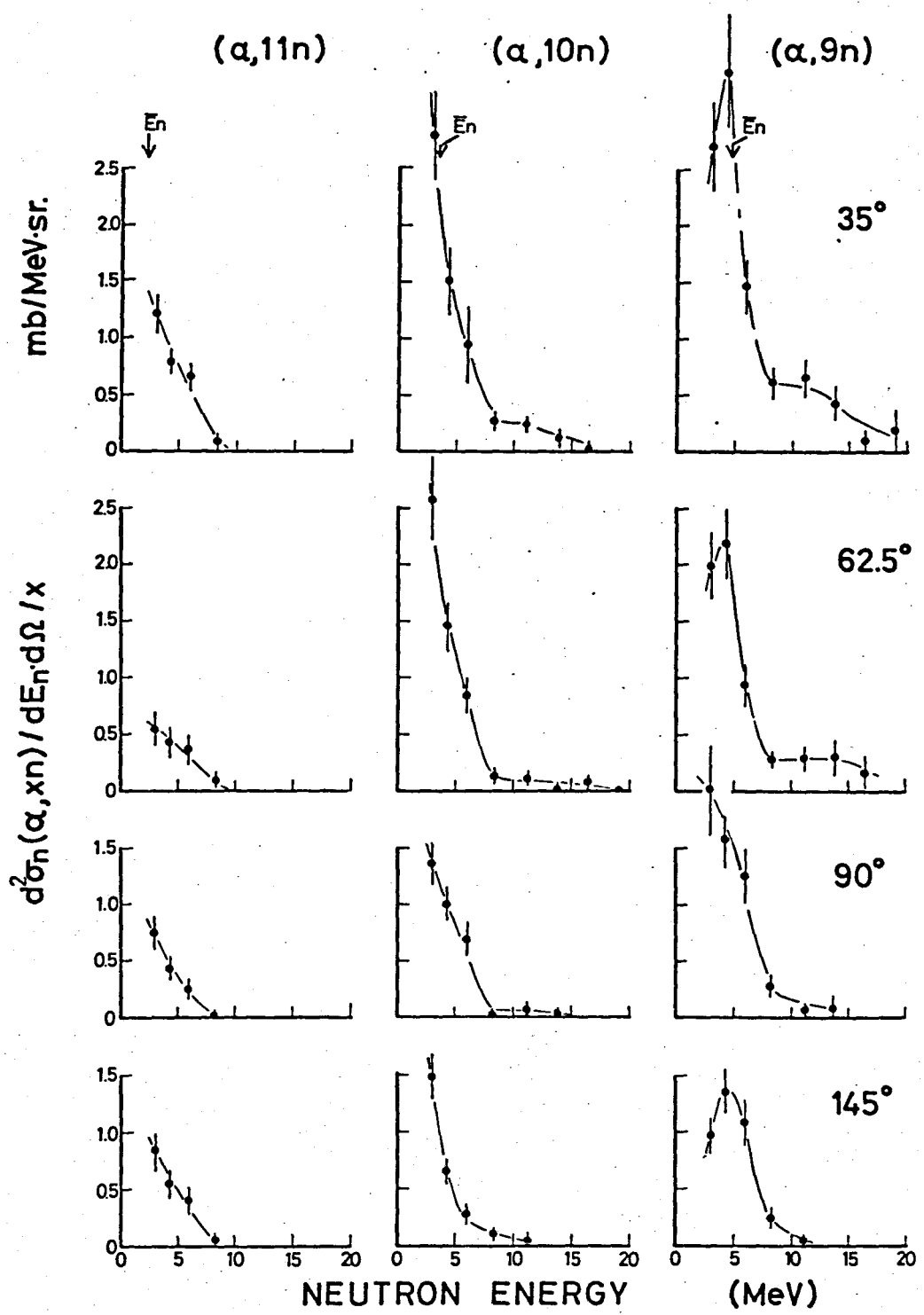


Fig. 3-18-a

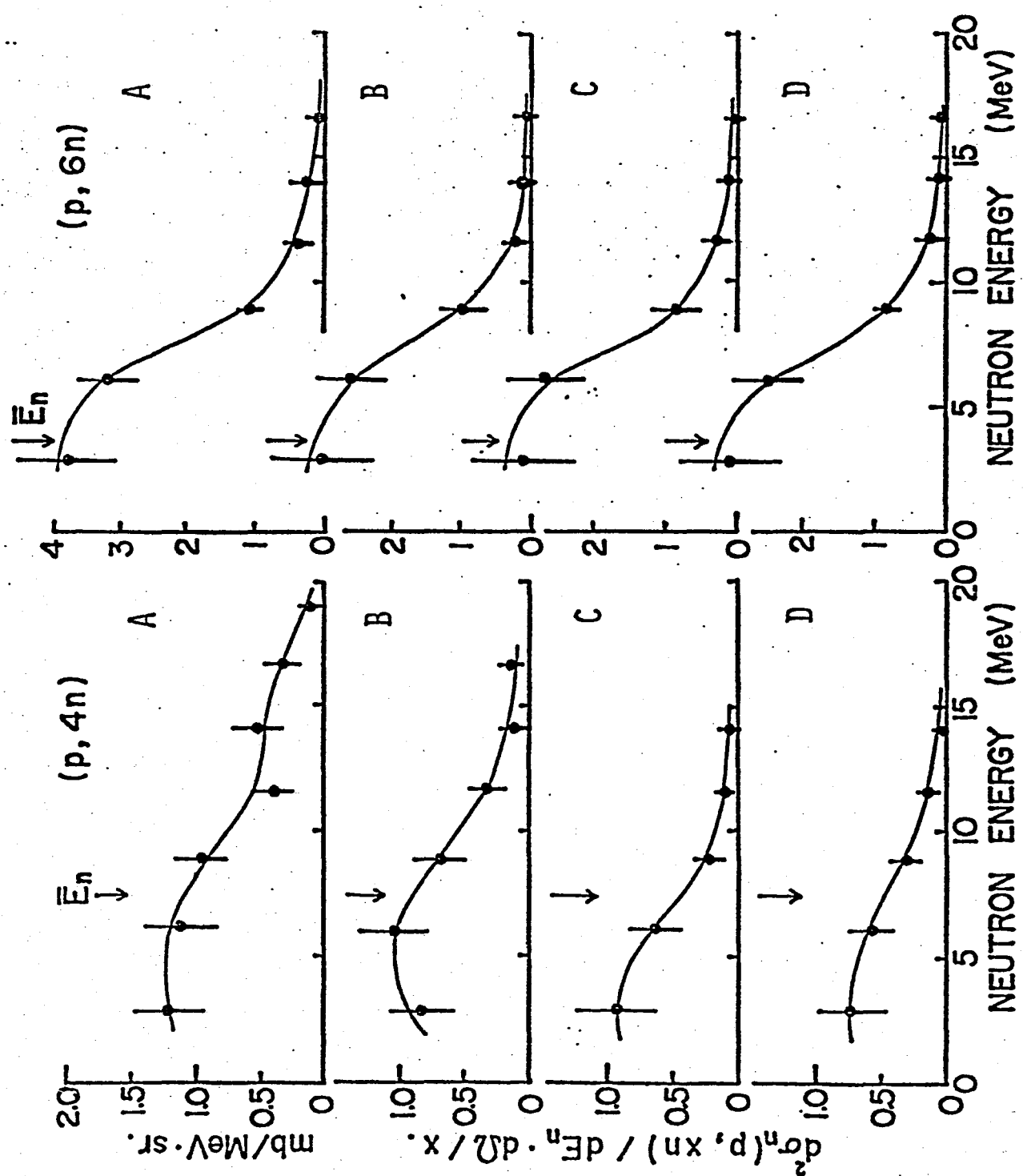


Fig. 3-18-b

NEUTRON ANGULAR DISTRIBUTION

$164\text{Dy} + 120\text{MeV } \alpha$

- $E_n \geq 2.5 \text{ MeV}$
- $E_n \geq 8.5 \text{ MeV}$

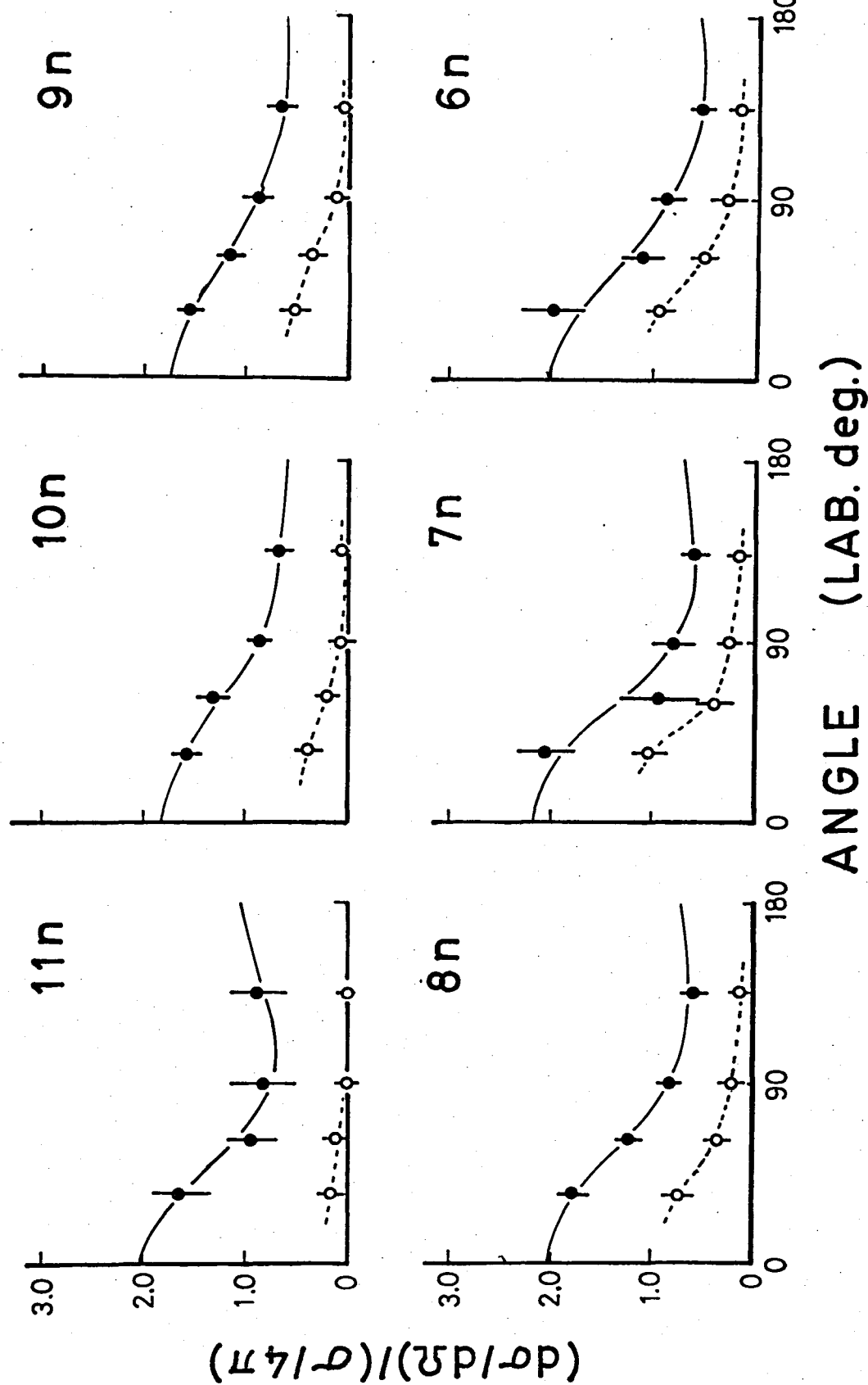


Fig. 3-19-a

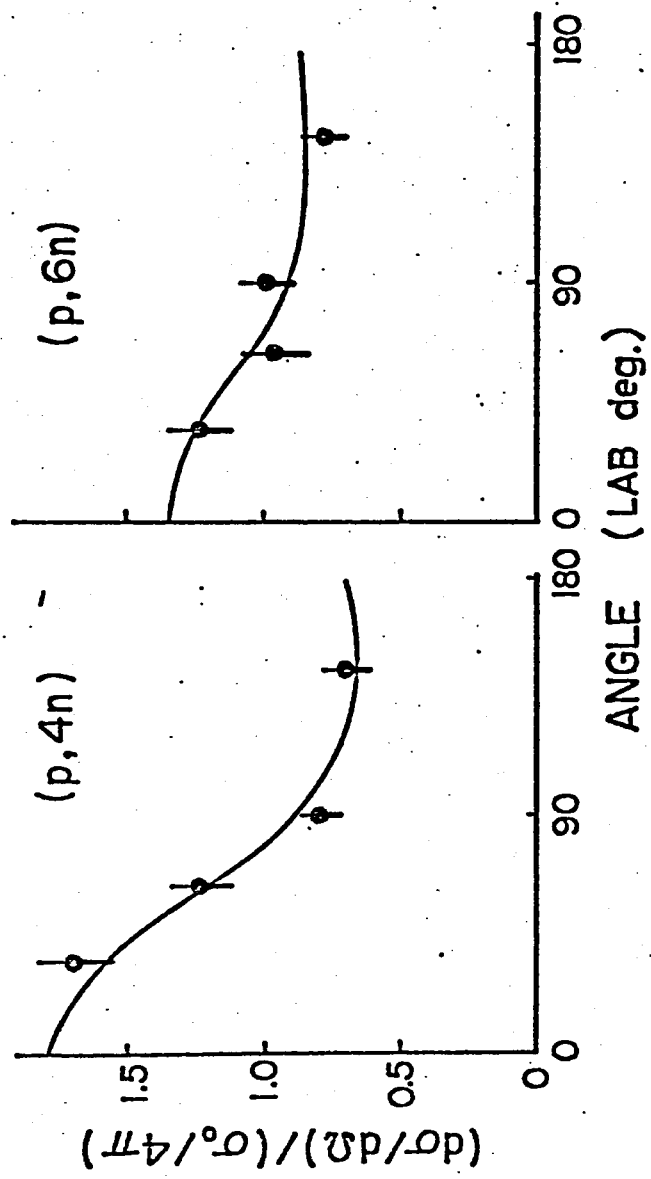


Fig. 3-19-b

$^{164}\text{Dy} + 120\text{ MeV-}\alpha$

$E_n \geq 2.5\text{ MeV}$

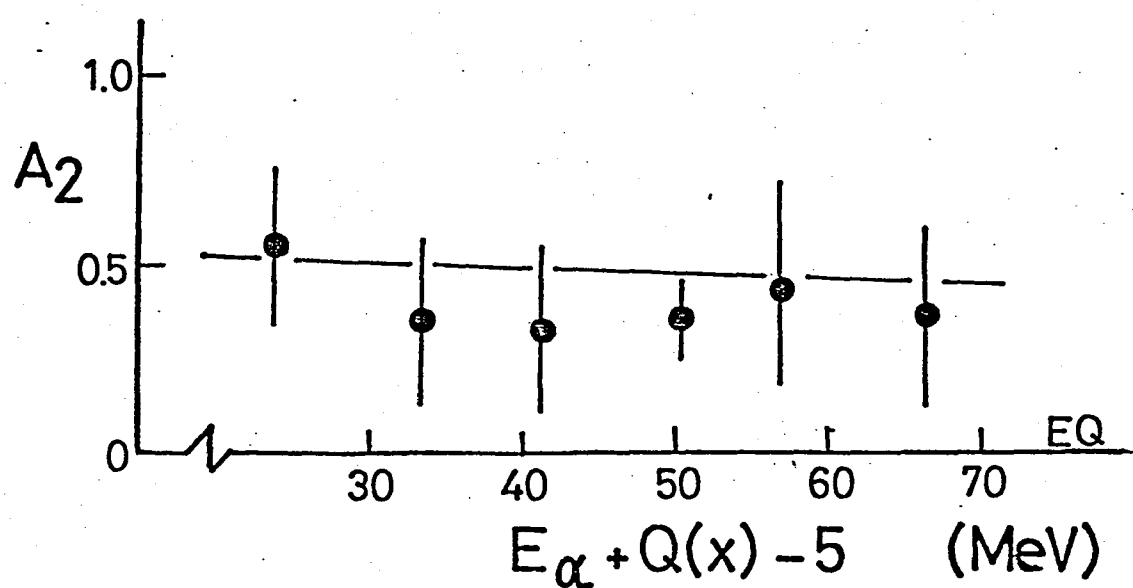
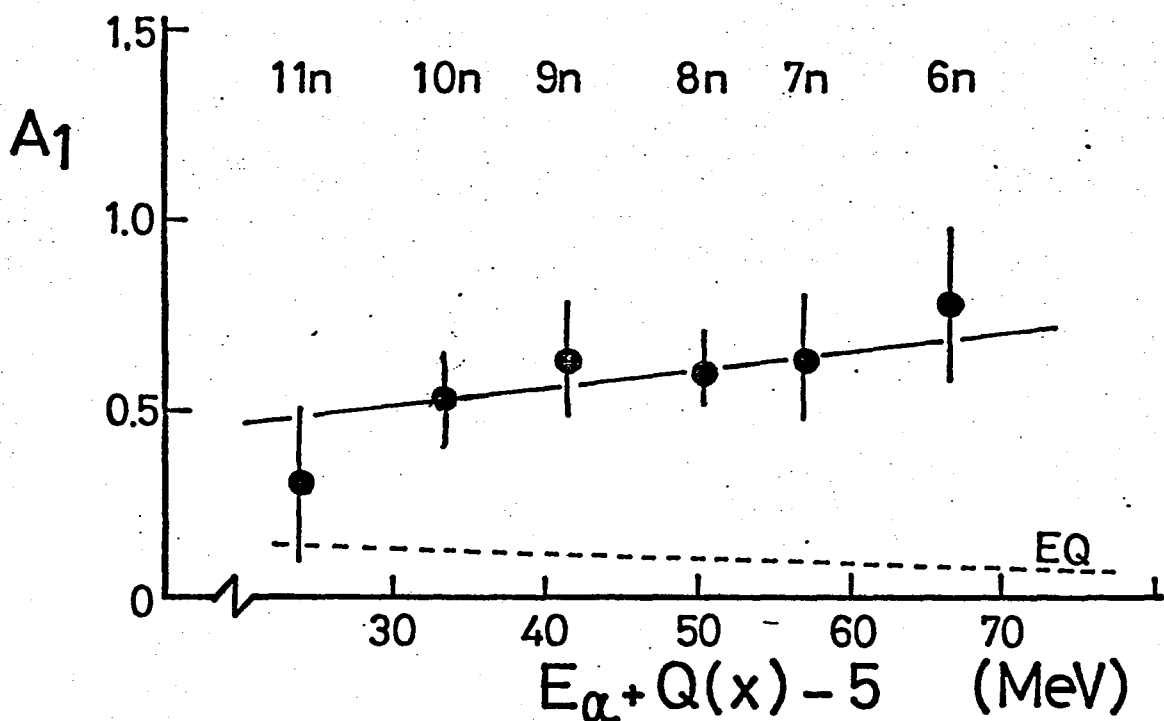


Fig. 3-20-a

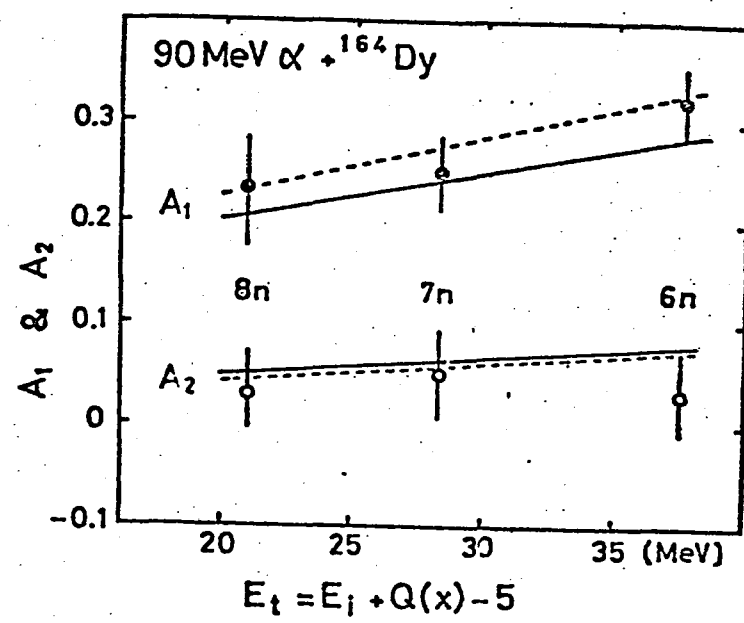


Fig. 3-20-b

PREEQUILIBRIUM FRACTION

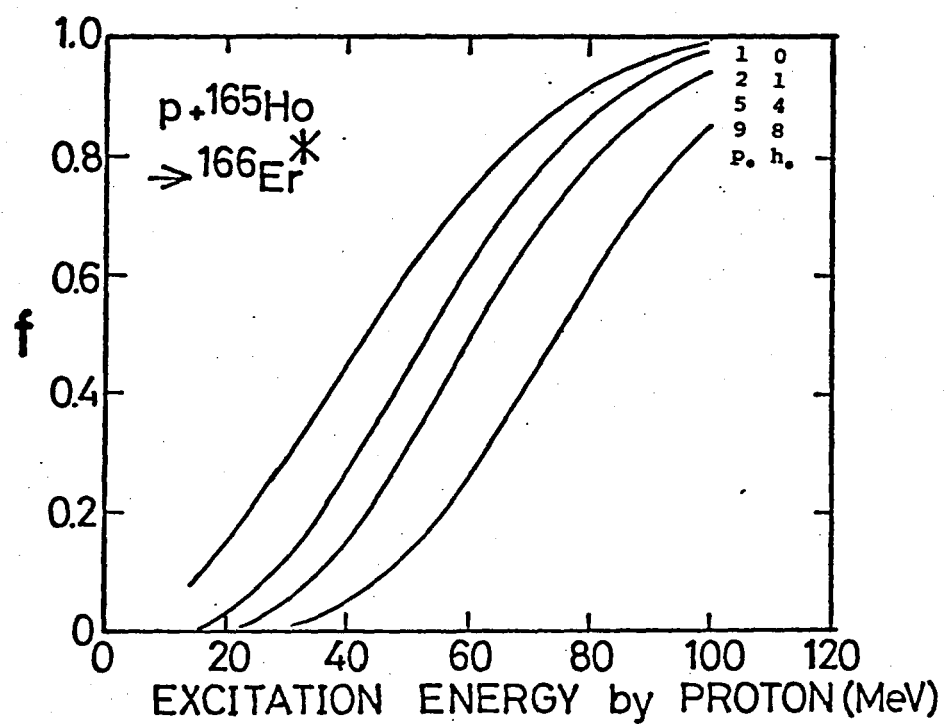
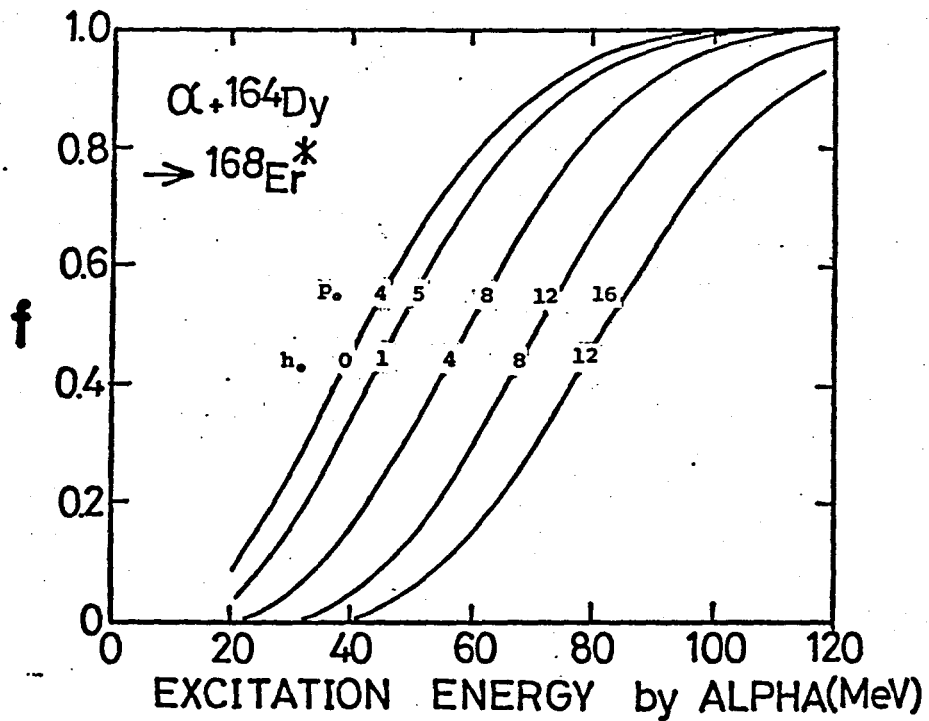


Fig. 4-1

ESCAPE PROBABILITY VS. EXCITON NUMBER

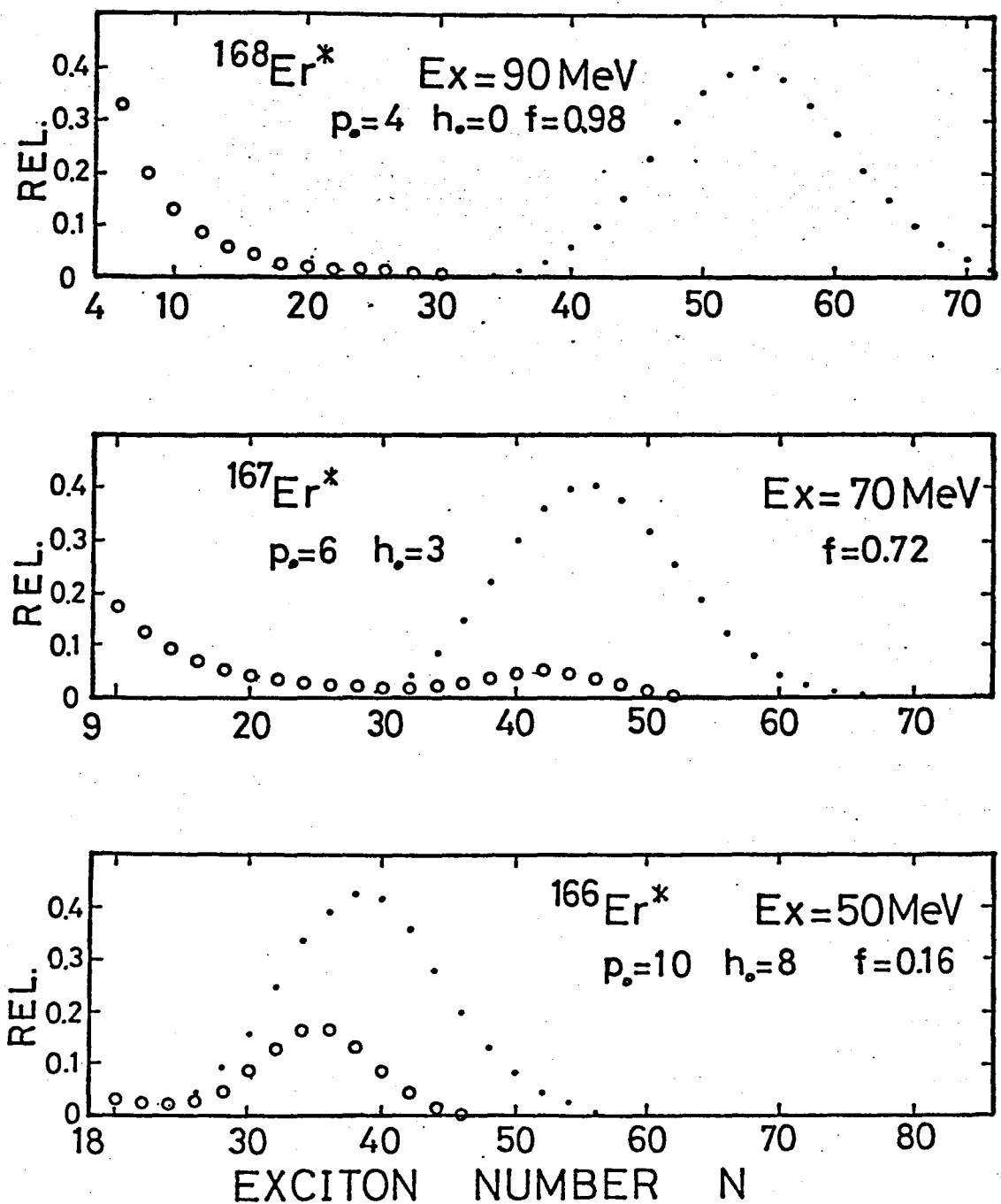


Fig.4-2

NEUTRON ENERGY SPECTRA

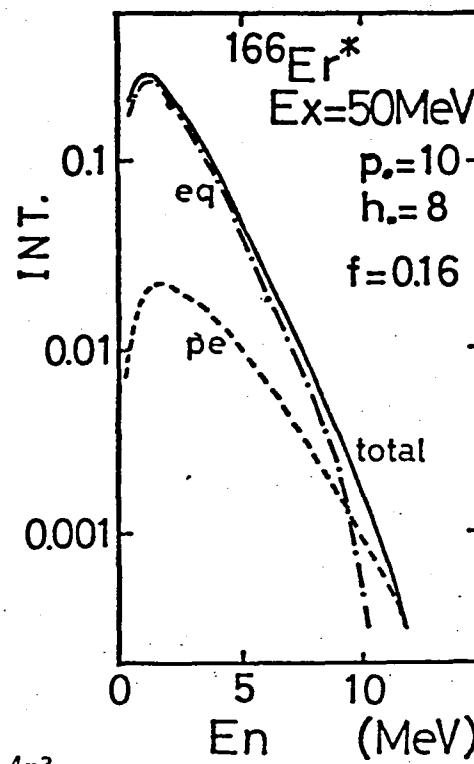
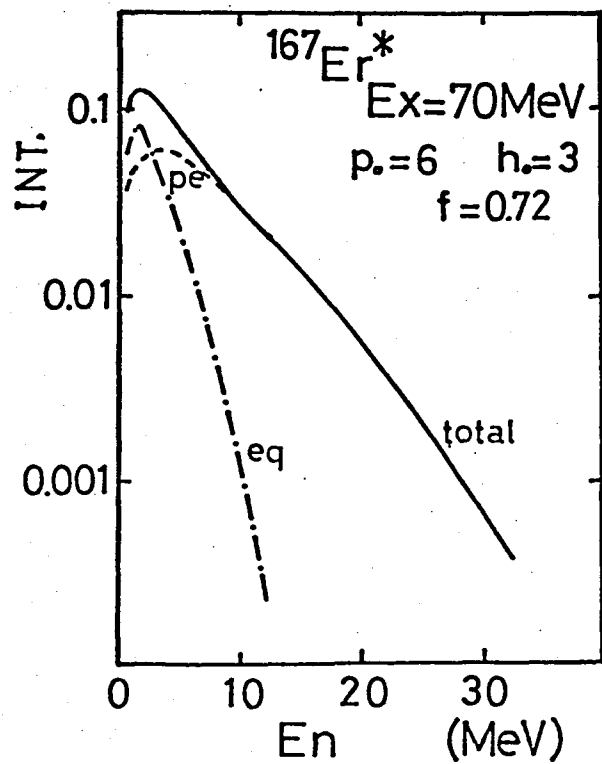
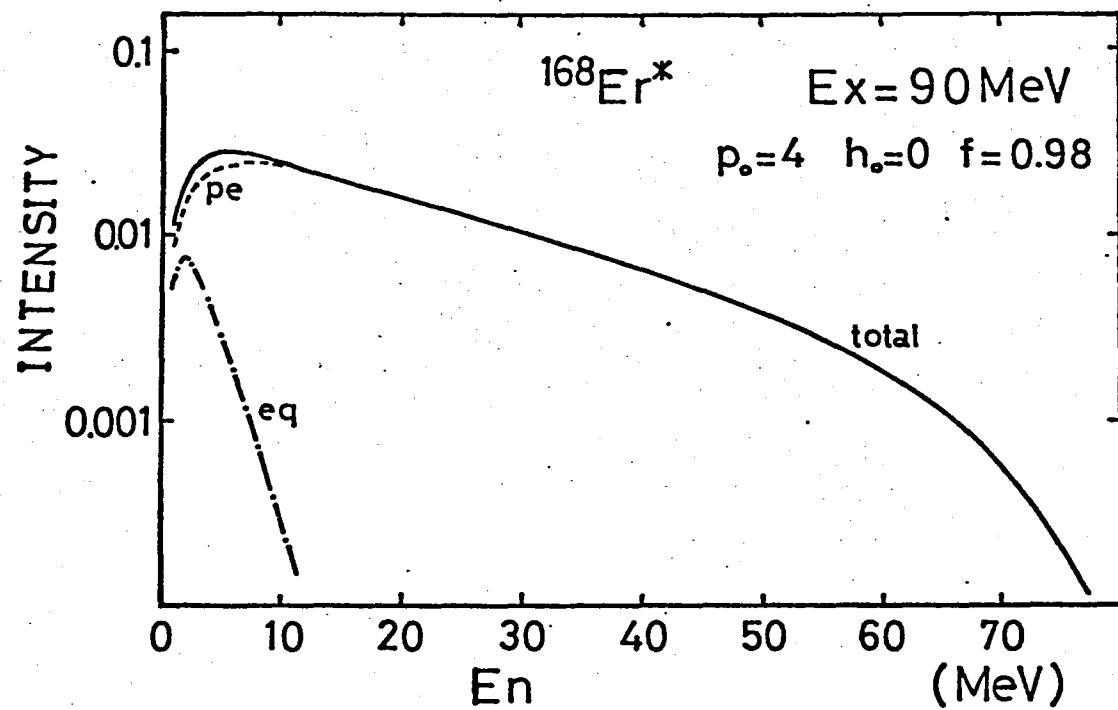


Fig. 4-3

NEUTRON ANGULAR DISTRIBUTION

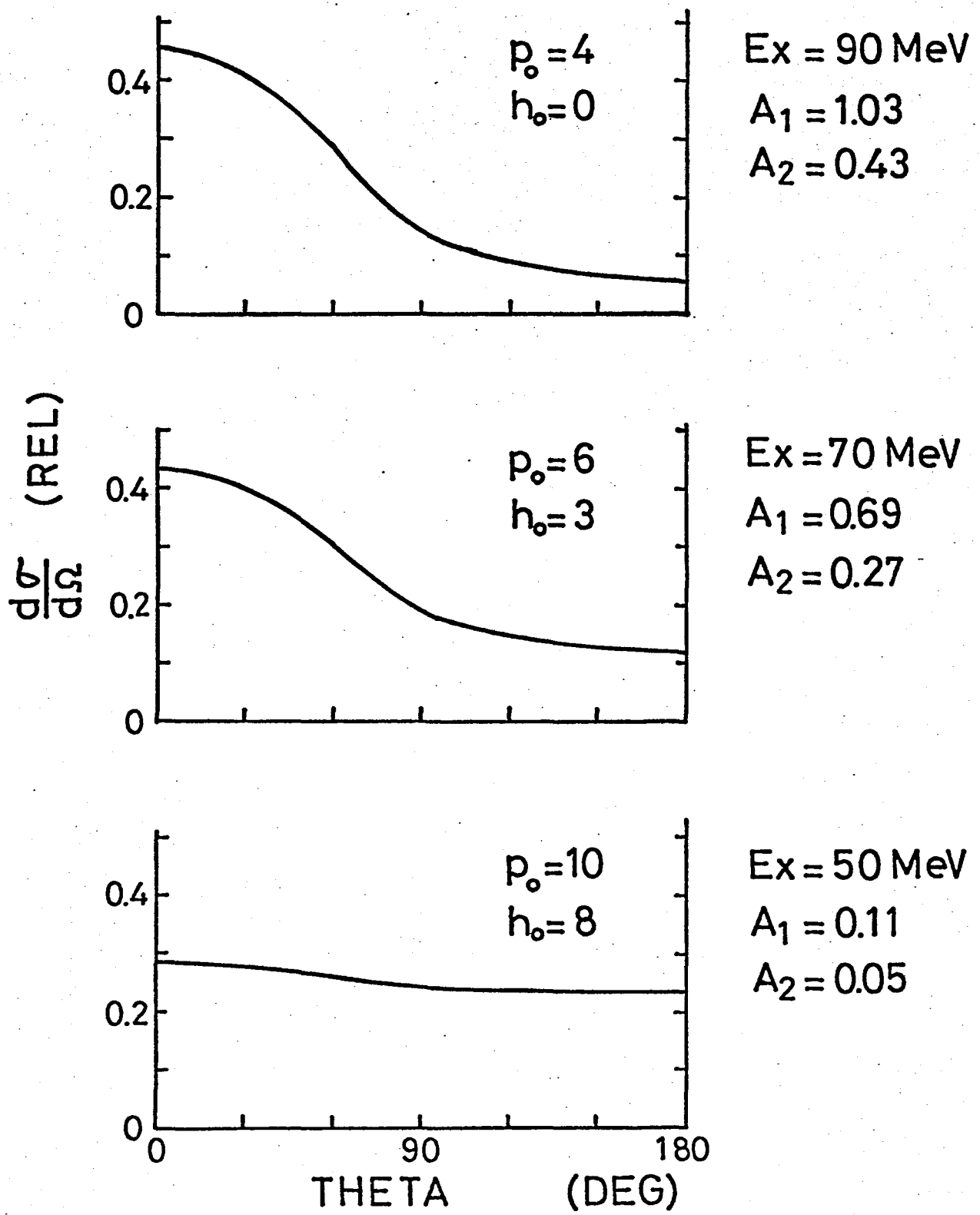


Fig. 4-4

Preequilibrium & Equilibrium Processes (Exciton Model)

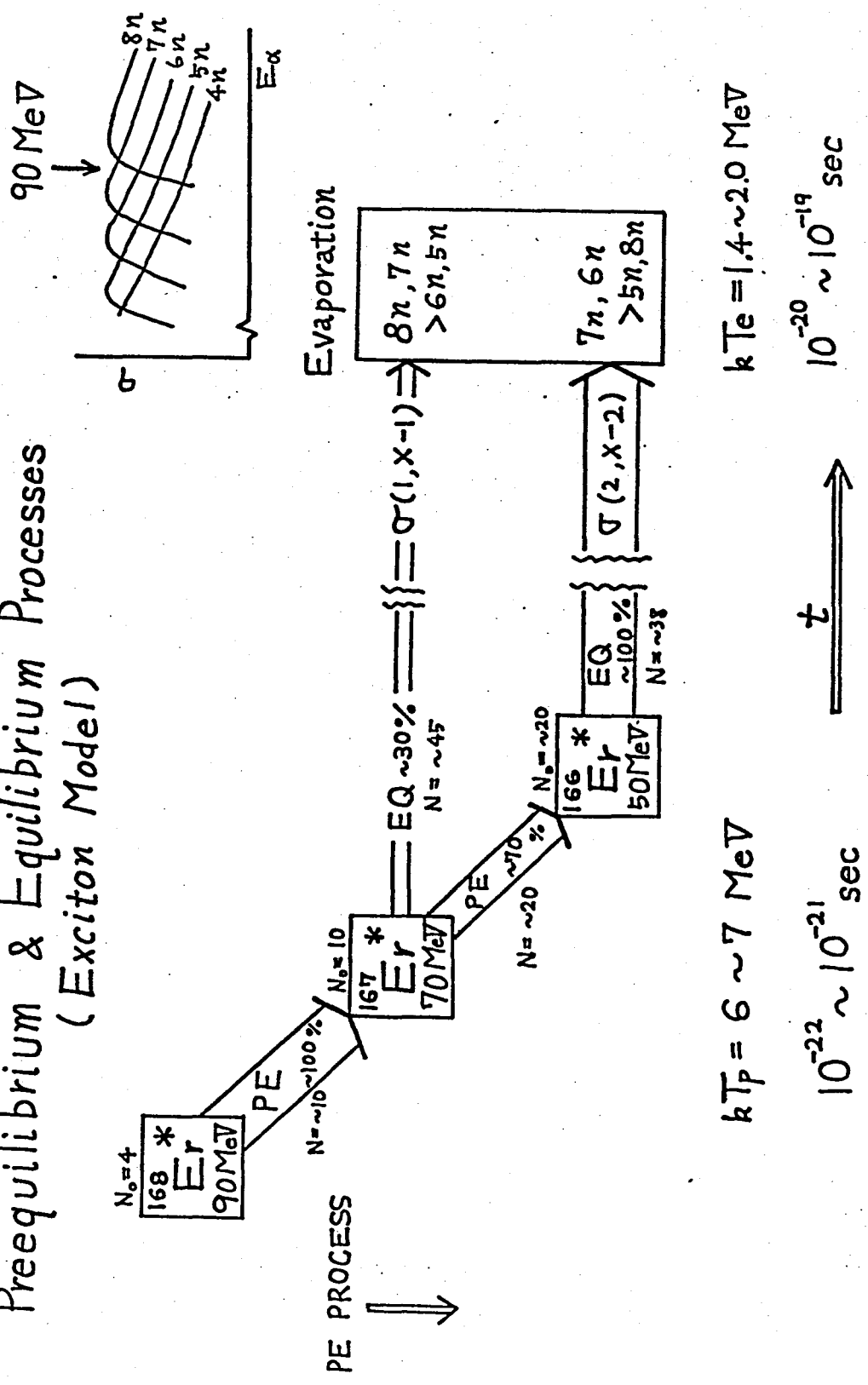


Fig. 4-5

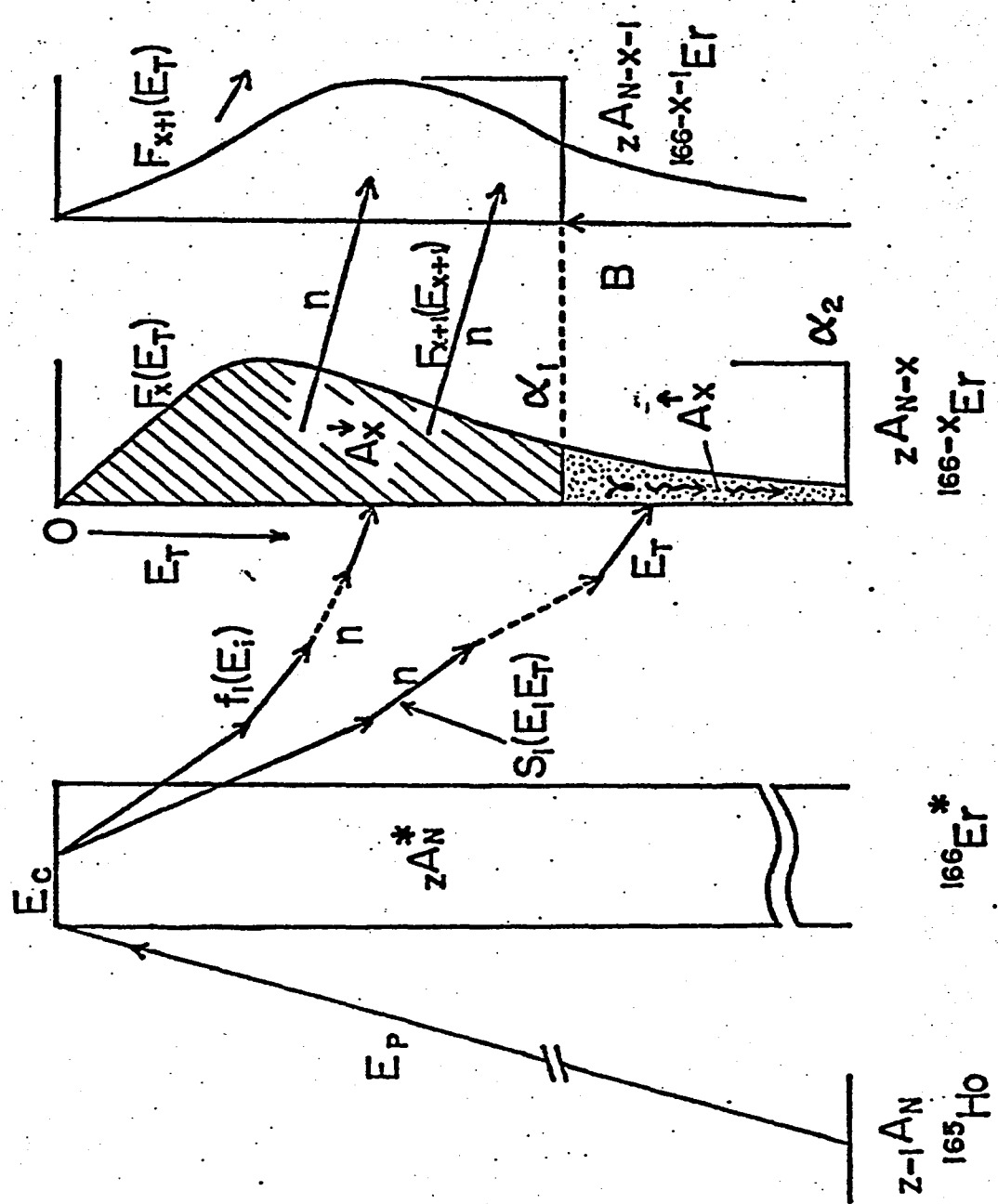


Fig. 4-6

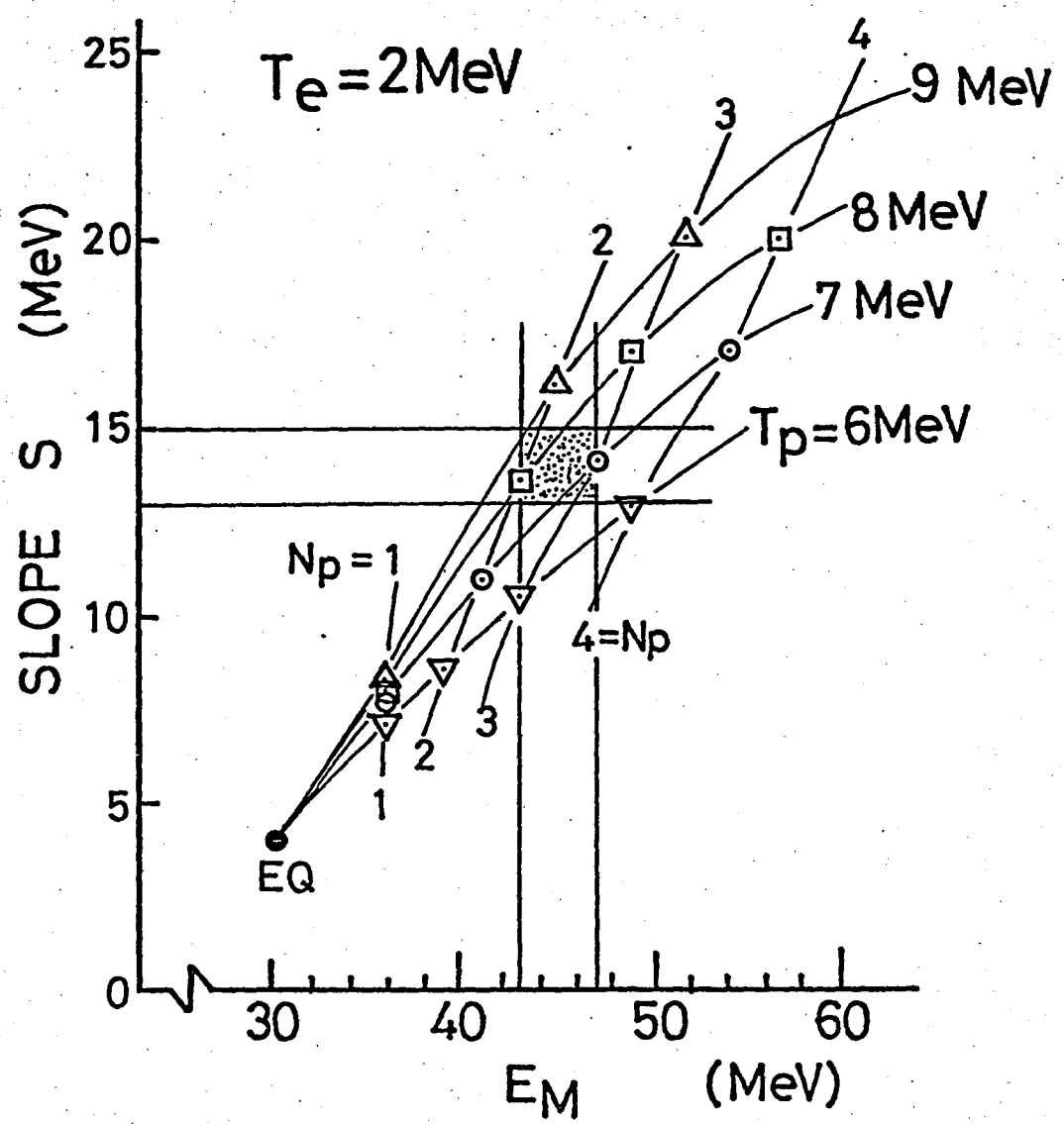


Fig. 4-7

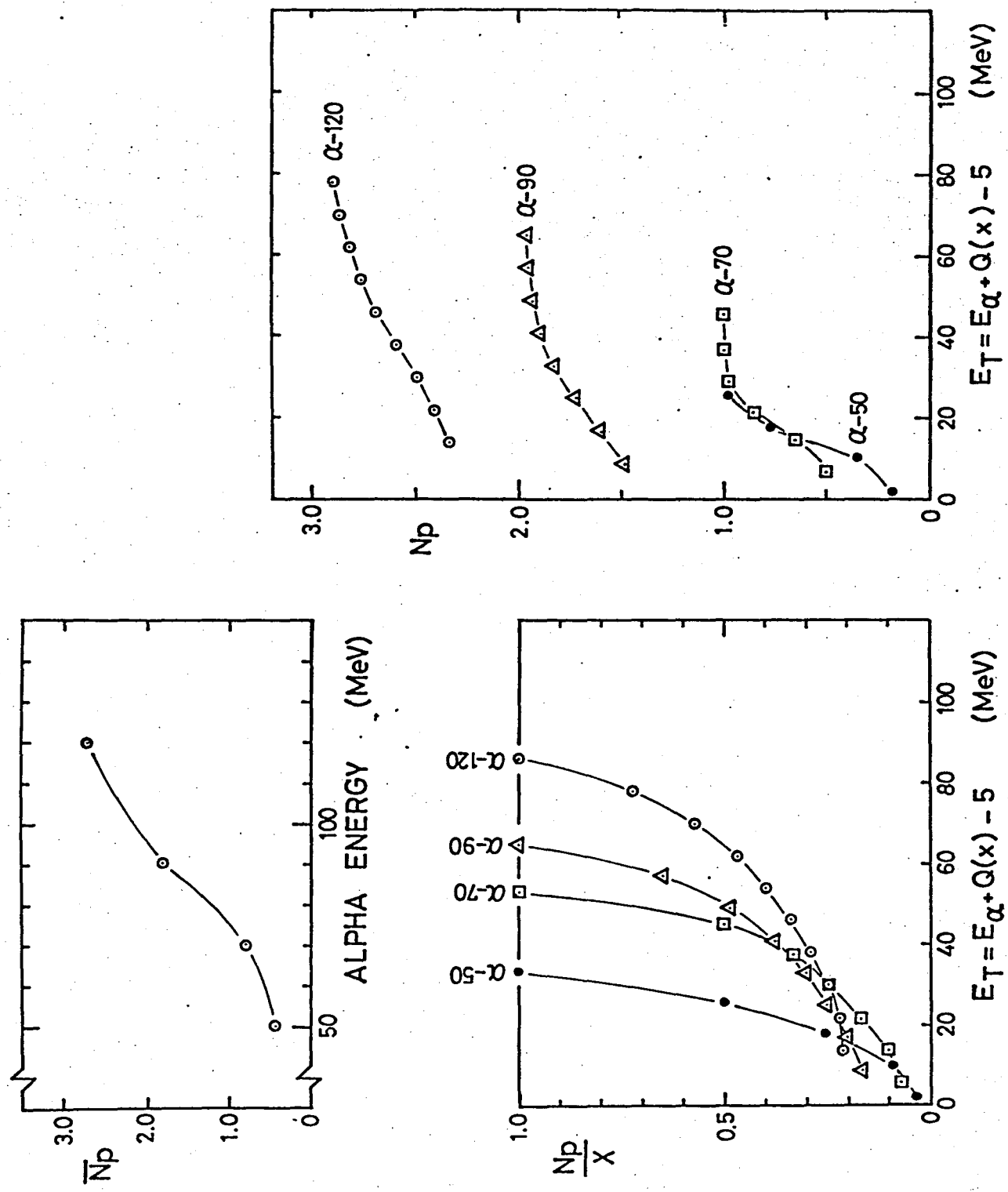


Fig. 4-8

$^{164}\text{Dy} + 120 \text{ MeV } \alpha$

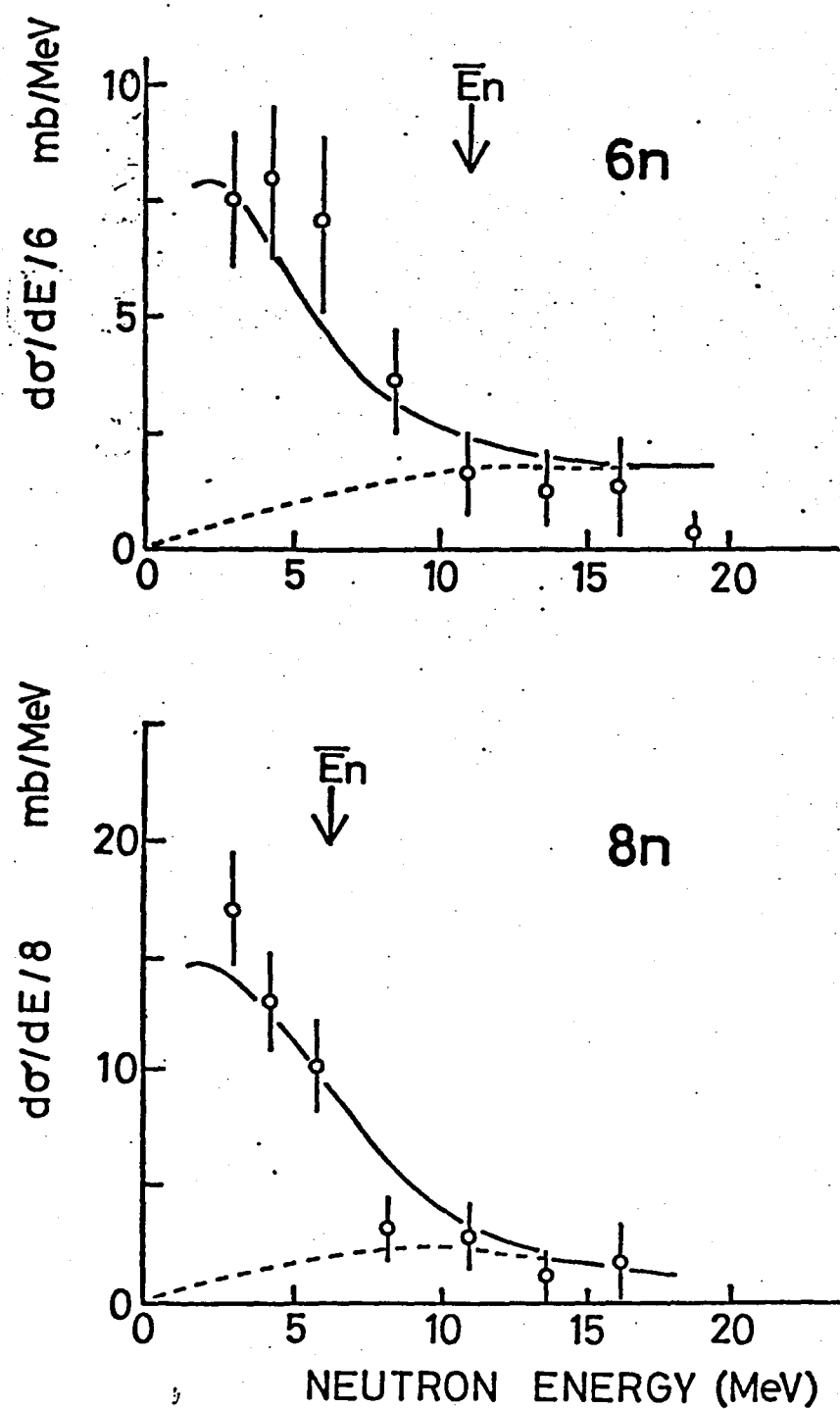


Fig. 4-9

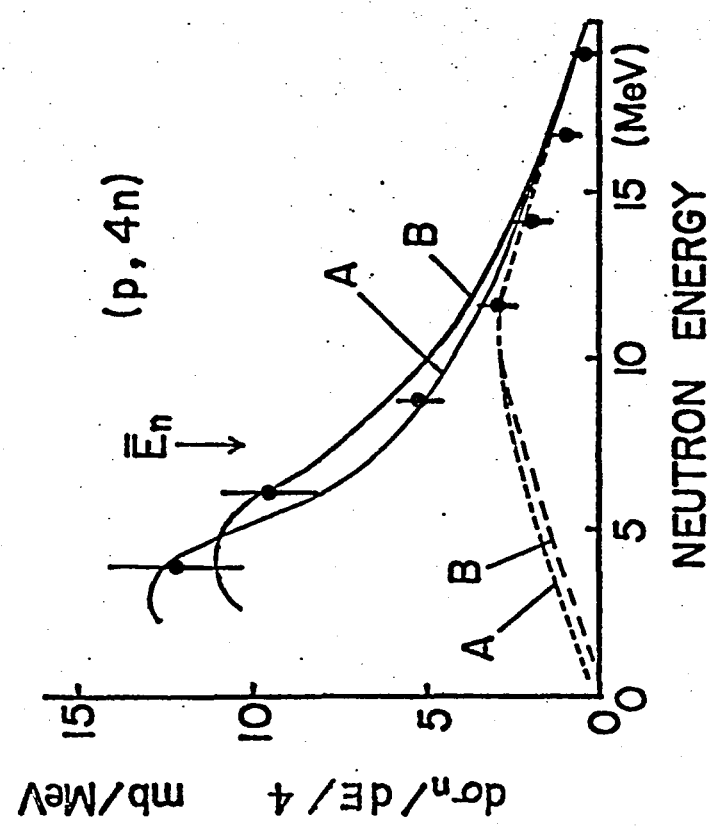


Fig. 4-10

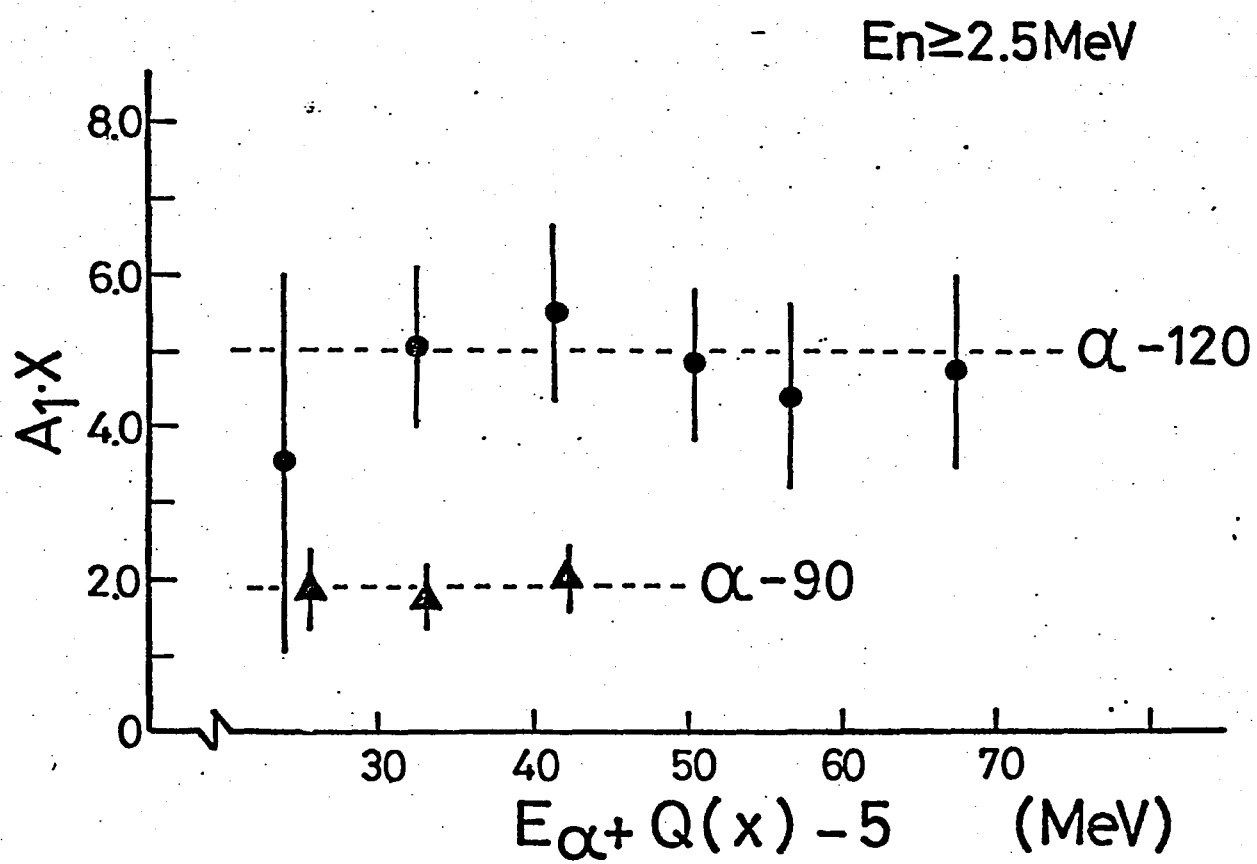


Fig. 4- 11